

WL-TR-96-4075

CHARACTERIZATION OF THE ISOTHERMAL
ELEVATED TEMPERATURE HIGH FREQUENCY FATIGUE
BEHAVIOR OF SCS-6/TIMETAL®21S [0/90]_s



NORMAN D. SCHEHL

UNIVERSITY OF DAYTON RESEARCH INSTITUTE
300 COLLEGE PARK
DAYTON OHIO 45469-0128

JUNE 1996

FINAL REPORT

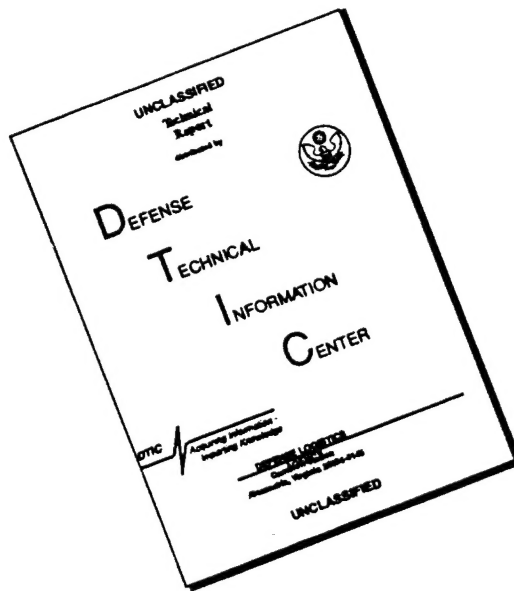
APPROVED FOR PUBLIC RELEASE; DISTRIBUTION IS UNLIMITED.

DTIC QUALITY INSPECTED 4

MATERIALS DIRECTORATE
WRIGHT LABORATORY
AIR FORCE MATERIEL COMMAND
WRIGHT PATTERSON AFB OH 45433-7734

19960930 095

DISCLAIMER NOTICE




THIS DOCUMENT IS BEST QUALITY AVAILABLE. THE COPY FURNISHED TO DTIC CONTAINED A SIGNIFICANT NUMBER OF PAGES WHICH DO NOT REPRODUCE LEGIBLY.

NOTICE

WHEN GOVERNMENT DRAWINGS, SPECIFICATIONS, OR OTHER DATA ARE USED FOR ANY PURPOSE OTHER THAN IN CONNECTION WITH A DEFINITELY GOVERNMENT-RELATED PROCUREMENT, THE UNITED STATES GOVERNMENT INCURS NO RESPONSIBILITY OR ANY OBLIGATION WHATSOEVER. THE FACT THAT THE GOVERNMENT MAY HAVE FORMULATED OR IN ANY WAY SUPPLIED THE SAID DRAWINGS, SPECIFICATIONS, OR OTHER DATA, IS NOT TO BE REGARDED BY IMPLICATION OR OTHERWISE IN ANY MANNER CONSTRUED, AS LICENSING THE HOLDER OR ANY OTHER PERSON OR CORPORATION, OR AS CONVEYING ANY RIGHTS OR PERMISSION TO MANUFACTURE, USE, OR SELL ANY PATENTED INVENTION THAT MAY IN ANY WAY BE RELATED THERETO.

THIS REPORT IS RELEASABLE TO THE NATIONAL TECHNICAL INFORMATION SERVICE (NTIS). AT NTIS, IT WILL BE AVAILABLE TO THE GENERAL PUBLIC, INCLUDING FOREIGN NATIONS.

THIS TECHNICAL REPORT HAS BEEN REVIEWED AND IS APPROVED FOR PUBLICATION.


JAY R. JIRA, Project Engineer
Materials Behavior Branch
Metals and Ceramics Division


ALLAN W. GUNDERSON, Chief
Materials Behavior Branch
Metals and Ceramics Division


WALTER M. GRIFFITH, Asst Chief
Metals and Ceramics Division
Materials Directorate

IF YOUR ADDRESS HAS CHANGED, IF YOU WISH TO BE REMOVED FROM OUR MAILING LIST, OR IF THE ADDRESSEE IS NO LONGER EMPLOYED BY YOUR ORGANIZATION, PLEASE NOTIFY, WL/MLLN, WRIGHT-PATTERSON AFB OH 45433-7817 TO HELP US MAINTAIN A CURRENT MAILING LIST.

COPIES OF THIS REPORT SHOULD NOT BE RETURNED UNLESS RETURN IS REQUIRED BY SECURITY CONSIDERATIONS, CONTRACTUAL OBLIGATIONS, OR NOTICE ON A SPECIFIC DOCUMENT.

REPORT DOCUMENTATION PAGE			Form Approved OMB No. 0704-0188	
Public reporting burden for this collection of information is estimated to average 1 hour per response, including the time for reviewing instructions, searching existing data sources, gathering and maintaining the data needed, and completing and reviewing the collection of information. Send comments regarding this burden estimate or any other aspect of this collection of information, including suggestions for reducing this burden, to Washington Headquarters Services, Directorate for Information Operations and Reports, 1215 Jefferson Davis Highway, Suite 1204, Arlington, VA 22202-4302, and to the Office of Management and Budget, Paperwork Reduction Project (0704-0188), Washington, DC 20503.				
1. AGENCY USE ONLY (Leave blank)	2. REPORT DATE June 1996	3. REPORT TYPE AND DATES COVERED Final		
4. TITLE AND SUBTITLE CHARACTERIZATION OF THE ISOTHERMAL ELEVATED TEMPERATURE HIGH FREQUENCY FATIGUE BEHAVIOR OF SCS-6/Timetal® 215 [0/90] _s		5. FUNDING NUMBERS C F33615-91-C-5602 PE 62102 PR 2302 TA P1 WU 03		
6. AUTHOR(S) NORMAN D. SCHEHL				
7. PERFORMING ORGANIZATION NAME(S) AND ADDRESS(ES) UNIVERSITY OF DAYTON RESEARCH INSTITUTE 300 COLLEGE PARK DAYTON, OH 45469-0128		8. PERFORMING ORGANIZATION REPORT NUMBER		
9. SPONSORING / MONITORING AGENCY NAME(S) AND ADDRESS(ES) MATERIALS DIRECTORATE WRIGHT LABORATORY AIR FORCE MATERIEL COMMAND WRIGHT PATTERSON AFB OH 45433-7734 POC: Mr. Jay Jira; 513-255-1358		10. SPONSORING / MONITORING AGENCY REPORT NUMBER WL-TR-96-4075		
11. SUPPLEMENTARY NOTES				
12a. DISTRIBUTION / AVAILABILITY STATEMENT APPROVED FOR PUBLIC RELEASE; DISTRIBUTION UNLIMITED		12b. DISTRIBUTION CODE		
13. ABSTRACT (Maximum 200 words) An evaluation of the high frequency fatigue behavior of a SCS-6/Timetal®21S [0/90] _s composite at elevated temperature was conducted. Experimental isothermal fatigue tests were performed on a unique high frequency test system capable of operating at frequencies in excess of 200 Hz. The effects of frequency, maximum stress, stress ratio, and elevated temperature on fatigue life were investigated. The results indicate that fatigue life of the cross-ply composite is primarily cycle dependent at 650°C, and both cycle and time dependent at 815°C. A frequency effect was noted, and fatigue results suggest that an endurance limit exists for this material at 650°C. Fractography and metallography were performed to characterize the failure mechanisms and progression of damage for specimens tested at 650°C and 815°C. Evidence of internal crack initiation from the off-axis fibers leading to fully fiber bridged through cracks was observed at both temperatures. Direct current electric potential was used to monitor the evolution of fatigue damage during the tests. A linear summation model was adapted to predict the fatigue life as a function of frequency, stress range, and stress ratio based on fractions of life under high frequency fatigue and creep. Model predictions were compared to experimental data at frequencies ranging from 0.01 Hz to 200 Hz.				
14. SUBJECT TERMS Cross-ply-composite, elevated temperature fatigue, high frequency fatigue, titanium matrix composites.		15. NUMBER OF PAGES 119		
		16. PRICE CODE		
17. SECURITY CLASSIFICATION OF REPORT UNCLASSIFIED	18. SECURITY CLASSIFICATION OF THIS PAGE UNCLASSIFIED	19. SECURITY CLASSIFICATION OF ABSTRACT UNCLASSIFIED	20. LIMITATION OF ABSTRACT SAR	

TABLE OF CONTENTS

INTRODUCTION	1
1.1 BACKGROUND.....	1
1.2 OBJECTIVE	3
EXPERIMENTAL METHODOLOGY	4
2.1 MATERIAL	5
2.2 SPECIMEN GEOMETRY AND PREPARATION.....	5
2.3 NONDESTRUCTIVE EVALUATION.....	6
2.4 SPECIMEN GRIPPING	8
2.5 LOADING EQUIPMENT	8
2.6 MODAL ANALYSIS.....	14
2.7 TEMPERATURE EQUIPMENT AND RESPONSE	19
2.8 DAMAGE MONITORING EQUIPMENT	21
2.9 DISPLACEMENT EQUIPMENT	24
2.10 EXPERIMENTAL PROCEDURE	24
2.11 TEST CONDITIONS	25
RESULTS	26
3.1 FATIGUE LIFE RESULTS	26
3.2 FIBER VOLUME FRACTION NORMALIZING PROCEDURE.....	26
3.3 DISCUSSION OF 650°C FATIGUE LIFE RESULTS.....	32
3.4 DISCUSSION OF 815°C FATIGUE LIFE RESULTS.....	37
3.5 RESIDUAL STRENGTH MEASUREMENTS.....	42
PHYSICAL OBSERVATIONS	45
4.1 FATIGUE DAMAGE MECHANISMS	45
4.2 MICROSTRUCTURAL EVOLUTION.....	45
4.3 FATIGUE DAMAGE OBSERVATIONS	50
4.4 FRACTOGRAPHY OF SPECIMENS TESTED AT 650°C.....	54
4.5 FRACTOGRAPHY OF SPECIMENS TESTED AT 815°C.....	63
DAMAGE MONITORING	67
5.1 ELECTRIC POTENTIAL RESULTS.....	67
5.2 CORRELATION OF DCEP INCREASE WITH PHYSICAL OBSERVATIONS.....	79

LIFE PREDICTION	86
6.1 LINEAR SUMMATION MODEL	86
6.2 FATIGUE LIFE PREDICTIONS	91
6.3 BLOCK LOADING STUDY	99
CONCLUSIONS.....	104
REFERENCES	106

LIST OF FIGURES

FIGURE

1.	High frequency fatigue specimen geometry (dimensions in mm)	7
2.	Ultrasonic C-scans, comparison between a sample with and without processing damage. The high attenuation dark region denoted by the arrow, indicates poor fiber spacing.....	9
3.	Friction grips and specimen assembly	10
4.	C20 high frequency fatigue test system.	11
5.	C20 high frequency automated control schematic.....	12
6.	High frequency fatigue sinusoidal loading waveform.....	13
7.	Modal analysis geometry and accelerometer locations.....	16
8.	Out-of-plane specimen frequency response.....	17
9.	Greatly exaggerated motions of the specimen and load train are shown representing characteristic modal shapes.....	18
10.	Two zone control heating lamp schematic.....	20
11.	Specimen temperature survey (midpoint = 0.0, dimensions in mm).....	22
12.	Electric potential current and pickup lead configuration.	23
13.	650°C Fatigue Life Results of SCS-6/Timetal®21S [0/90] _s	33
14.	650°C SCS-6/Timetal®21S [0/90] _s fatigue life time to failure results.....	35
15.	650°C SCS-6/Timetal®21S [0/90] _s , maximum stress vs. cycles to failure fatigue life results.	36
16.	Goodman Diagram, SCS-6/Timetal®21S [0/90] _s at 200 Hz and 650°C.	38

17.	Goodman Diagram, SCS-6/Timetal®21S [0/90]s at 200 Hz and 815°C.	39
18.	815°C SCS-6/Timetal®21S [0/90]s, stress range vs. cycles to failure fatigue life results.	40
19.	815°C SCS-6/Timetal®21S [0/90]s, Stress range vs. time to failure fatigue life results.	41
20.	650°C, 815°C SCS-6/Timetal®21S [0/90]s fatigue life comparison.	43
21.	As-received microstructure.	47
22.	Mid-thickness microstructure after 650°C exposure for less than 1 hr.	48
23.	Alpha-phase precipitation on the specimen surface after 650°C exposure for less than 1 hr.	48
24.	Oxidation damage of the fiber/matrix interface on SCS-6 fibers subjected to 100 hr exposure at 650°C.	49
25.	Microstructure of specimen subjected to 815°C exposure for less than 1 hr.	51
26.	Alpha phase precipitation on the surface of a specimen subjected to 815°C exposure for less than 1 hr.	51
27.	Fiber/Matrix interface failure at each interfacial layer. (a) debonding of first carbon coating. (b) debonding between carbon coatings. (c) debonding of carbon coating and matrix.	52
28.	Matrix crack initiation at [90] fibers.	52
29.	650°C transgranular fatigue crack propagation.	53
30.	815°C intergranular fatigue crack propagation.	53
31.	Environmental damage of [0] degree fibers at 650°C.	55
32.	Environmental damage of [0] degree fibers at 815°C.	55
33.	Representative 650°C failure locations.	56
34.	Fatigue crack growth region of a 650°C test specimen.	56

35.	Complete matrix cracking around a [0] fiber.....	57
36.	Matrix fatigue cracks extending from the [90] plies.....	57
37.	Ductile overload matrix dimpling around a [0] fiber.	59
38.	Overload failure region of a 650°C test specimen with no cracks emanating from [90] fibers.....	59
39.	High magnification photo of ductile dimpling between [90] plies on fracture surface.	60
40.	Transgranular surface cracks in a specimen tested at 650°C.	61
41.	Acoustic Microscopy scan displaying edge and center cracks in a 650°C test specimen.	61
42.	Fiber bridging of through-thickness cracks.....	62
43.	Representative 815°C failure locations.....	64
44.	Matrix fatigue cracks extending from the [90] plies.....	64
45.	Thumbnail crack on 815°C fracture surface.	65
46.	Brittle failure region induced by precipitated alpha phase.	65
47.	Stepped fracture in overload failure region of an 815°C test specimen.	66
48.	DCEP for 650°C R=0.1 tests.	69
49.	DCEP for 650°C R=0.5 tests.	69
50.	DCEP for 650°C, R=0.8 tests.	70
51.	DCEP for 815°C, R=0.1 tests.	70
52.	DCEP for 815°C, R=0.5 tests.	71
53.	DCEP for 815°C, R=0.8 tests.	71
54.	Reduction in current carrying cross-sectional area due to [90] fibers.	74
55.	Normalized DCEP change for 650°C, R=0.1	76
56.	Normalized DCEP change for 650°C, R=0.5	76

57.	Normalized DCEP change for 650°C, R=0.8	77
58.	Consolidation of normalized DCEP change for 650°C, R=0.1, 0.5 and 0.8.....	77
59.	Normalized DCEP change for 815°C, R=0.1	79
60.	Normalized DCEP change for 815°C, R=0.5	79
61.	Normalized DCEP change for 815°C, R=0.8	80
62.	DCEP change with respect to life for 650°C, R=0.1.....	80
63.	DCEP change with respect to life for 650°C, R=0.5.....	81
64.	DCEP change with respect to life for 650°C, R=0.8.....	81
65.	DCEP change with respect to life for 815°C, R=0.1.....	82
66.	DCEP change with respect to life for 815°C, R=0.5.....	82
67.	DCEP change with respect to life for 815°C, R=0.8.....	83
68.	Cyclic damage term, 200 Hz power law fit, R=0.1, 650°C.....	88
69.	Cyclic damage term 200 Hz power law fit, R=0.1, 815°C.....	89
70.	Experimental data and model predictions for R=0.1, 650°C.....	92
71.	Time dependent damage term creep rupture life, power law fit, 650°C	93
72.	Time dependent damage term creep rupture life, power law fit, 815°C.....	94
73.	Experimental data and model predictions at 815°C, R=0.1.....	95
74.	Experimental data and model predictions for 200 Hz, R=0.1, 0.5, and 0.8, 650°C.	96
75.	Experimental data and model predictions for 200 Hz, R=0.1, 0.5, and 0.8, 815°C.	97
76.	Block Loading normalized DCEP change.	102

LIST OF TABLES

TABLE

1.	200 Hz FATIGUE TEST RESULTS ON [0/90] _s SCS-6/TIMETAL®21S.....	27
2.	0.01 Hz FATIGUE TEST RESULTS ON [0/90] _s SCS-6/TIMETAL®21S	28
3.	1 Hz, FATIGUE TEST RESULTS ON [0/90] _s SCS-6/TIMETAL®21S.....	28
4.	TENSILE TEST RESULTS ON [0/90] _s SCS-6/TIMETAL®21S	29
5.	CREEP TEST RESULTS ON [0/90] _s SCS-6/TIMETAL®21S.....	29
6.	TENSILE TEST RESULTS ON TIMETAL®21S.....	30
7.	RESIDUAL STRENGTH AFTER 100 HOUR THERMAL EXPOSURE	44
8.	CONSTITUENT RESISTIVITIES AS A FUNCTION OF TEMPERATURE.....	68
9.	PREDICTED AND MEASURED INITIAL DCEP VOLTAGE DROP.....	75
10.	BLOCK LOADING STUDY, R=0.1, 200 Hz.....	100

FOREWORD

This study was performed at the Metals Behavior Branch, Materials Directorate, Wright-Patterson Air Force Base, Ohio and was funded under Contract No. F33615-91-C-5606.

The author would like to thank Dr. Noel Ashbaugh for guidance and support of this work, Mr. Stephan Russ and Dr. M. Khobaib for sharing their unpublished data and discussion regarding this study, and Mr. Richard Goodman for technical support concerning the experimental setup.

SECTION 1

INTRODUCTION

1.1 BACKGROUND

Continuous fiber reinforced metal matrix composites (MMC) are being considered for incorporation into the next generation of aerospace designs. Advanced aerospace initiatives such as Integrated High Performance Turbine Engine Technology (IHPTET) and hypersonic vehicles require high temperature materials with superior weight specific properties to those in existence. Titanium matrix composites (TMC) are envisioned to meet the requirements of these programs with their high specific strength, stiffness, and oxidation resistance [1, 2]. As structural components subjected to nonaxial loadings, composites also benefit from their tailorable properties. The addition of off-axis fibers into the layup was intended to improve the balance of inplane properties, and resolve the poor matrix dominated transverse properties associated with anisotropic unidirectional composites. The transverse tensile properties of TMCs were shown to benefit from the addition of off-axis fibers, and $[0/90]_S$ laminates have demonstrated intermediate strengths between the transverse and longitudinal tensile strengths of unidirectional composites [3].

The fatigue behavior of TMCs are governed by a complex accumulation of damage. Damage mechanisms include matrix cracking, fiber fracture, fiber matrix interface failure, and degradation due to environmental attack [4, 5]. The prevalent damage mechanisms vary with the fiber and matrix strengths, fiber volume fraction, fiber orientation, the nature of the mechanical loading, and the

aggressive environment [5]. High strength titanium matrices require similarly high strength fiber/matrix interfaces to transfer the load from the matrix to fiber. The presence of off-axis fibers was shown in several studies [4, 5, 6] to contribute to the development of fatigue damage through the failure of the [90] fiber/matrix interface.

A previous high frequency fatigue (HF) study of unidirectionally reinforced Ti-24Al-11Nb [7] demonstrated the susceptibility of the laminate to environmentally induced damage. Compilation of isothermal fatigue life data at several frequencies suggested that time dependent damage controlled the failure life. A second matrix alloy, Ti-15Mo-2.7Nb-3Al-0.2Si (wt%), or Timetal®21S*, is being considered for its improved oxidation resistance and elevated temperature properties [8]. The performance of this matrix alloy, and its dependence on cyclic and environmentally induced damage mechanisms, has yet to be clearly defined.

Conducting fatigue tests at high frequency (HF) better simulates a purely cycle dependent fatigue life and provides insight into cyclic and time dependent damage mechanisms. The characterization of the SCS-6/Timetal®21S [0/90]_s composite subjected to isothermal elevated temperature high frequency fatigue is described in this study.

*Timetal®21S is a trademark of the Timet Corporation, Henderson NV.

1.2 OBJECTIVE

The objective of this study was to characterize the HF fatigue behavior of SCS-6/Timetal®21S [0/90]_s by investigating the effects of frequency, maximum stress, stress ratio, and elevated temperature on fatigue life and damage evolution.

The testing parameters were chosen to provide baseline fatigue lives for a life prediction model, and to correspond with low frequency fatigue test conditions conducted at Wright Laboratory Materials Directorate, Wright-Patterson Air Force Base.

The investigation of the initiation and accumulation of damage, and the identification of damage mechanisms, were conducted using both in-situ techniques and post-test fractography and metallography.

This paper includes the experimental methodologies developed for the HF testing of cross-ply TMCs (Section 2), fatigue life results (Section 3), identification and monitoring of fatigue damage (Sections 3 and 4, respectively), and the application of a linear summation model (Section 5).

SECTION 2

EXPERIMENTAL METHODOLOGY

Initial fatigue tests of the composite material investigated in this study resulted in the majority of failures occurring at or near the grip in both low and high frequency tests. Three primary initiatives were pursued to ensure the gage section failure of the cross-ply MMC specimens. A specimen geometry more favorable for gage section failure was developed, specimen and load train alignment was improved, and nonaxial loads were identified through the determination of resonant and natural frequency induced peaks with a modal analysis study.

This section describes the experimental methodology developed for the isothermal elevated temperature high frequency fatigue testing of [0/90]_s SCS-6/Timetal®21S. The material tested and specimen geometry chosen, as well as the testing equipment and experimental techniques employed will be discussed in detail. The minimization of nonaxial loads and other steps taken to ensure gage section failure will be addressed.

For the future discussion, stress ratio, mean stress and stress-range are related to maximum and minimum stress by the following equations.

$$R = \frac{S_{\min}}{S_{\max}} \quad (2.1)$$

$$S_{\text{mean}} = \frac{(S_{\max} + S_{\min})}{2} \quad (2.2)$$

$$S_{range} = S_{max} - S_{min} \quad (2.3)$$

2.1 MATERIAL

The composite material used for this study was the SCS-6/Timetal®21S [0/90]_S composite. The continuous fiber reinforcement was the Textron SCS-6 fiber. The fiber was produced by chemical vapor deposition on a 40 μm carbon core to produce a 142 μm nominal fiber diameter. The surface was modified with the addition of two 2.0 μm coatings [9]. The first, an amorphous carbon coating that protects and strengthens the SiC fiber core; the second, a carbon rich SiC coating for improved bonding with the titanium matrix material. The matrix material is a metastable beta phase titanium alloy, Ti - 15Mo - 3Nb - 3Al - 0.2Si (weight %), developed for improved room temperature ductility and oxidation resistance [8]. The fibers were woven in a mat using a Ti-Nb crossweave to ensure adequate fiber spacing. Fabrication of the four ply composite panel was conducted using alternately stacked matrix foils and fiber mats to form a laminate which was consolidated with hot isostatic pressing (HIP). Specimens were exposed to a 620°C/8hr vacuum heat treatment to stabilize the microstructure and eliminate the potential for omega formation within the beta grains.

2.2 SPECIMEN GEOMETRY AND PREPARATION

Initial [0/90]_S testing at 650°C was conducted using a straight sided specimen geometry. After nine failures at or near the grip, which was outside the heated region, a dogbone specimen design was adapted for subsequent high frequency tests. The dogbone design, Fig. 1, had a 50% reduction in cross-sectional area, a 146 mm overall length with a length of 72 mm between grips, 12.7 mm gage section width, and a transition radius of 57 mm. Specimens were

machined using an abrasive water jet technique, and selected dogbone specimen edges were further prepared to aid in the detection of damage initiation and progression. Edges were polished using 400, 600, and 800 grit SiC paper followed by successive mechanical polishing with 15, 9, and 6 micron diamond paste. Specimens were oriented such that the [0] fibers were parallel to the loading axis. Variations in panel thickness resulted in the composite material having different fiber volume fractions. Two specimen thicknesses were HF fatigue tested, 0.80 mm and 0.93 mm, having experimentally determined volume fractions of 0.38 and 0.32, respectively.

2.3 NONDESTRUCTIVE EVALUATION

Nondestructive evaluation (NDE) techniques were used to detect abnormalities in specimens prior to testing. Ultrasonic NDE methods are useful for detecting manufacturing abnormalities in the matrix such as poor foil consolidation, delamination, or cracking [10]. Ultrasonic 45° shear wave backscattering C-scans were produced for each specimen. With the exception of one specimen, 92-599, processing damage was not detected. Fig. 2 shows the C-scans for specimen 92-599 and 92-600 respectively, where the region of local damage is apparent in 92-599. The high attenuation region in 92-599 was due to poor 90° fiber spacing, and attention was given to the proximity of its fracture location to the inconsistency.

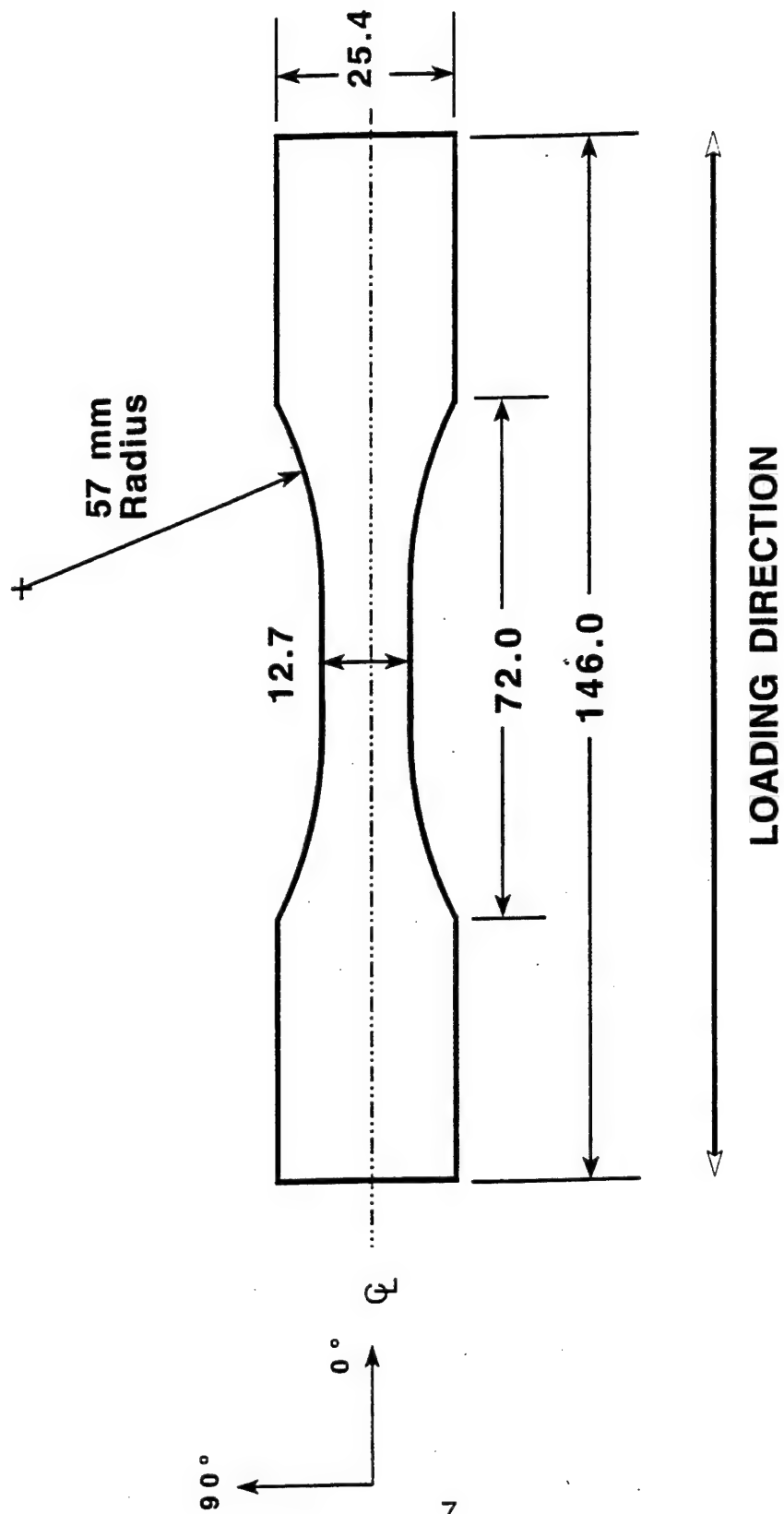


Fig. 1 High frequency fatigue specimen geometry (dimensions in mm)

2.4 SPECIMEN GRIPPING

Specimens were friction gripped with cooling air flowing through the Ti-6Al-4V grips Fig. 3. The connecting pin between the grip and load shaft was a slip fit which was then torqued, resulting in a rigid fixed gripping method rather than a pinned connection. Uniform specimen clamping was provided by four bolts evenly torqued in 25 in-lb increments to 225 in-lbs, applying a clamping pressure of approximately 10 ksi. The grips were designed to electrically isolate the specimen from the grip and load train, so that electric potential measurements of the specimen could be made. Electrical isolation was accomplished through the use of fiberglass insulators between the titanium grip and the superalloy tab. Although gripping tabs were not bonded to the specimens, the durable superalloy grip tab applied uniform clamping to the specimen and was reusable. The specimen was aligned and assembled in the grips prior to being installed in the test frame. Parallel precision ground plates were used to align the grips while the specimen was installed and gage blocks were used to center the specimen along the longitudinal loading axis.

2.5 LOADING EQUIPMENT

The C20 high frequency test system was used in this investigation and is shown in Fig. 4 [11]. The test system was an automated load control machine consisting of a dual loading system capable of producing useable loads for frequencies in excess of 300 Hz. A schematic of the automated control system is shown in Fig. 5. The high frequency loading waveform, Fig. 6, was developed

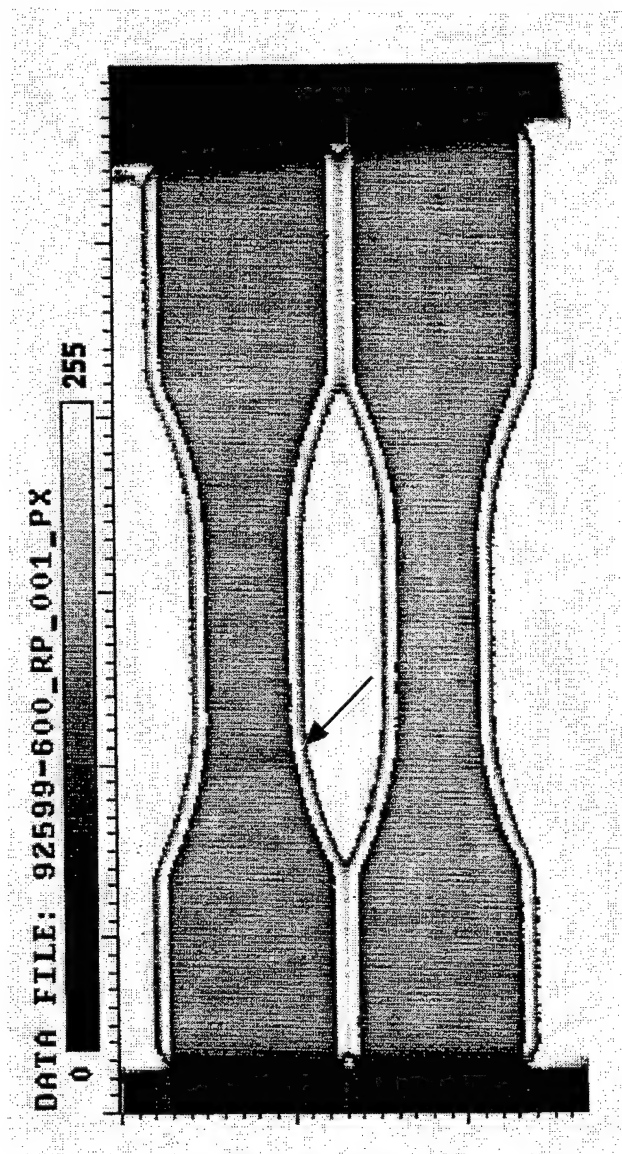


Fig. 2 Ultrasound C-scans, comparison between a sample with and without processing damage. The high attenuation dark region indicates poor fiber spacing

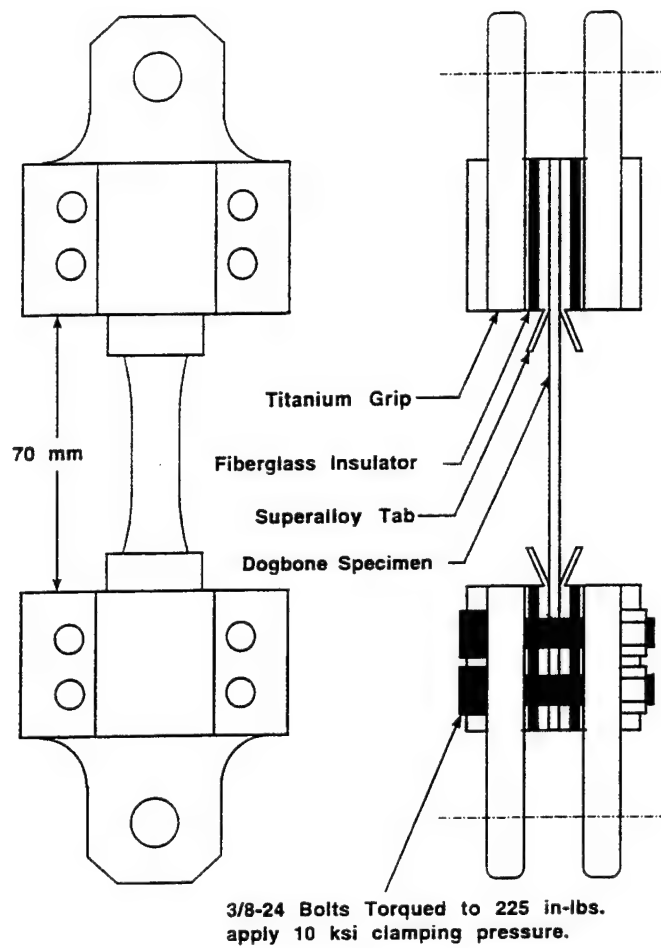


Fig. 3 Friction grips and specimen assembly

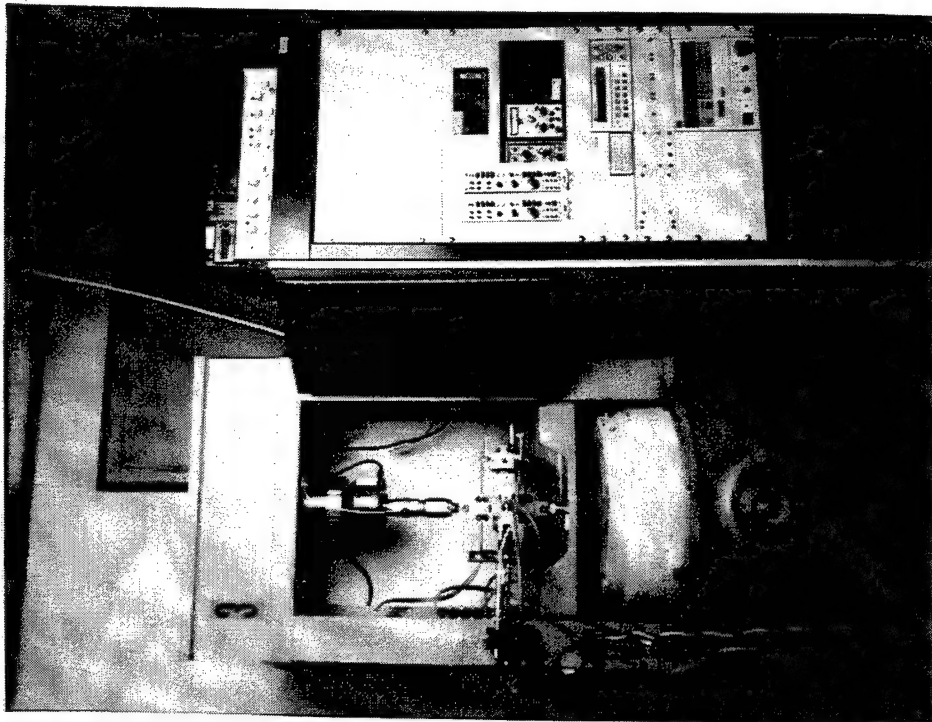
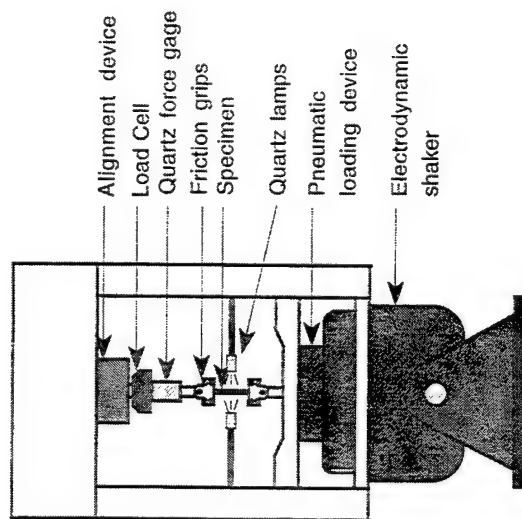


Fig. 4 C20 high frequency fatigue test system

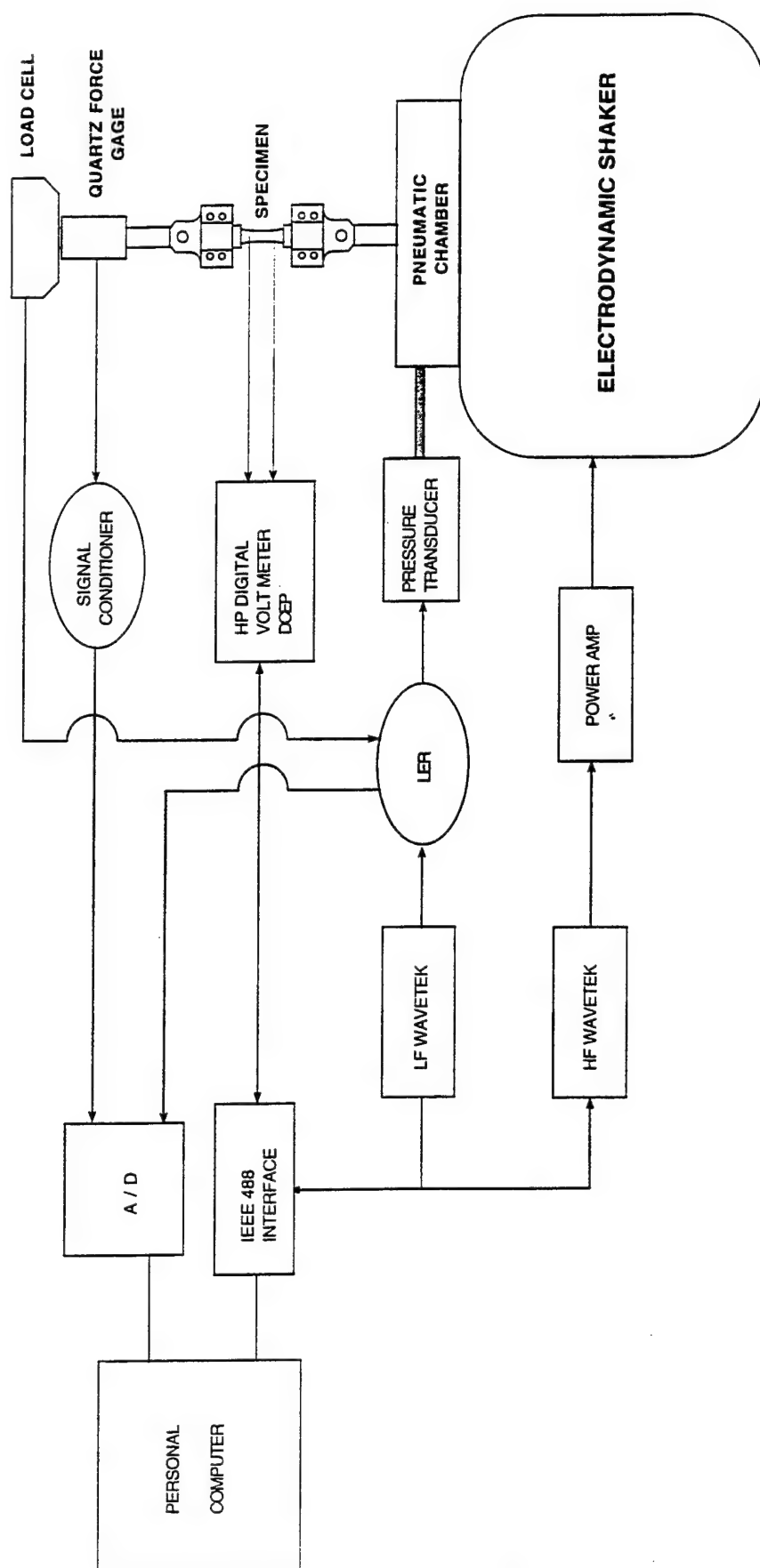


Fig. 5 C20 high frequency automated control schematic

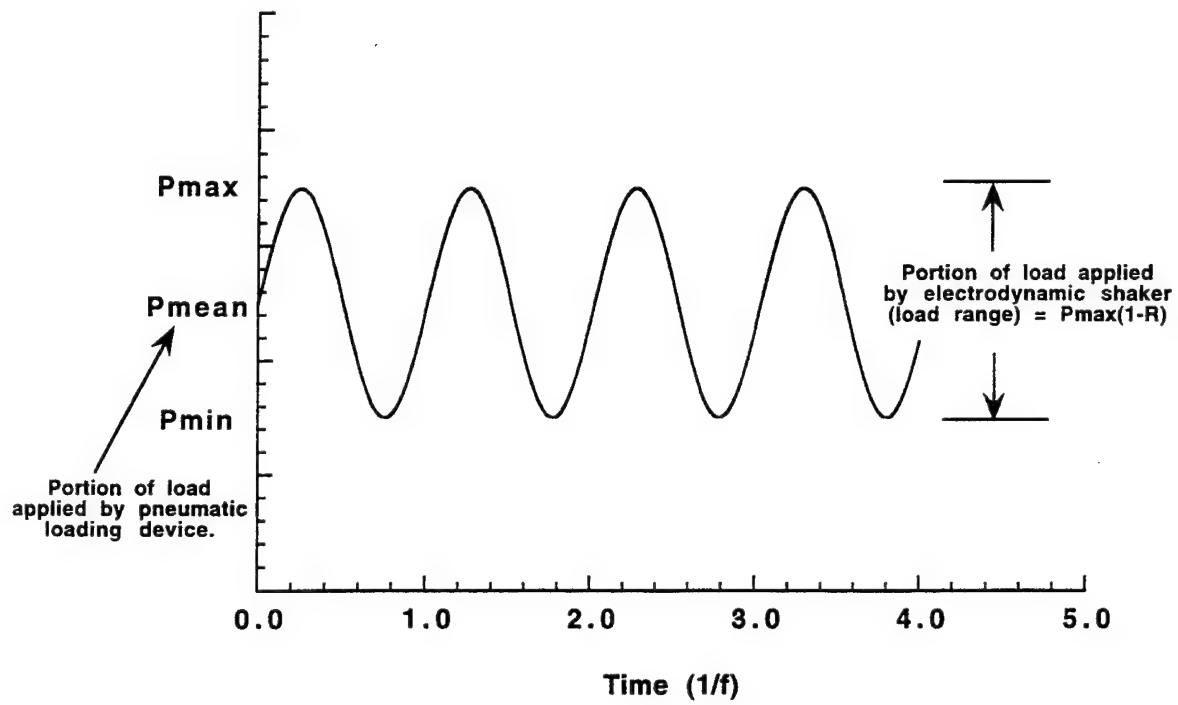


Fig. 6 High frequency fatigue sinusoidal loading waveform

using an electrodynamic shaker to superimpose a sinusoidal high frequency load on a static mean load applied by a pneumatic loading device. A load cell was used to measure mean loads, and a quartz force gage measured the high frequency peak-to-peak load. Alignment of the specimen and load train was maintained by a translation, rotation, and angularity adjustable alignment device clamped with a pneumatic actuator.

An improved alignment procedure was developed. The alignment procedure begins with the removal of the upper and lower load shafts, and replacement with threaded precision ground blocks. Two precision angles were then used to align the threaded blocks and load train, and the pneumatic alignment device was clamped. The load shafts and specimen/grip assembly were then installed. The alignment procedure was conducted after each test to verify alignment of the load train.

2.6 MODAL ANALYSIS

Initial testing of off-axis composites had demonstrated a material sensitivity to non-axial loads, and an attempt was made to minimize bending stresses. The dynamic response of the specimen and load train to a high frequency axial input must be considered when operating at the frequencies used for the tests. A modal analysis was performed to characterize the dynamic response of the specimen and load train to an axial force applied by the shaker. The modal analysis and spectrum processing program "Prism" by Anatrol was used to generate a representation of the dynamic modes occurring in the specimen.

Data acquisition was performed with a Hewlett Packard 3562A dynamic signal analyzer operating in burst random mode. Axial loading, corresponding to the signal analyzer command, was induced by the electrodynamic shaker. Forced accelerations in the direction of the loading axis were measured by the quartz force gage acting as the input or excitation transducer, and a tri-axial accelerometer measured both the in-plane and out-of-plane acceleration responses. Acquisitions of X, Y, and Z coordinate direction accelerations were performed at 52 points on the specimen and load train as shown in Fig. 7. The upper load train consisted of the force gage, load cell and pneumatic alignment device. The lower load train, below the specimen, consisted of a direct link to the electrodynamic shaker armature. Of the 52 points chosen to define the system geometry, point 1 was the input transducer (force gage) and accelerations were measured only in the Y coordinate direction. Accelerations of all other points were measured with the tri-axial accelerometer. The response/excitation measurements were analyzed over a frequency range of 0 to 600 Hz using a Fast Fourier Transform on the experimental data. Response peaks were most likely the result of the excitement of natural frequencies in the load train and electrodynamic shaker armature, and testing was avoided at these frequencies. The out-of-plane, Z coordinate direction, frequency response of the specimen to an axial load input is shown in Fig. 8. Peaks were noted at: 137 Hz, 330 Hz, and 408 Hz.

Figure 9(a-c) displays greatly exaggerated representations of the mode shapes which correspond to the three response peaks characteristic of the motion of the specimen and load train. Three different perspectives are shown of the dynamic response of the modeled geometry. Fig. 9(a) is a two-dimensional view of the XY or in-plane response, Fig. 9(b) is a two-dimensional view of the YZ or

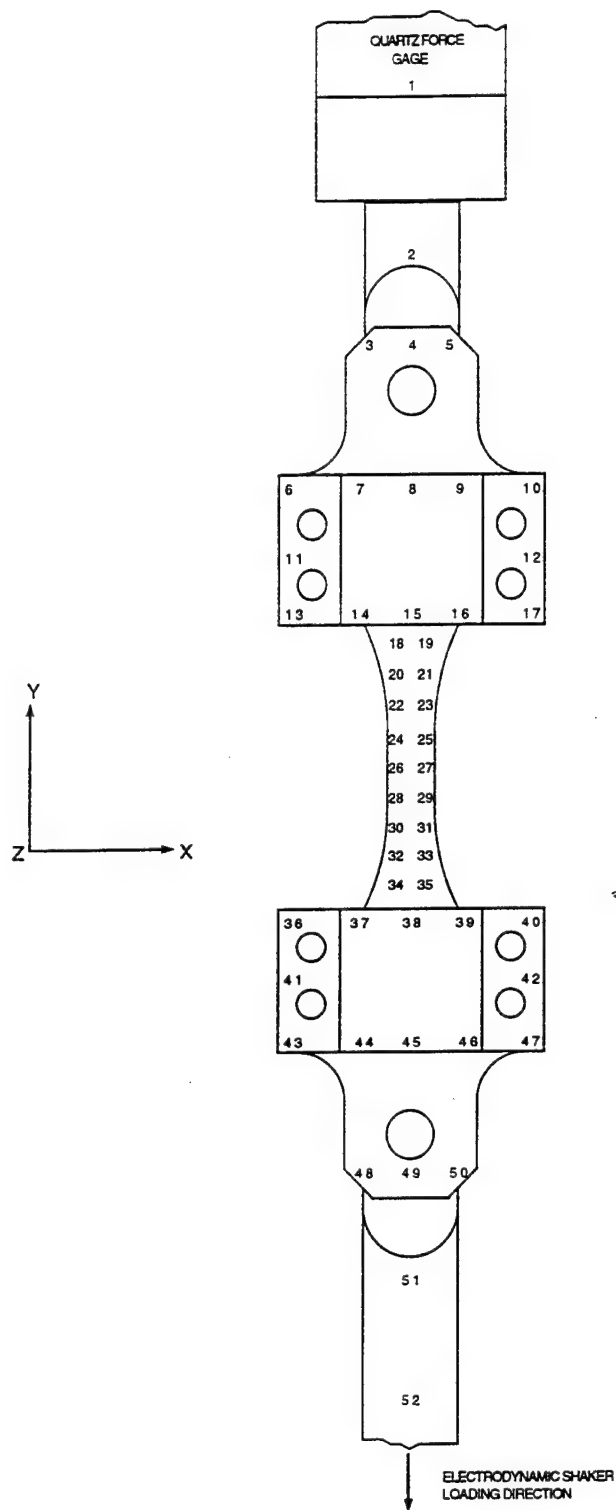


Fig. 7 Modal analysis geometry and accelerometer locations

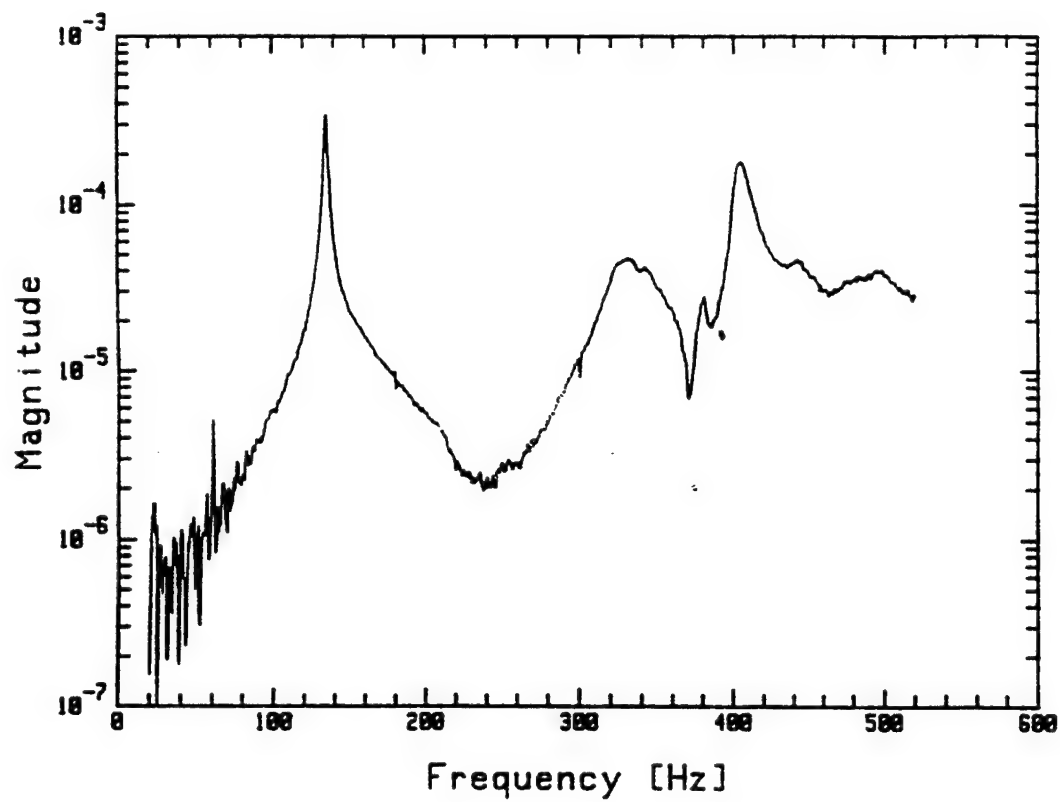


Fig. 8 Out-of-plane specimen frequency response

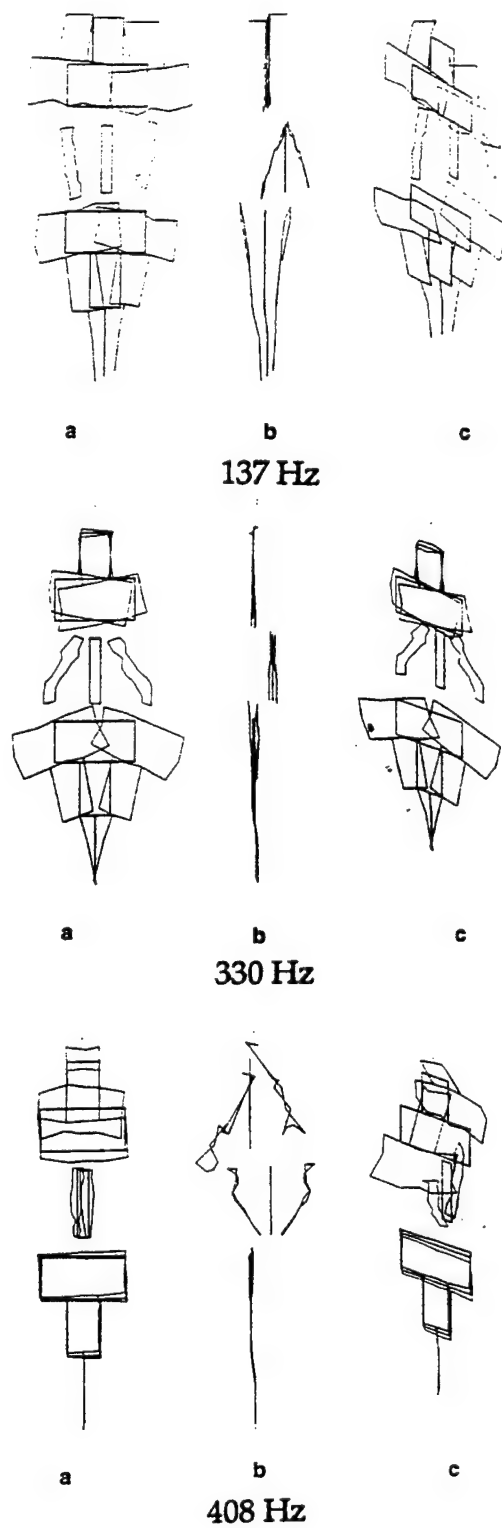


Fig. 9 Greatly exaggerated motions of the specimen and load train are shown representing characteristic modal shapes

out-of-plane response, and Fig. 9(c) displays an isometric or three dimensional view of the geometry. The 137 Hz response exhibits both in-plane and out-of-plane motion induced primarily by the lower load train and shaker armature. The 330 Hz response is reduced to in-plane motion produced by the lower load train. The 408 Hz response is primarily out-of-plane provoked by the response of the upper load train.

A 200 Hz testing frequency was selected because it displayed limited frequency response and will provide at least two orders of magnitude difference in frequency with the available low frequency data.

2.7 TEMPERATURE EQUIPMENT AND RESPONSE

Radiant heating was used to elevate the specimen temperature to 650°C or 815°C. A quartz bulb heating lamp was oriented horizontally on each side of the specimen which was oriented vertically in the test frame. The two heating zones consisted of the front and back of the specimen gage section, Fig. 10.

Thermocouples were spotwelded to the specimen to monitor the test temperature; however, thermocouple spotwelds were susceptible to failure due to the high frequency loading. For this reason, thermocouples spotwelded to the front and back of a dummy specimen in close proximity with the test specimen were used as lamp output control and provided the necessary feedback to accurately maintain the specimen temperature.

For temperature mapping purposes, thermocouples were spotwelded to the specimen and correlated to dummy specimen temperatures. The dummy specimen temperatures which corresponded to the test specimen at 650°C or 815°C were determined and acted as controlling setpoints during testing.

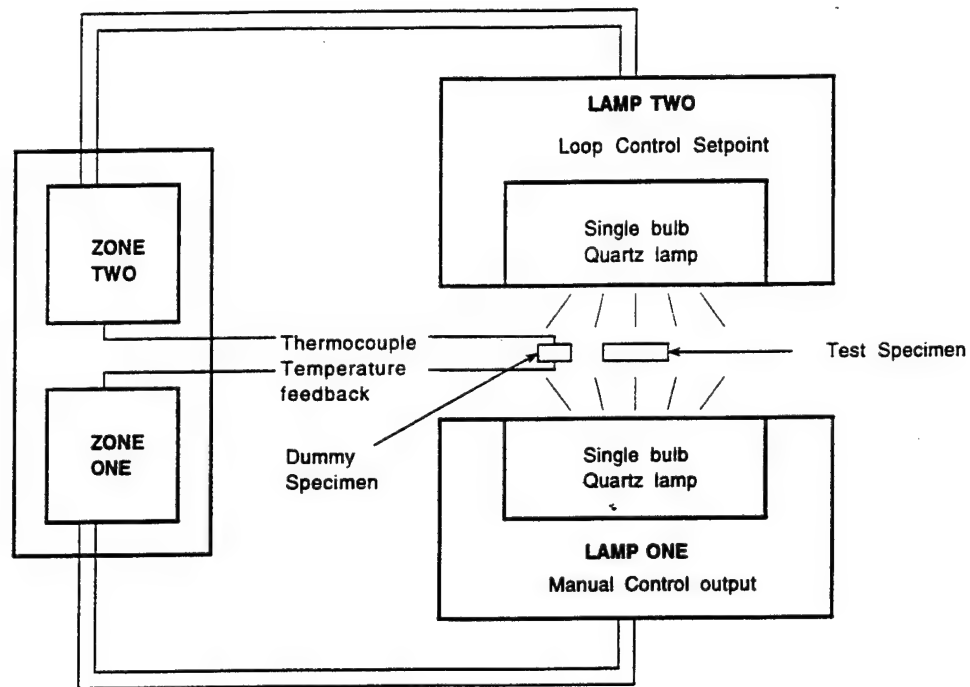


Fig. 10 Two zone control heating lamp schematic

The best temperature uniformity results were obtained when zone one was a fixed output, and zone two was in loop control for a given set point.

Temperature uniformity surveys were performed using type K 36 gage thermocouple wires spotwelded to an MMC specimen. Thermocouple temperatures were recorded and noted for repeatability. The two lamp, two zone control temperature survey of a MMC specimen is shown in Fig. 11 for both HF testing temperatures. The elevated temperature, 650°C or 815°C, peaks at the midpoint of the specimen and decreases to 600°C and 760°C respectively, 10 mm from the midpoint.

2.8 DAMAGE MONITORING EQUIPMENT

Electric potential change [12] was monitored with an automated system, also shown in Fig. 5, throughout selected tests. A 10 A current was passed through the specimen using a Hewlett-Packard 6033A power supply, and voltage drop along the length of the specimen was measured by a Hewlett-Packard 3478A multimeter for the duration of the test. Current leads, constructed of 1.0 mm NiCr wire, were spotwelded to the superalloy grip tabs on opposing sides of both the upper and lower grip as shown in Fig. 12. Direct current electric potential (DCEP) pickup leads were constructed of 36 gage type K thermocouple wire, and were spotwelded directly to the test specimen. Reduction of the initial DCEP voltage variation requires the consistent spacing of pickup leads. For this test program and specimen geometry, a distance of 50.8 mm along the longitudinal direction and the placement of leads across the thickness of the specimen was chosen to span the potential region of fracture. DCEP voltage measurements were recorded at mean load with no HF loading during periodic, operator determined interval, Data Acquisition Cycles (DAC).

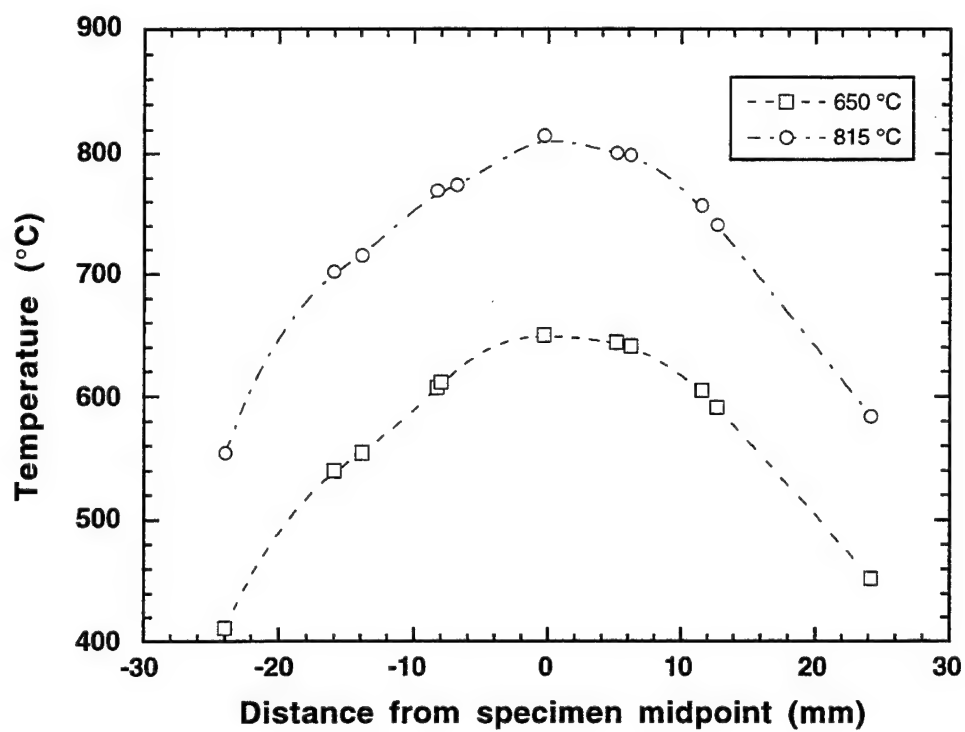


Fig. 11 Specimen temperature survey (midpoint = 0.0, dimensions in mm)

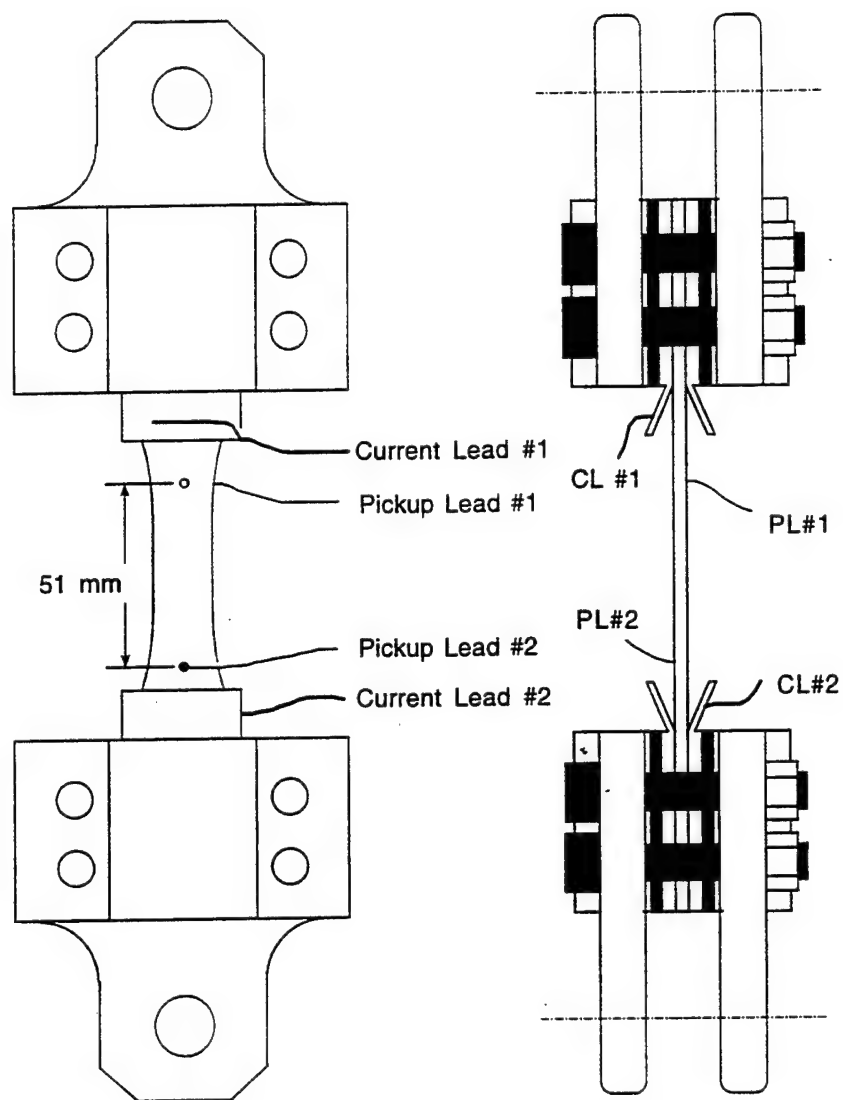


Fig. 12 Electric potential current and pickup lead configuration

It was noted that when the DCEP voltage increased substantially, and rapidly, toward the end of the fatigue life, the DAC could not respond rapidly enough to measure a significant number of data points and accurately portray the change in DCEP voltage. For this reason, a method of measuring DCEP voltage without interrupting the fatigue cycling of the test was developed.

2.9 DISPLACEMENT EQUIPMENT

An MTS high temperature extensometer was used to make initial elevated temperature elastic modulus measurements and then removed from the specimen prior to high frequency loading. Quartz rods with wedge shaped tips spanning the thickness of the specimen and spaced across a 12.7 mm gage length were used and periodic calibration of the extensometer ensured accuracy.

2.10 EXPERIMENTAL PROCEDURE

Specimens were aligned and clamped in the friction grips and then assembled in the aligned test frame. After spotwelding of the thermocouples and DCEP leads, and connecting the grip cooling, the specimen was heated to the temperature desired, 650°C or 815°C at approximately 1.0 °C/sec. The specimen was then held at temperature with grip cooling for 5 minutes, allowing the specimen to oxidize sufficiently in order to lower the emissivity and produce a stable temperature. Load-Displacement measurements were conducted at elevated temperatures prior to testing. The sinusoidal 200 Hz loading waveform was monitored throughout the test with an oscilloscope. Electric potential measurements were made on both an elapsed time and voltage change basis. Cycles-to-failure was recorded for each test, and specimen fracture into two pieces was defined as failure. One hundred hours at 650°C was chosen as runout based on the time-at-temperature projected for the envisioned

application. Some fatigue tests did not fail and were cycled in excess of the 100 hour runout. At 200 Hz, 100 hours represents 72 million cycles.

2.11 TEST CONDITIONS

All high frequency fatigue tests of SCS-6/Timetal®21S [0/90]_s were performed at 200 Hz in laboratory air at 650°C or 815°C. Stress range was varied from 180 MPa to 423 MPa at 650°C, and 180 MPa to 360 MPa at 815°C to obtain baseline fatigue life data, essential for the life prediction model, at a stress ratio of $R=0.1$.

To investigate the effect of frequency, the 200 Hz fatigue lives were compared to fatigue lives of 0.01 Hz and 1 Hz fatigue testing at similar stresses. The 0.01 Hz and 1 Hz low frequency testing was conducted by Steve Russ [13] of the Materials Directorate on a servo-hydraulic test frame, with the exception of a few 0.01 Hz tests conducted by Mike Castelli [14] at NASA-Lewis.

The residual strength of the material when subjected to hold times at temperature was investigated. Four specimens were exposed to 100 hour hold times at 650°C or 815°C with no load. Following thermal exposure, the specimens were failed statically in tension at their exposure temperature to determine the residual strength.

To study the effect of stress-ratio, several high frequency tests were conducted with $R= 0.5$, and 0.8 at 650°C and 815°C.

SECTION 3

RESULTS

3.1 FATIGUE LIFE RESULTS

Eighteen high frequency fatigue tests on $[0/90]_S$ composites were conducted and the test conditions and cyclic fatigue life results for all 200 Hz tests are shown in Table 1.

The effect of frequency was studied by comparing the high frequency cyclic lives to that of 0.01 Hz and 1 Hz low frequency isothermal fatigue test data in Tables 2 and 3, respectively.

For modeling purposes, tensile and creep test results which were used in the analysis are shown in Tables 4, 5 and 6, respectively [15].

3.2 FIBER VOLUME FRACTION NORMALIZING PROCEDURE

The fiber volume fraction of a fiber reinforced composite can greatly influence the measured results. For example, at elevated temperature, the ultimate strength is strongly dependent upon the fiber strength and fiber volume fraction. Fatigue testing was predominantly conducted with specimens from plates containing a volume fraction of 0.38; however, creep tests and one fatigue test were conducted with material containing a fiber volume fraction of only 0.32. To compare results of specimens containing differing volume fractions, the experimentally applied stress was standardized through a rule-of-mixtures (ROM) technique. The normalizing procedure relates the volume fraction of

matrix and fibers, and their respective strengths, to an experimentally measured composite ultimate strength.

TABLE 1

200 Hz FATIGUE TEST RESULTS ON [0/90]_s SCS-6/TIMETAL®21S

Specimen ID	Stress ratio	Max Stress (MPa)	Temperature (°C)	Cycles to Failure (Nf)
92-598	0.1	200	650	7.20E+07*
92-607	0.1	250	650	1.50E+08*
92-600	0.1	300	650	1.04E+06
92-451	0.1	300/320**	650	4.08E+05
92-602	0.1	400	650	1.30E+05
92-606	0.1	470	650	1.87E+04
92-608	0.5	345	650	8.7936e+06
92-610	0.5	450	650	2.0275e+05
92-611	0.8	425	650	7.40E+07*
93-449	0.8	475	650	3.9965E+07
92-601	0.1	200	815	4.09E+06
92-604	0.1	300	815	9.00E+05
92-605	0.1	400	815	6.14E+04
92-609	0.5	293	815	7.20E+07*
92-612	0.5	345	815	3.5424E+06
92-599	0.5	440	815	1.6953E+06
92-161	0.8	450	815	6.5332E+05
93-160	0.8	500	815	9462

* Tests which did not result in failure.

** Experimentally applied stress / Effective applied stress.

TABLE 20.01 Hz FATIGUE TEST RESULTS ON [0/90]_s SCS-6/TIMETAL®21S

Specimen ID	Stress ratio	Max Stress (MPa)	Temperature (°C)	Cycles to Failure (Nf)
92-552	0.1	570	650	1340
92-553	0.1	470	650	3151
92-395	0.1	400	650	10000*
Nasa-Lewis	0.0	450	650	2316
Nasa-Lewis	0.0	400	650	6984
Nasa-Lewis	0.0	350	650	29000
92-588	0.1	425	815	621
92-554	0.1	350	815	1011
92-586	0.1	275	815	6154

* Tests which did not result in failure.

TABLE 31 Hz, FATIGUE TEST RESULTS ON [0/90]_s SCS-6/TIMETAL®21S

Specimen ID	Stress ratio	Max Stress (MPa)	Temperature (°C)	Cycles to Failure (Nf)
92-112	0.1	570	650	3,097
92-113	0.1	350	650	577,707
92-114	0.1	425	650	18,405
92-116	0.1	470	650	11,965
92-119	0.1	250	650	1,002,000*
92-120	0.1	300	650	153,447
92-128	0.1	300	650	152,791
92-129	0.1	400	815	7,866
92-117	0.1	275	815	82,700
92-115	0.1	225	815	24,643
92-118	0.1	225	815	24,097
92-111	0.1	347	815	4,329

* Tests which did not result in failure.

TABLE 4
TENSILE TEST RESULTS ON [0/90]_s SCS-6/TIMETAL®21S

Specimen ID	Temperature (°C)	Ultimate Strength (MPa)
91-597	650	698.0
91-217	650	644.0
92-214	650	631.0
92-218	815	495.0
92-213	815	479.0
92-544	815	456.0

TABLE 5
CREEP TEST RESULTS ON [0/90]_s SCS-6/TIMETAL®21S

Specimen ID	Temperature (°C)	Max Stress (MPa)	Time to Failure (s)
92-540	650	425/502.6**	6.480E+04
92-094	650	400/438**	2.998E+05
92-097	815	400	14,000
92-603	815	379.5	7.9E+05*
92-603A	815	310.5	7.686E+05

* Tests which did not result in failure.

** Experimentally applied stress / Effective applied stress.

TABLE 6
TENSILE TEST RESULTS ON TIMETAL®21S

Specimen ID	Temperature (°C)	Strain Rate 1/s	Ultimate Strength (MPa)
92-449	650	833.0E-6	362
91-184	650	83.3E-6	245
92-474	650	8.33E-6	126

An effective applied stress was obtained using a rule-of-mixtures relation to determine an effective ultimate strength. This relation is given as:

$$\sigma_{ult} = \left(\frac{V_f}{2} \right) (\sigma_f) + \left(1 - \frac{V_f}{2} \right) (\sigma_m) \quad (3.1)$$

where σ_{eff} is the composite ultimate tensile strength, V_f is the fiber volume fraction, σ_f is the stress in the fiber, and σ_m is the stress in the matrix.

Matrix material ultimate strength was noted to be influenced by the tension test strain rate, and supplemental tensile results are shown in Table 6. Therefore, matrix material ultimate tensile strength values, recorded at the highest strain rate, 833.0E-6/s, were used to normalize the HF data which achieved strain rates greater than 0.60/s, and the lowest strain rate, 8.33E-6/s tensile data were used to normalize the creep data.

The fiber volume fraction of the composite material, V_f , was computed including all fibers in the layup, [0] and [90]. Only the [0] fibers are considered to contribute to the strength of the composite in the loading direction. Therefore, the volume fraction of [0] fibers was represented in (3.1) by one-half of the total fiber volume fraction, or $V_f/2$. It was presumed that when calculating [0] fiber

volume fraction from total volume fraction, there will be negligible change in strength for small variations in volume fraction.

The maximum stress in the fibers was found using the ROM relation (3.1) between the average experimentally determined composite ultimate tensile strength for a known volume fraction (Table 3), and the ultimate strength of the matrix at a representative strain rate. For example, specimen 91-217 (Table 4), having a volume fraction of 0.343 and an ultimate tensile strength of 644.0 MPa. Considering the HF test conditions, the matrix material ultimate strength of specimen 92-449 (Table 6), at a strain rate of 833.0E-6/s was 362 MPa. This results in an ultimate fiber strength of 2006 MPa.

A prediction of the ultimate tensile strength as a function of volume fraction was then computed for specimen 92-451 from equation (3.1), using the previously determined constituent ultimate strengths at 650 °C ($\sigma_f = 2006$ MPa, $\sigma_m[\text{HF fatigue}] = 362$ MPa, $\sigma_m[\text{Creep}] = 126$ MPa). The constituent strengths, and a volume fraction of 0.38 results in a predicted ultimate strength of 674.4 MPa.

The effective applied stress was then calculated for a volume fraction of 0.38, and found to equal 320 MPa, through a relation knowing the experimentally applied stress, volume fraction, and the ultimate strengths at the respective volume fractions as shown in equation (3.2).

$$\sigma_{\text{normalized}}^{(v_f=0.38)} = \frac{\sigma_{\text{applied}}^{(v_f=0.31)}}{\sigma_{\text{uts}}^{(v_f=0.31)}} \sigma_{\text{uts}}^{(v_f=0.38)} \quad (3.2)$$

Applied stress data which have been standardized are noted in the test results tables.

3.3 DISCUSSION OF 650°C FATIGUE LIFE RESULTS

Fatigue life data were most easily compared at a given test temperature. The results of all 650°C high and low frequency fatigue tests are illustrated in Fig. 13, on a normalized stress range vs. cycles-to-failure plot. The three high frequency and one 1 Hz lives which were not failures, are denoted by horizontal arrows. Tests conducted at a stress ratio of 0.1 are ordered by frequency, with the high frequency tests accumulating more cycles prior to failure. Although the 200 Hz and 0.01 Hz tests differed in frequency by over four orders of magnitude, cyclic lives varied by less than one order of magnitude. By definition, purely cycle dependent behavior results in identical cyclic fatigue lives for similar conditions, regardless of frequency. This suggests that the 650°C fatigue lives are primarily cycle dependent. Fatigue lives, however, do display some frequency dependence exemplified by the approximate factor of five difference in fatigue lives between tests conducted at 0.01 Hz and 200 Hz with a stress range of 350 MPa.

Two hundred Hertz high frequency data are also shown from tests conducted at stress ratios of 0.5 and 0.8. As expected, cyclic life decreases with an increase in mean stress for a given value of stress range, resulting in the 200 Hz fatigue-life data layering according to mean stress.

In order to quantify the effect of mean stress, cyclic lives having similar stress ranges and varying stress ratios should be compared. However, experimental data at the same stress range were not available. Projected values for each stress ratio are shown at one cycle, and are the equivalent maximum stress ranges corresponding to the ultimate strength. Interpolating from the experimental data to the projected values, provides a $R=0.5$ data value with a similar stress range, 270 MPa, to the $R=0.1$ experimental data. At a stress range

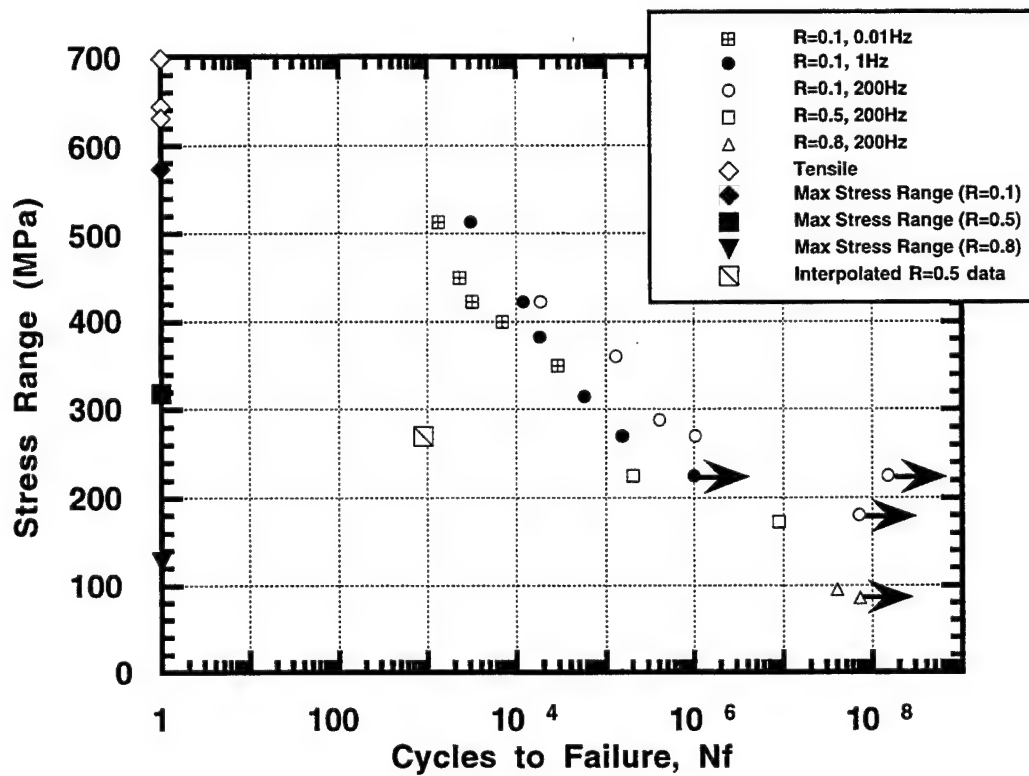


Fig. 13 650°C Fatigue Life Results of SCS-6/Timetal®21S [0/90]_s

of 270 MPa, a factor of 2.5 increase in mean stress from 165 MPa to 405 MPa, results in a decrease in the fatigue life of three orders of magnitude.

The 650°C fatigue life data are shown on a stress range vs. time-to-failure basis in Fig. 14. If fatigue lives were purely time dependent, all data would collapse into a single line. If data were purely cycle dependent, time-to-failure lives would vary over four orders of magnitude ($2.0\text{E}+4$). Comparing 200 Hz and 0.01 Hz data at a stress range of 350 MPa, fatigue life data varies by approximately $4.0\text{E}+03$. This variation is the result of the factor of 5 variation attributed to frequency dependence on the cycles-to-failure plot. This comparison again suggests that the fatigue lives on a time-to-failure basis are predominantly cycle dependent and display a slight frequency dependence. The four tests which did not result in specimen fracture suggest that an endurance limit exists for this material at 650°C.

To better understand the influential factors, a plot of the maximum stress vs. time to failure is shown in Fig. 15. Plotting the maximum stress allows the inclusion of creep data. Comparisons can be made between creep results and fatigue tests at a stress ratio of 0.8. At high stress ratios, the stress range is relatively small compared to the mean stress creating fatigue test conditions similar to a creep test. Fatigue tests at similar maximum stresses have slightly increased lives compared to the creep results.

Plotting cyclic fatigue lives as a function of maximum stress also indicates that maximum stress is not the governing factor for the endurance limit. Talreja [4] described the endurance limit of composites to be the same as the maximum strain corresponding to the fatigue limit of the matrix. As shown in Fig. 15, a test having a stress ratio of 0.8, and a maximum stress of 400 MPa did not fail even though failures occurred at lower maximum stresses and their resulting

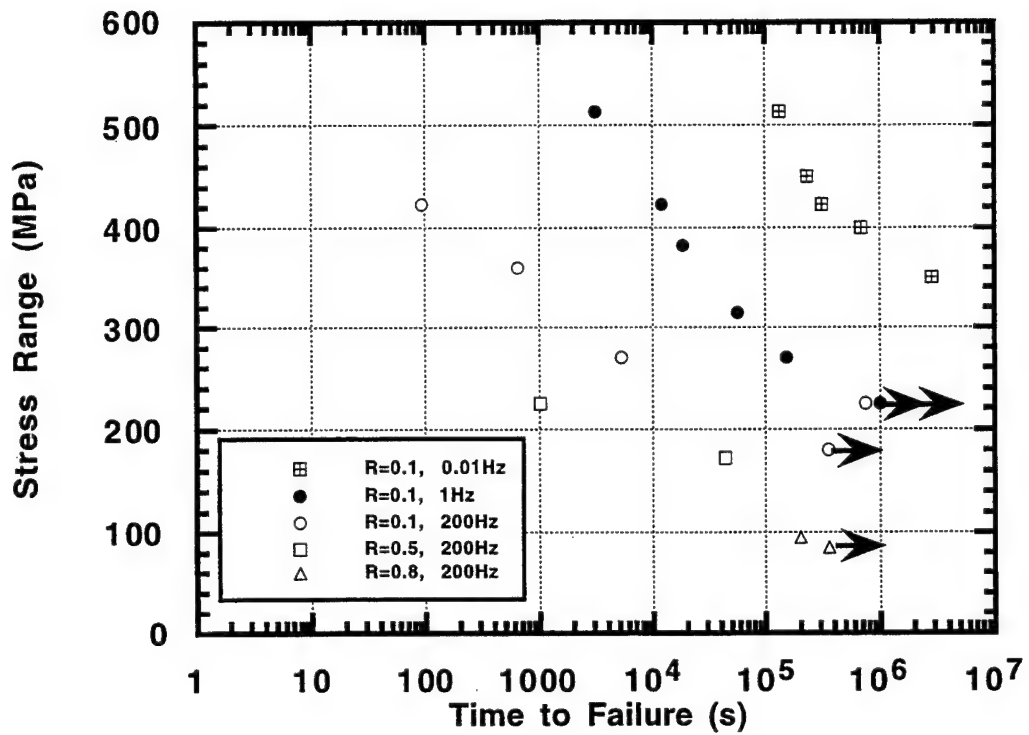


Fig. 14 650°C SCS-6/Timetal®21S [0/90]_S fatigue life time to failure results

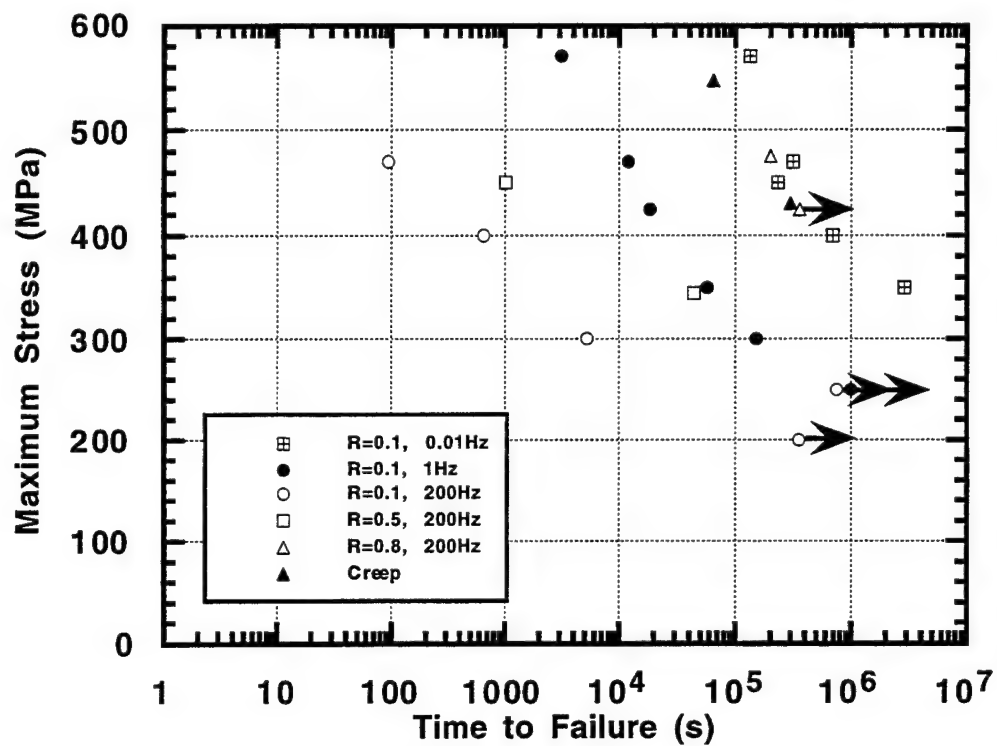


Fig. 15 650°C SCS-6/Timetal®21S [0/90]_S, maximum stress vs. cycles to failure fatigue life results

reduced maximum strains. The endurance limit of the cross-ply material of interest is not simply a function of maximum stress or strain, but is influenced by other parameters.

Goodman diagrams are presented in Figs. 16 and 17 for 650°C and 815°C fatigue life results, respectively, as a method to interpret the combined effects of mean stress and stress range as a criterion for failure. The mean stress or X-axis intercept of the Goodman line is determined by the ultimate strength of the material, and the Y-axis intercept was determined through an empirical fit of the Goodman line to the data. Combined alternating and mean stress conditions which do not exceed the Goodman line will result in test conditions below the materials endurance limit and fracture will not occur. The experimental results agree with the Goodman line failure criterion shown in Figs. 16 and 17.

3.4 DISCUSSION OF 815°C FATIGUE LIFE RESULTS

The results of all fatigue tests conducted at 815°C are shown in Fig. 18 on a stress range vs. cycles-to-failure basis. The frequencies for these tests covered four orders of magnitude, and the fatigue lives varied by three orders of magnitude for a given stress range. Fatigue lives are ordered by frequency, with the 200 Hz tests accumulating the most cycles prior to failure. When plotted on a time-to-failure basis, as shown in Fig. 19, lives vary over two orders of magnitude at a given stress range. If fatigue life were purely cycle or time dependent, variation would not be present at a given stress range, on a cycles-to-failure or time-to-failure plot, respectively.

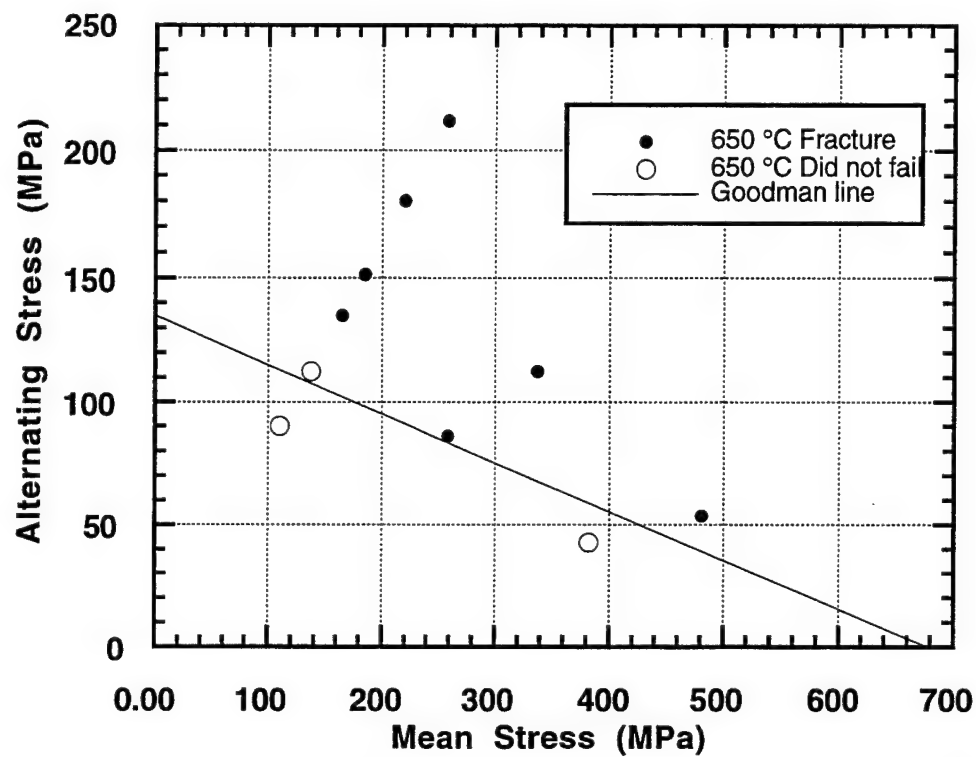


Fig. 16 Goodman Diagram, SCS-6/Timetal®21S [0/90]_s at 200 Hz and 650°C

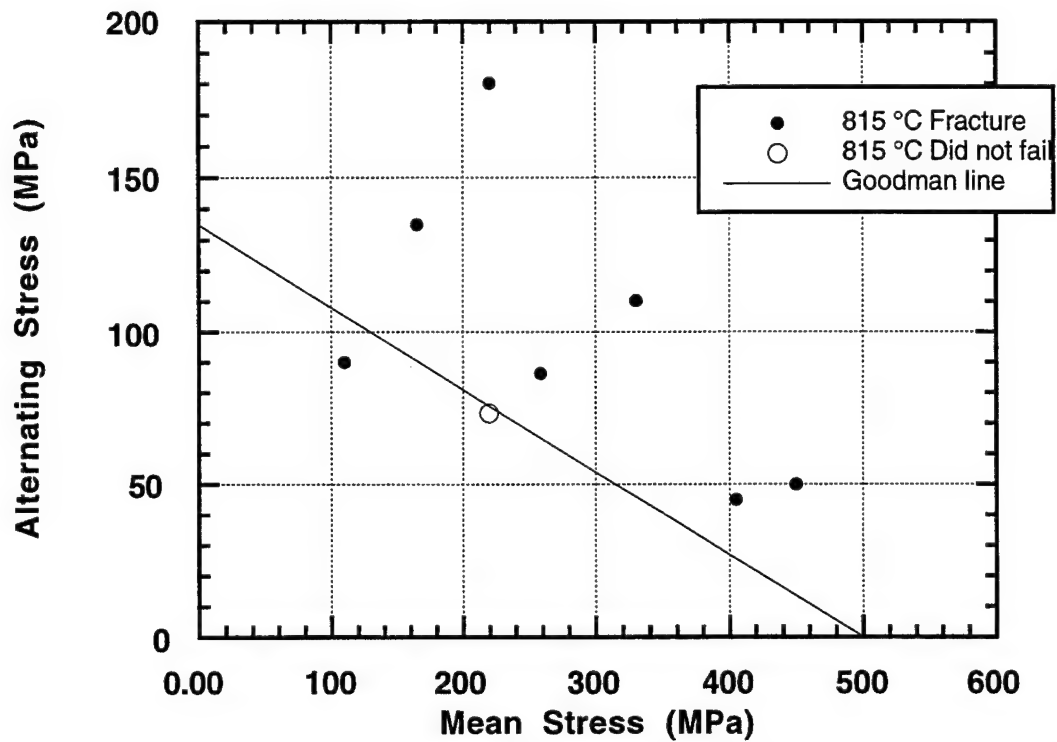


Fig. 17 Goodman Diagram, SCS-6/Timetal®21S [0/90]_S at 200 Hz and 815°C

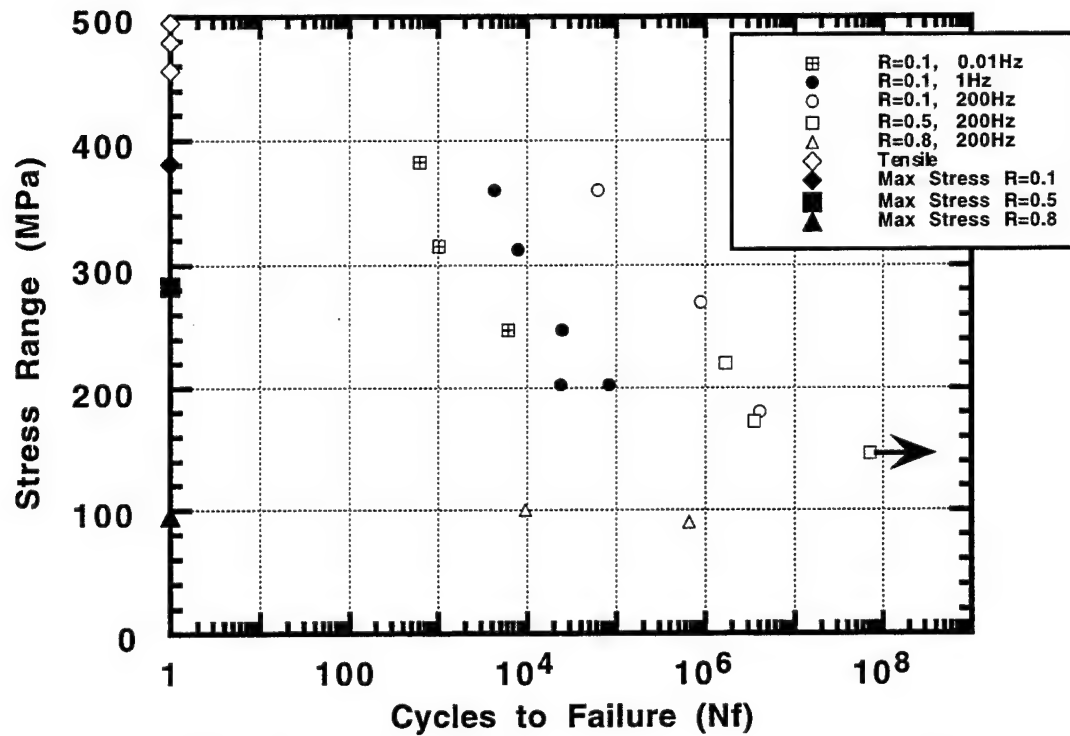


Fig. 18 815°C SCS-6/Timetal®21S [0/90]_S, stress range vs. cycles to failure fatigue life results

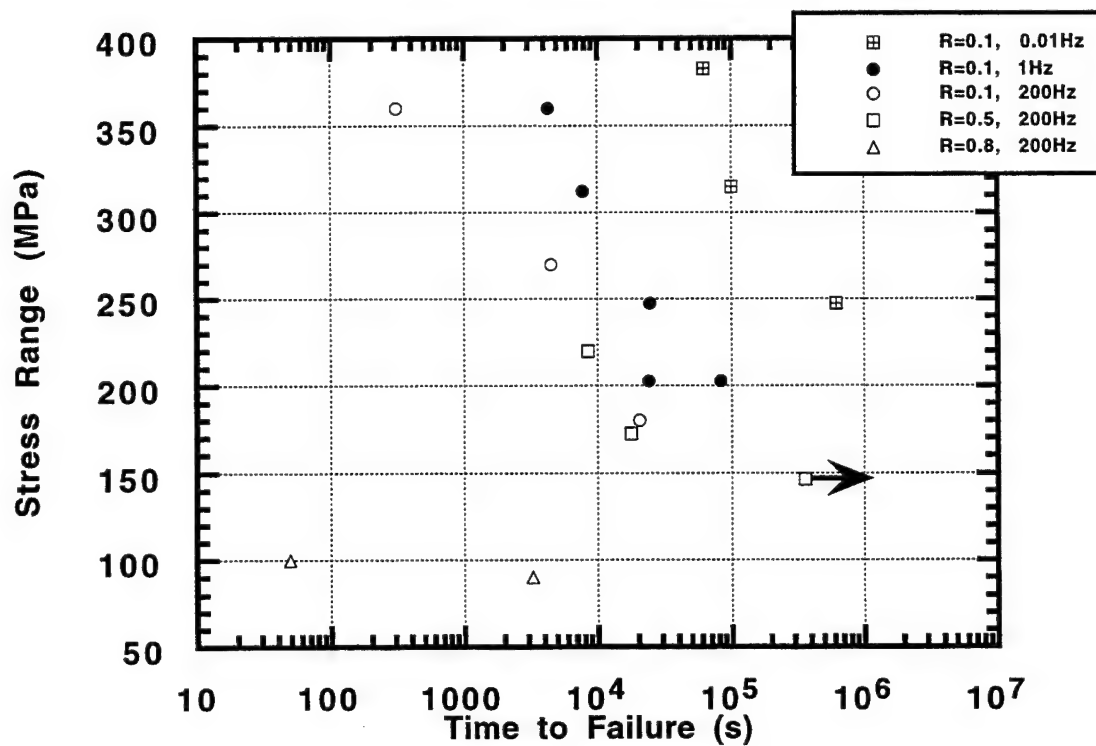


Fig. 19 815°C SCS-6/Timetal®21S [0/90]_s, Stress range vs. time to failure fatigue life results

High frequency fatigue lives at 650°C and 815°C at $R=0.1$ are shown in Fig. 20. These results indicate that time dependent effects have negligible influence on life at or above 300 MPa. Only at stresses below 300 MPa, where the fatigue life is of sufficient length to allow environmental degradation to occur, are 815°C lives shorter than 650°C lives, and time dependent effects become notable.

3.5 RESIDUAL STRENGTH MEASUREMENTS

Because of the significant number of tests which did not result in failure and the indication of time dependent influences, the ultimate strength of the composite was measured after a 100 hour thermal exposure at 650°C or 815°C under no load. Residual strength tensile tests were conducted after thermal exposure to investigate environmental degradation and its effect on strength. Straight sided specimens, 12.7 mm in width, were held in air cooled friction grips in the HF test setup for 98 hours. Specimens were then held at elevated temperature for 2 hours in a horizontal frame machine, followed by a tensile test at elevated temperature. Strain control was used with a strain rate of $83.3E-6/s$. Residual strength measurements are shown in Table 7. The ultimate strengths of the exposure specimens exceed those recorded without thermal exposure. Revelos [16] noted a reduction in UTS of 45% after 138 hour exposure, however, residual strength measurements were made at room temperature rather than the elevated exposure temperature.

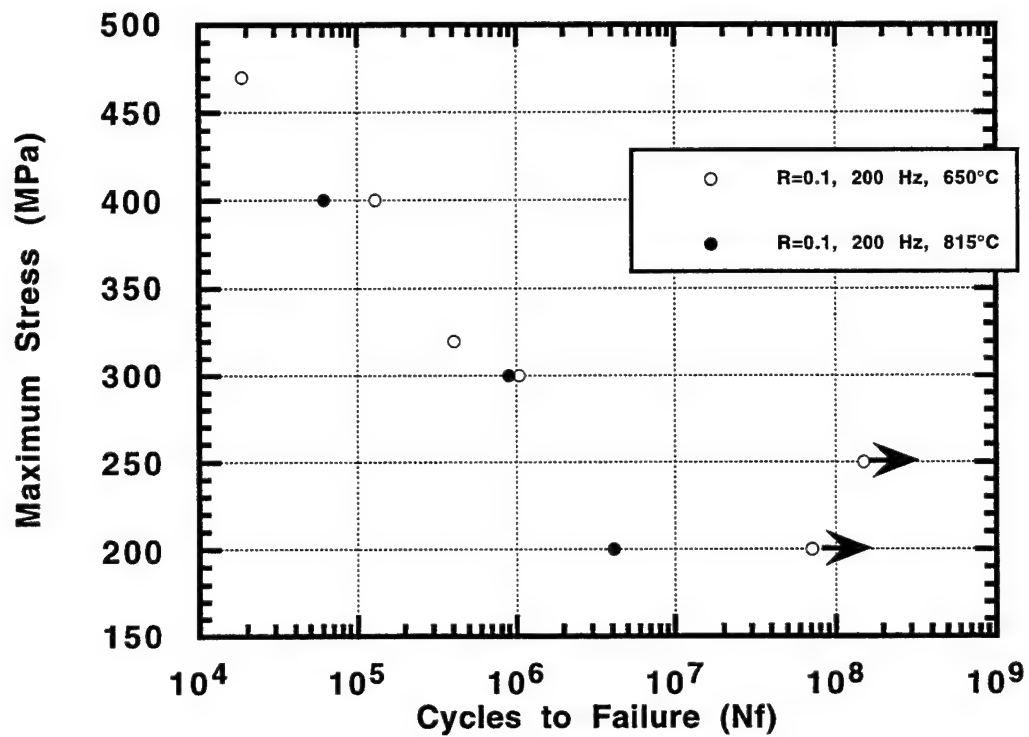


Fig. 20 650°C, 815°C SCS-6/Timetal®21S [0/90]_S fatigue life comparison

Table 7

RESIDUAL STRENGTH AFTER 100 HOUR THERMAL EXPOSURE

Specimen ID	Temperature (°C)	Strain Rate 1/s	Ultimate Strength (MPa)
91-592	650	83.3E-6	798.7
91-593	650	83.3E-6	786.5
92-594	815	83.3E-6	554.7

The residual strength results indicate that the composite material ultimate strength was not reduced by thermal exposure at 650°C, but rather increased by approximately 15 %. This indicates the strength of the [0] fibers was maintained during exposure.

SECTION 4

PHYSICAL OBSERVATIONS

4.1 FATIGUE DAMAGE MECHANISMS

Fatigue damage in MMCs is a complex process influenced by the properties of the fiber, matrix, and fiber/matrix interface. To better understand the nature of the damage mechanisms influencing the fatigue behavior of the cross-ply SCS-6/Timetal®21S composite, selected high frequency test specimens were inspected using post-test fractography and metallography. These techniques provided insight into the damage mechanisms leading to specimen fracture. Fatigue damage was the result of several factors inherent to titanium matrix composites (TMC). When subjected to elevated temperature fatigue, microstructural evolution of the matrix, degradation of the fiber/matrix interface, and matrix cracking were noted to contribute to the damage process.

4.2 MICROSTRUCTURAL EVOLUTION

Timetal®21S is a metastable beta titanium alloy, and its mechanical properties are affected by aging which occurs during elevated temperature exposure. Following the heat treatment at 620°C, the microstructure is made up of homogeneously nucleated, fine alpha phase in the beta matrix [16]. Exposure of the the matrix to elevated temperatures in air has been shown to result in material aging and precipitation of the alpha phase [8, 16, 17, 18]. This precipitation was shown to significantly effect matrix ductility and influence material behavior.

To determine the microstructural changes as well as damage evolution which took place in the matrix during elevated temperature testing, selected specimens were used for fractographic and metallographic analysis. One-half of the fracture surface was preserved for fractography, while the other half was sectioned longitudinally, parallel to the [0] fibers and perpendicular to [90] fibers, for metallography. Longitudinal sections were mounted, polished, and examined using optical microscopy.

The microstructural changes which took place in the specimens tested at elevated temperature will be discussed first since material property changes influence the development of fatigue damage. The as-received microstructure, Fig. 21, is made up of uniformly dispersed, fine alpha and beta phase. Significant microstructural changes occurred in specimens subjected to isothermal fatigue at 650°C for less than 1 hour, as shown in Figs. 22 and 23. The micrographs shown are the microstructure at specimen mid-width and reflect the changes which occurred in the heated zone gage section. Aging at 650°C results in the precipitation of alpha phase at the grain boundaries and in the interior of the beta grains. The resulting heterogeneous nucleation of the alpha phase creates a precipitate free zone (PFZ) identified by the lighter region contrasting with the dark alpha shown in Fig. 22. The presence of oxygen was demonstrated to encourage the formation of alpha on the surface of thermal exposure specimens [16]. Alpha phase precipitation was also observed on the specimen surface in isothermal fatigue specimens as shown in Fig. 23. However, with the exception of a surface oxide layer and microstructural change, little environmental damage was noted in 1 hour at 650°C.

A greater amount of oxidation was observed on micrographs from extended 100 hour 650°C exposure specimens. Oxidation of the carbon-carbon interfacial coatings of [90] fibers was prevalent, as shown in Fig. 24, and

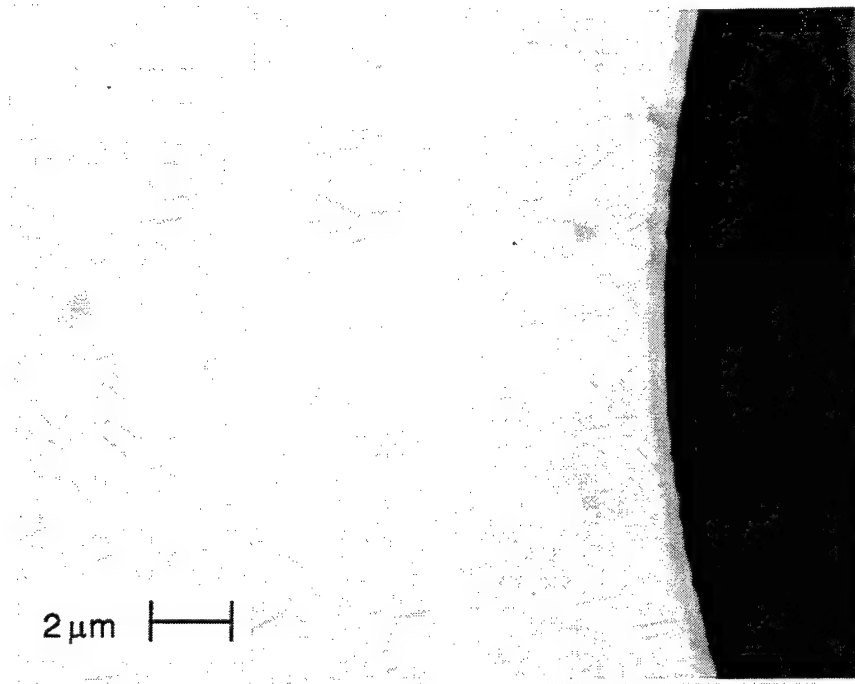


Fig. 21 As-received microstructure

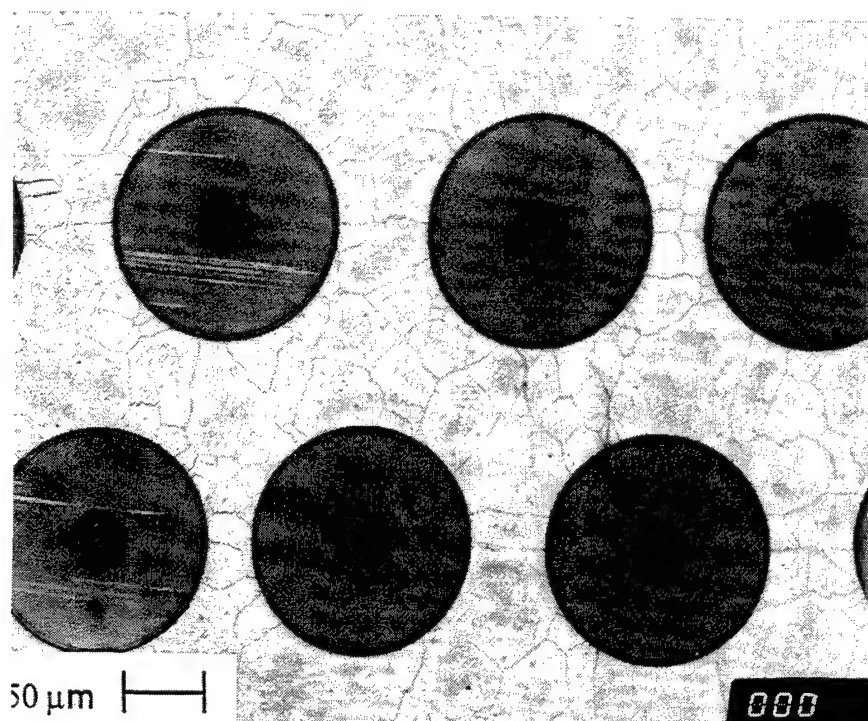


Fig. 22 Mid-thickness microstructure after 650°C exposure for less than 1 hr

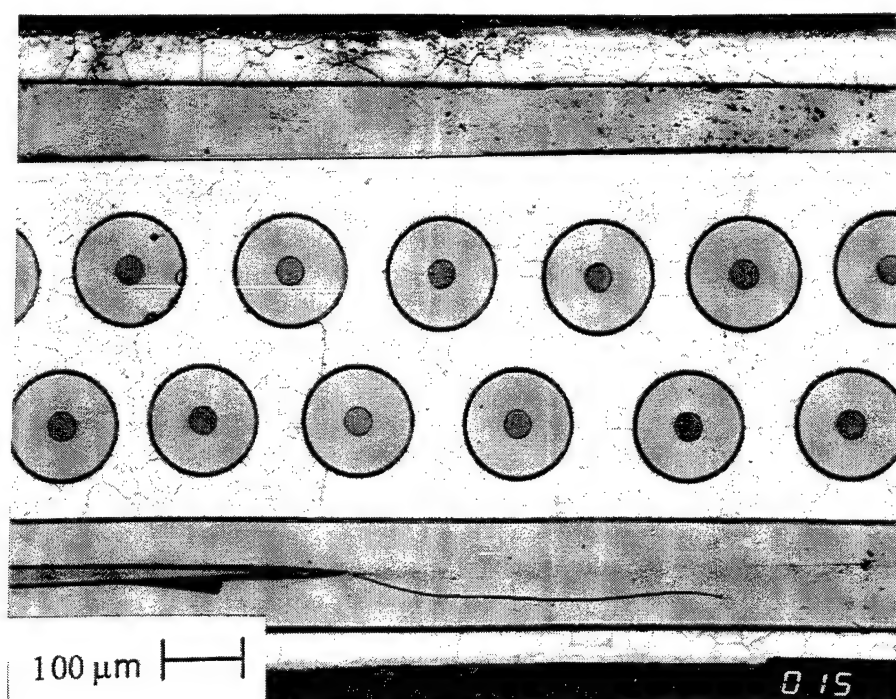


Fig. 23 Alpha-phase precipitation on the specimen surface after 650°C exposure for less than 1 hr

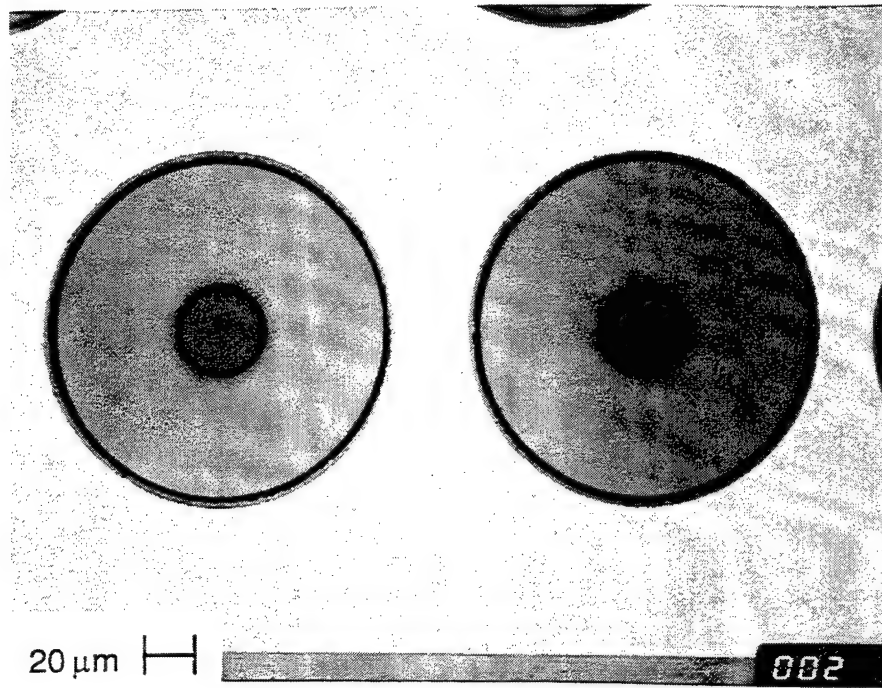


Fig. 24 Oxidation damage of the fiber/matrix interface on SCS-6 fibers subjected to 100 hr exposure at 650°C

numerous monofilament fiber cores were damaged or absent from the [90] fibers, similar to observations made in thermal fatigue studies [16].

Figures 25 and 26 are mid-width micrographs of a specimen subjected to isothermal fatigue at 815°C for less than 1 hour. The micrograph of the longitudinally sectioned specimen in Fig. 25 indicates that the primarily beta grain microstructure includes residual alpha stabilized by oxygen. Interspersed particles throughout the beta grains were identified by W. Jones, using energy dispersive spectroscopy (EDS), to be diffused TiC reaction product from the carbon coatings of the fibers [16]. The presence of oxygen at the surface of the specimen promoted the precipitation of alpha phase along with the oxide film shown in Fig. 26.

4.3 FATIGUE DAMAGE OBSERVATIONS

The presence of [90] fibers has been reported to substantially reduce composite strength [3, 5, 19, 20]. The high strength titanium matrix requires an equally strong fiber/matrix interface to transfer the load from the matrix to the [90] fiber. In review, the fiber and matrix are separated by two carbon coatings on the fiber. Interfacial failure was shown to occur at each layer of the interface. Fig. 27 (a) depicts the separation of the SCS-6 fiber from the first carbon coating, Fig. 27 (b) shows debonding of the carbon-carbon layers, and Fig. 27 (c) shows the failure of the matrix reaction zone and carbon coating. Fatigue damage was observed to initiate at the failed fiber/matrix interface, and proceed as follows.

Matrix cracking initiated at the [90] fibers as shown in Figure 28, and propagated perpendicularly to the loading axis. Cracks from neighboring [90] fibers were then observed to link and propagate toward the [0] plies as shown in Figs. 29 and 30 for 650°C and 815°C conditions, respectively. Matrix cracks were observed to be transgranular at 650°C, Fig. 29, due to the brittle alpha

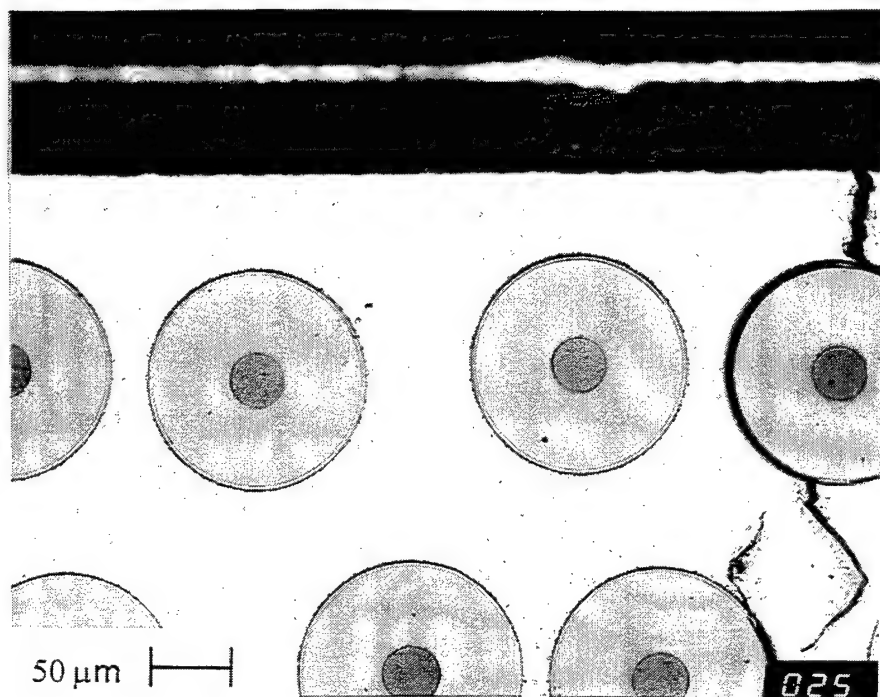


Fig. 25 Microstructure of specimen subjected to 815°C exposure for less than 1 hr

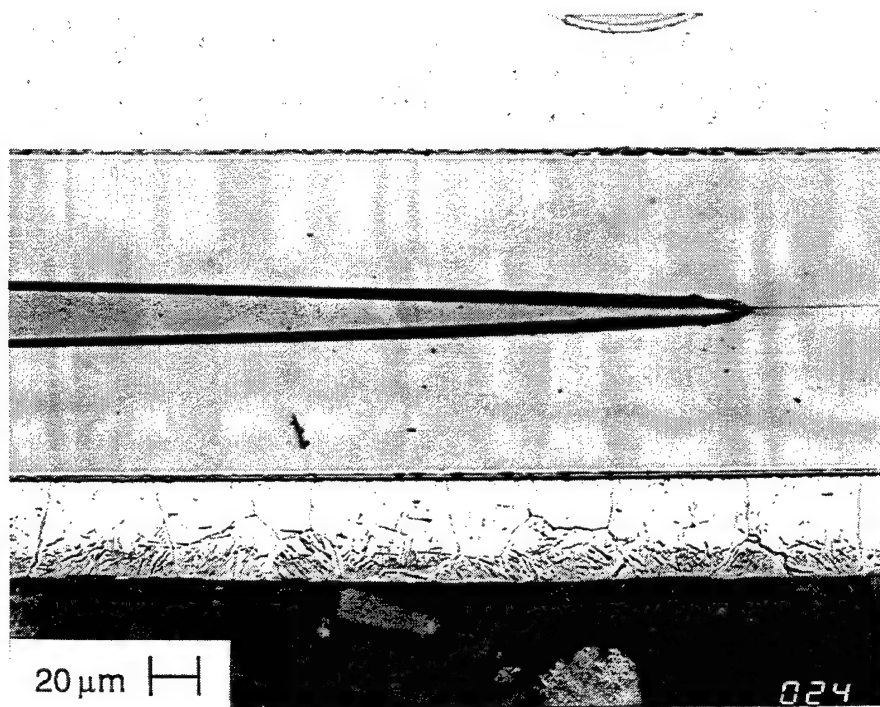
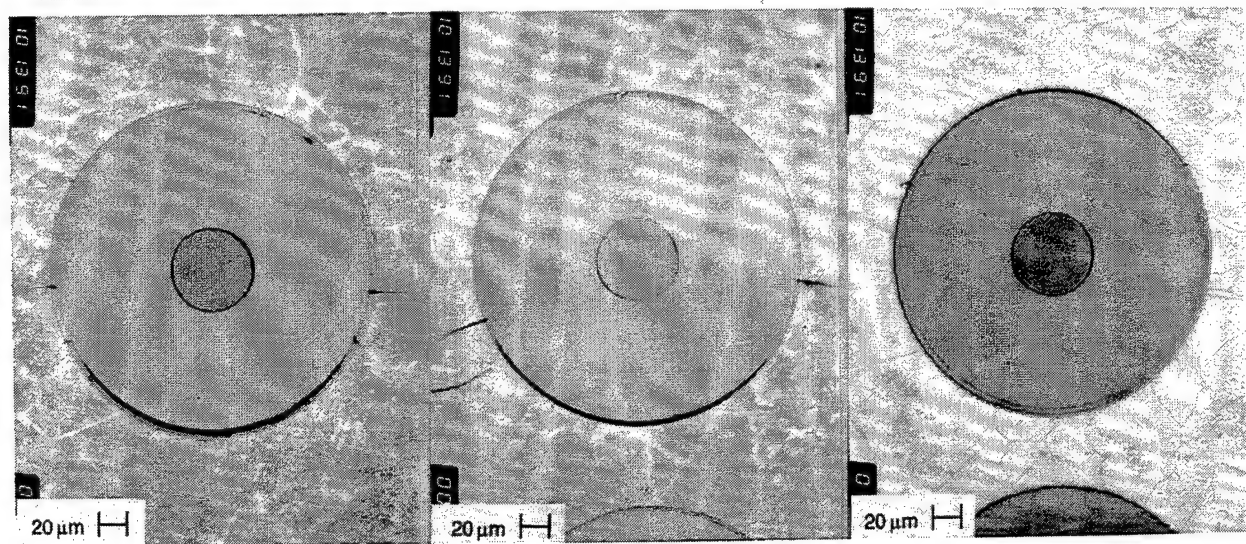


Fig. 26 Alpha phase precipitation on the surface of a specimen subjected to 815°C exposure for less than 1 hr



a.

b.

c.

Fig. 27 Fiber/Matrix interface failure at each interfacial layer

(a) debonding of first carbon coating

(b) debonding between carbon coatings

(c) debonding of carbon coating and matrix

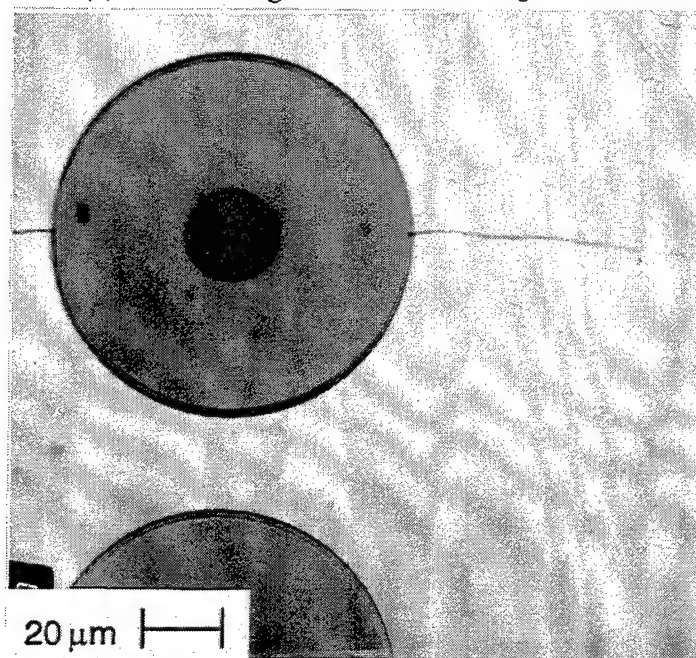


Fig. 28 Matrix crack initiation at [90] fibers

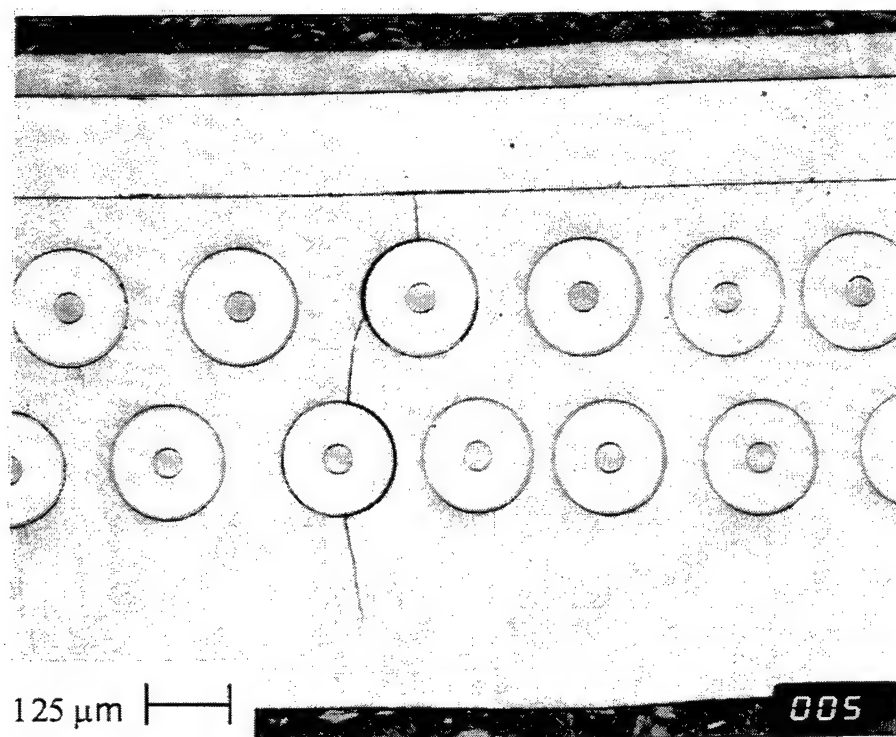


Fig. 29 650°C transgranular fatigue crack propogation

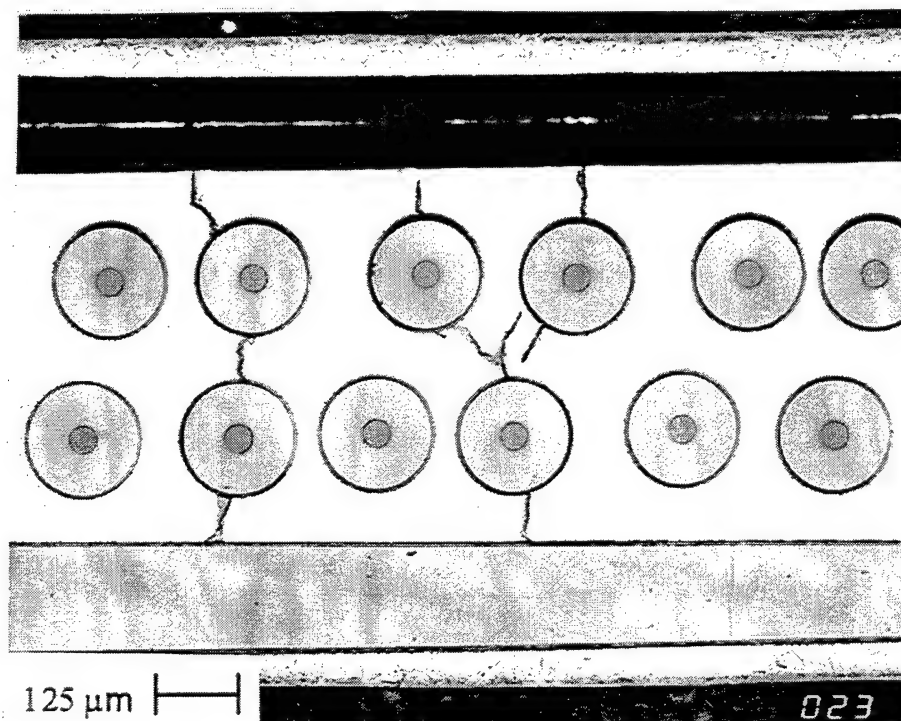


Fig. 30 815°C intergranular fatigue crack propogation

precipitated in the beta grains. The irregular cracking path in Fig. 30 was due to the residual alpha phase on the beta grain boundaries promoting intergranular cracking at 815°C. The internal crack surfaces precipitated alpha phase indicating the presence of oxygen through the width of the specimen and into the internal matrix cracks. Matrix crack propagation into the [0] plies leads to local interfacial oxidation and degradation, Figs. 31, and 32, 650°C and 815°C, respectively, and the eventual failure of the [0] fibers.

Several fatigue tests did not result in specimen fracture as noted in Table 1. Metallographic sectioning of these specimens displayed no indication of fiber/matrix interface debonding or matrix crack initiation.

4.4 FRACTOGRAPHY OF SPECIMENS TESTED AT 650°C

Three fractured specimens, representative of the failure locations at 650°C, are shown in Fig. 33. With the exception of one test, 93-449, tested at a maximum stress of 475 MPa and $R=0.8$, the tests conducted at 650°C failed in the radius or transition zone, a region of stress concentration and reduced temperature.

A fatigue cracked region was observed on the fracture surface of the 650°C fatigue specimens. The fracture surfaces from specimens 92-602, and 92-606, tested at $R=0.1$ and maximum stresses of 400 MPa and 470 MPa, respectively, were examined with a scanning electron microscope (SEM). Matrix cracking indicating fatigue crack growth was observed in the [90] plies to extend toward the [0] plies. Evidence of through-thickness matrix cracking, Fig. 34, is shown from specimen 92-606. Matrix cracks extended to completely surround the [0] fibers as shown in Fig. 35. Fatigue cracking extended through-the-width of the specimen along the [90] fibers, Fig. 36, although through-thickness cracking was limited.

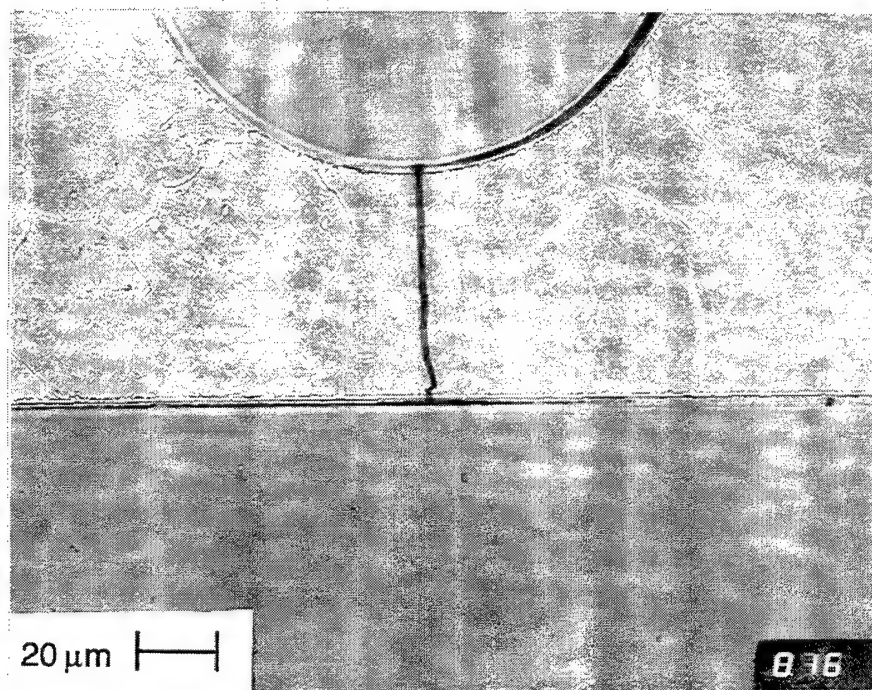


Fig. 31 Environmental damage of [0] degree fibers at 650°C

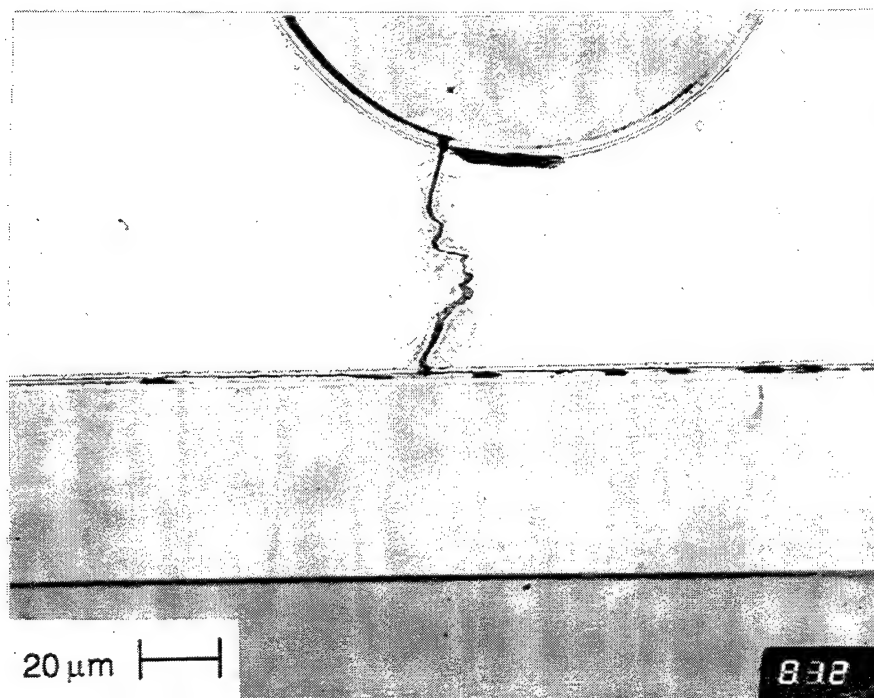


Fig. 32 Environmental damage of [0] degree fibers at 815°C

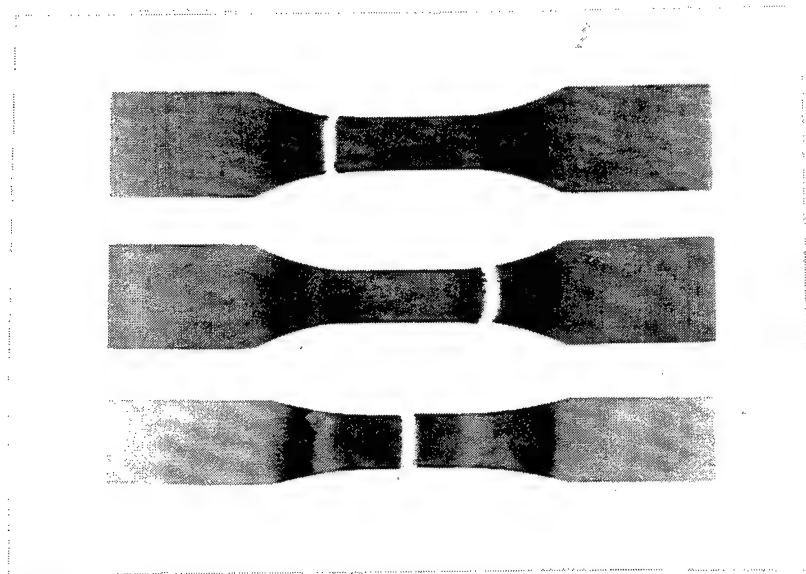


Fig. 33 Representative 650°C failure locations

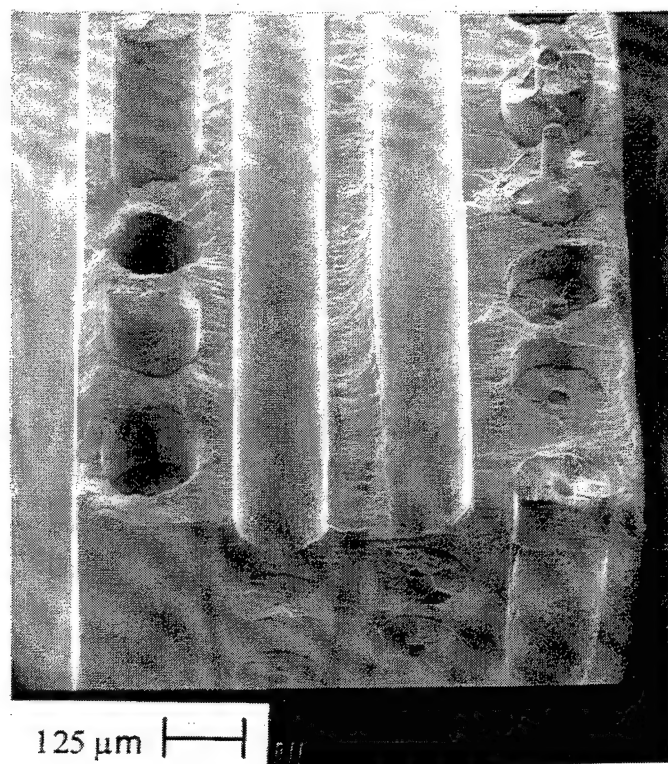


Fig. 34 Fatigue crack growth region of a 650°C test specimen

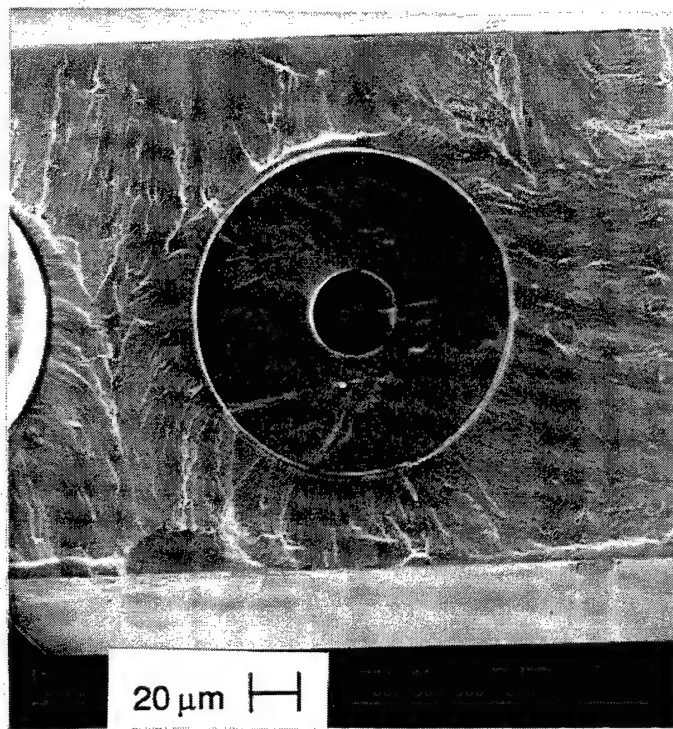


Fig. 35 Complete matrix cracking around a [0] fiber

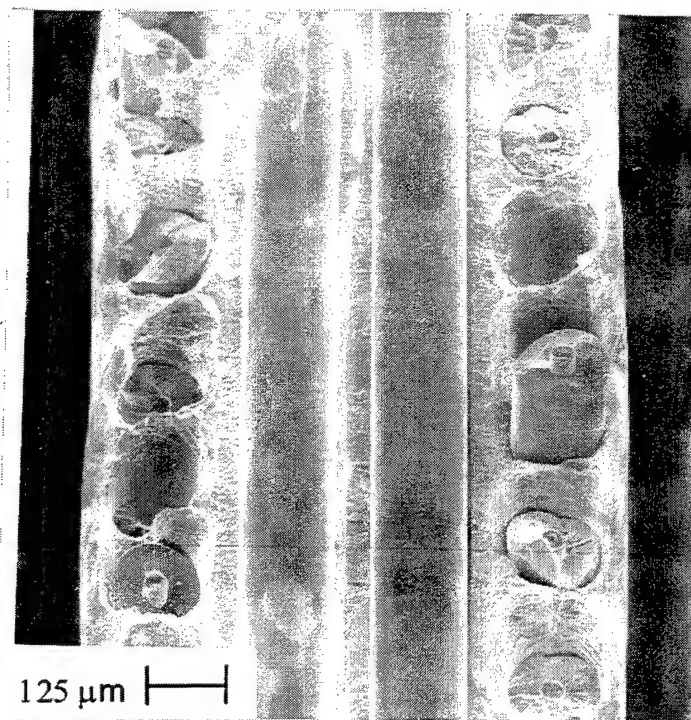


Fig. 36 Matrix fatigue cracks extending from the [90] plies

Matrix bounding the [0] fibers and nearest the surface is shown in Fig. 37 with extensive matrix ductility and dimpling, both around the uncracked portion surrounding the fiber, and at the specimen surface. Not all [90] plies were thoroughly cracked prior to failure as shown in Fig. 38, where the overload fast fracture region spanned the thickness of specimen 92-602. Ductile dimpling occurred between the [90] plies indicative of fast fracture as shown in Fig. 39.

The tests of the specimens 92-602 and 92-606, conducted at a stress ratio of 0.1 formed surface cracks in the radius region at both ends of the specimen, Fig. 40. An acoustic microscopy scan of the 92-602 radius region that did not fail was performed by P. Karpur of UDRI. From the scan, cracks reaching each edge of the specimen were noted, Fig. 41. The longest covered more than 50 % of the specimen width. Three cracks were detected, two reaching the specimen edge, and most notably one located in the center of the width with no edge connection. Longitudinal sectioning determined that all three of these cracks were through thickness cracks. The specimen surface was polished to reveal complete fiber bridging of the crack, and no fiber failure in the vicinity, Fig. 42. Very little fiber pullout was observed which suggests that, although fiber bridging of the crack may have occurred, fibers failed in the plane of the crack upon final fracture.

The extent of matrix fatigue cracking was influenced by the loading conditions. Specimens tested at similar maximum stresses, but increasing mean stresses at higher stress ratios, displayed a reduction in fatigue cracked matrix surface area. For example, specimen 92-602, tested with a maximum stress of 400 MPa, and a stress ratio of 0.1, lasted 130,000 cycles and failed after fatigue cracking covered approximately 73 % of the matrix fracture surface. Specimen 92-610, tested with a maximum stress of 450 MPa, and a stress ratio of 0.5,

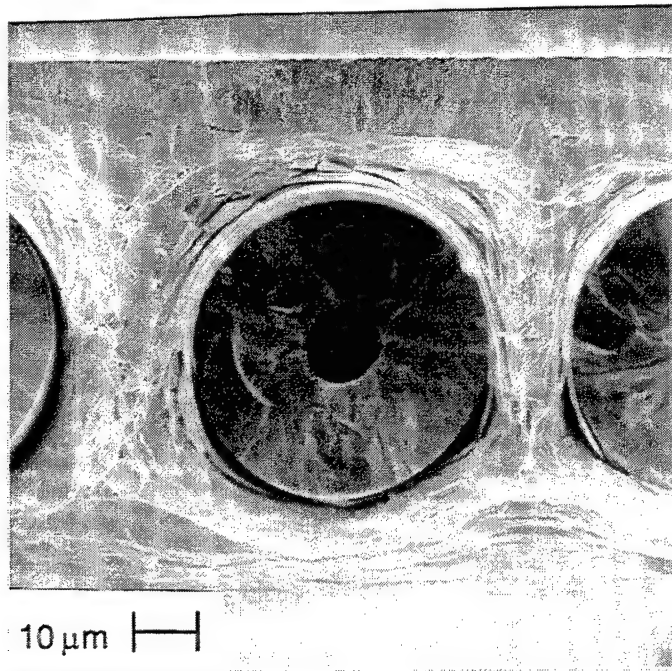


Fig. 37 Ductile overload matrix dimpling around a [0] fiber

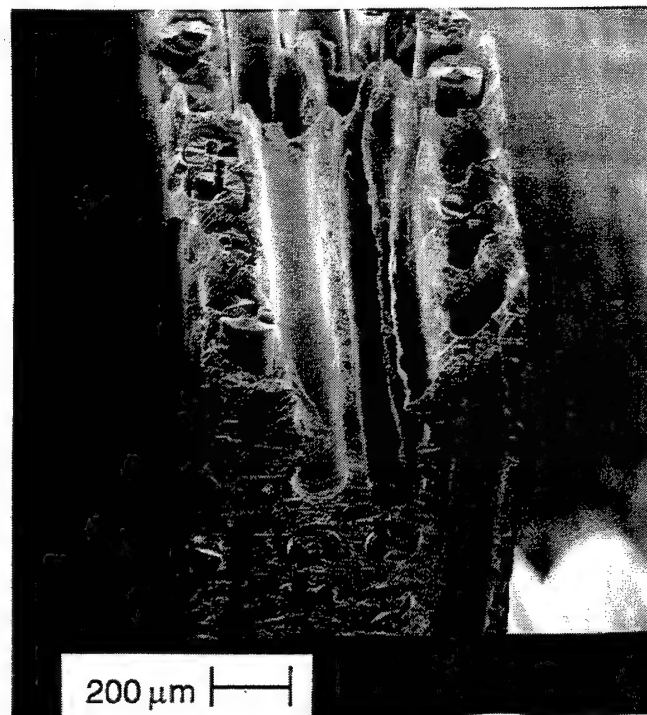


Fig. 38 Overload failure region of a 650°C test specimen with no cracks emanating from [90] fibers

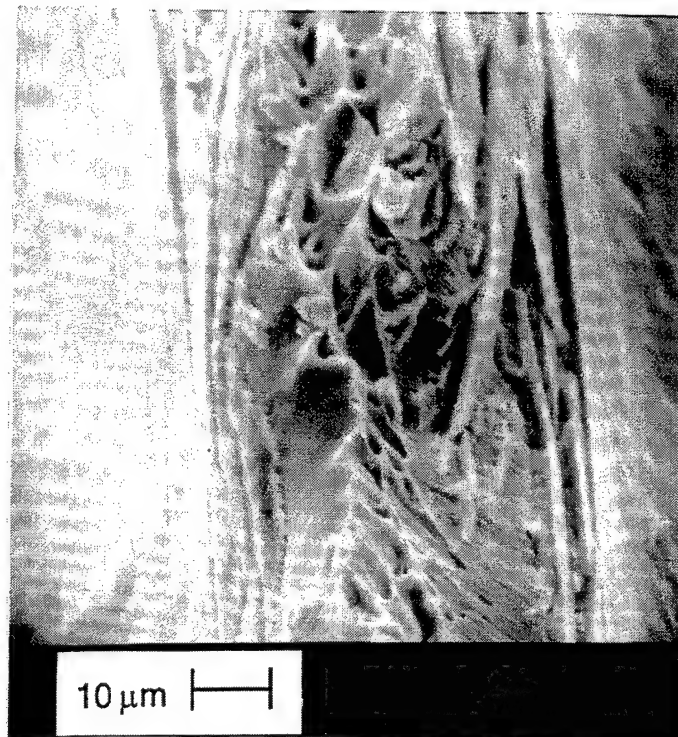


Fig. 39 High magnification photo of ductile dimpling between [90] plies on fracture surface

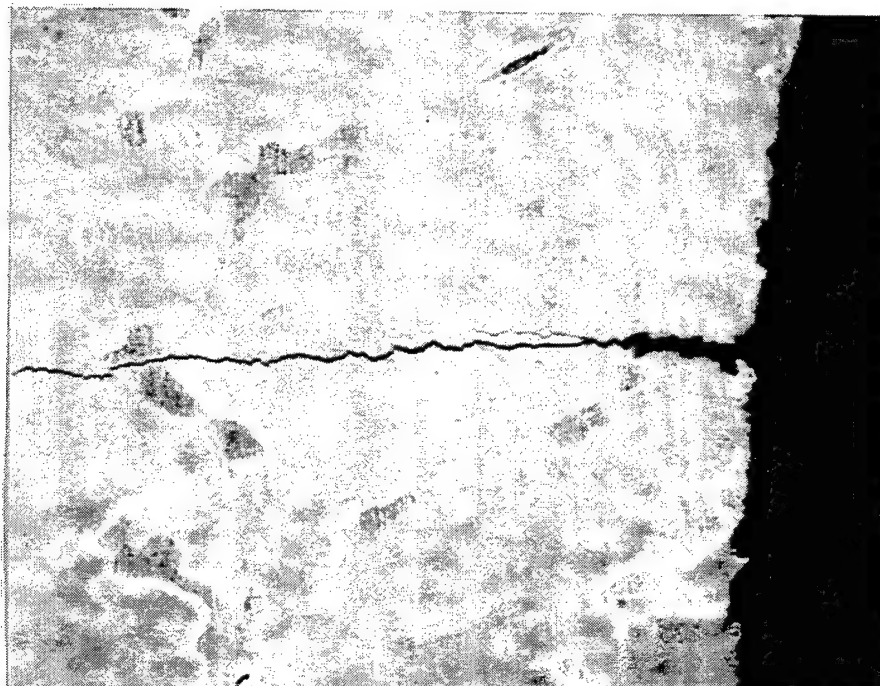


Fig. 40 Transgranular surface cracks in a specimen tested at 650°C

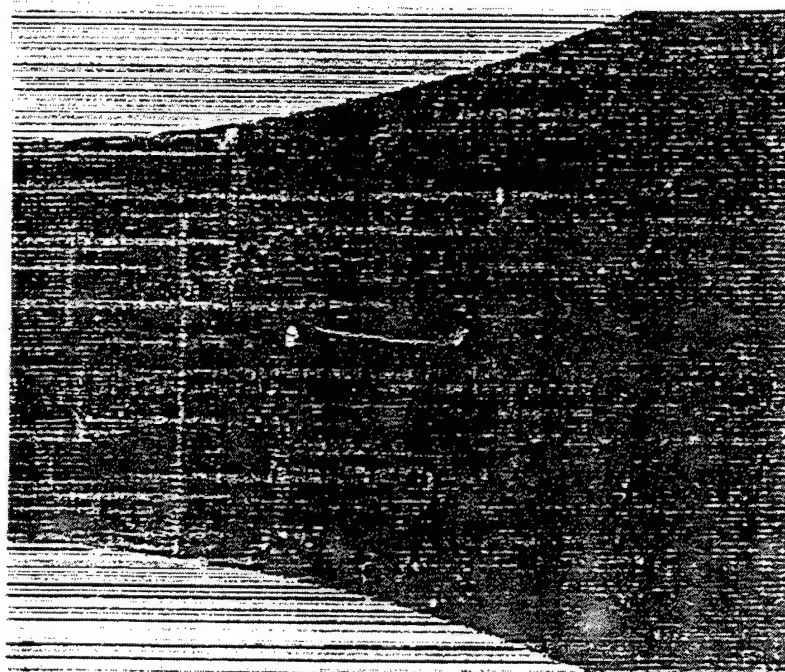


Fig. 41 Acoustic microscopy scan displaying edge and center cracks in a 650°C test specimen

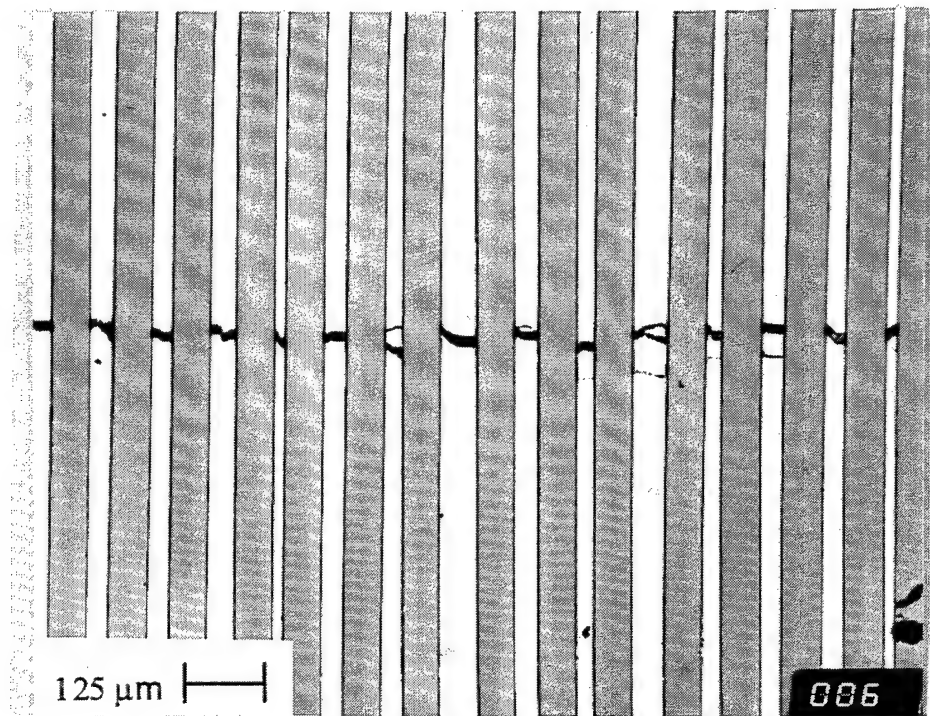


Fig. 42 Fiber bridging of through-thickness cracks

lasted 2.0275×10^5 cycles and failed after only 48 % of the matrix fracture surface was fatigue cracked. Furthermore, the specimen 93-449, tested at a maximum stress of 475 MPa and a stress ratio of 0.8, failed after 3.9965×10^7 cycles and resulted in a fracture very similar to the residual strength tensile test, 91-593, with matrix ductile overload failure but no matrix fatigue crack formation.

4.5 FRACTOGRAPHY OF SPECIMENS TESTED AT 815°C

All tests conducted at 815 °C resulted in gage section failures. Four of the fractured specimens are shown as a representative sample of failure location, Fig. 43. Fracture surfaces displayed a stepped surface suggesting a connection between cracks on different [90] fiber planes. Significant fiber pullout was also observed, and attributed to larger debond lengths due to extensive damage of the [0] fiber matrix interfaces at 815°C.

Fracture surfaces of the 815°C tests displayed crack propagation outward from the transverse fibers, similar to what was observed in the 650°C tests. Fractographic analysis of 92-605 tested with a stress ratio of 0.1, and a maximum stress of 400 MPa indicated that in the fatigue crack growth region, Fig. 44, cracks grew nearly to the surface as evidenced by the thumbnail crack between the [0] fibers in Fig. 45. A brittle failure zone was noted between the thumbnail crack and the specimen surface, Fig. 46. Alpha phase stabilized by oxygen diffused from the surface of the specimen created the brittle region. Strengthening occurred in Timetal®21S when oxygen levels increase; however, a simultaneous reduction in ductility was noted [16, 17]. The surface of the specimen tested at 815°C failed in a brittle manner, indicating the embrittling effect of the alpha phase surface precipitation. Stepped fracture and fiber pullout, Fig. 47, suggested an increase in damage at 815°C along the [0] fibers between [90] fiber planes.

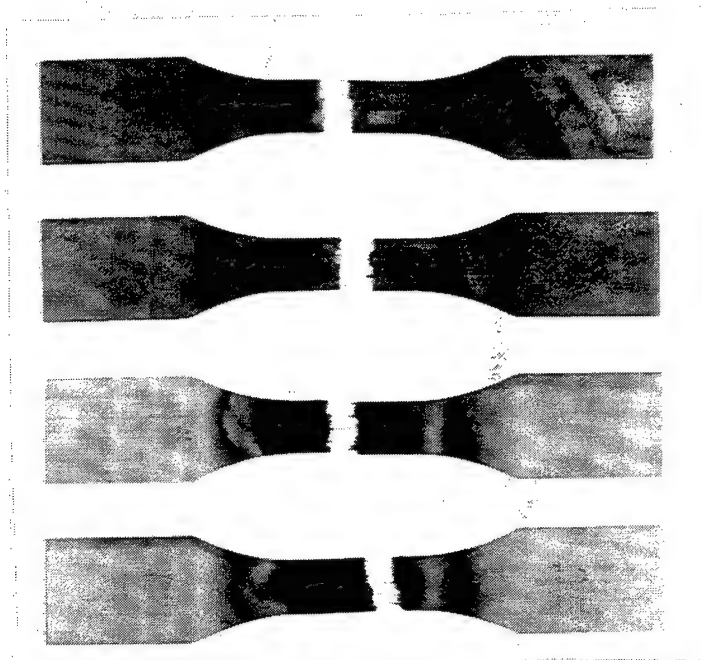


Fig 43 Representative 815°C failure locations

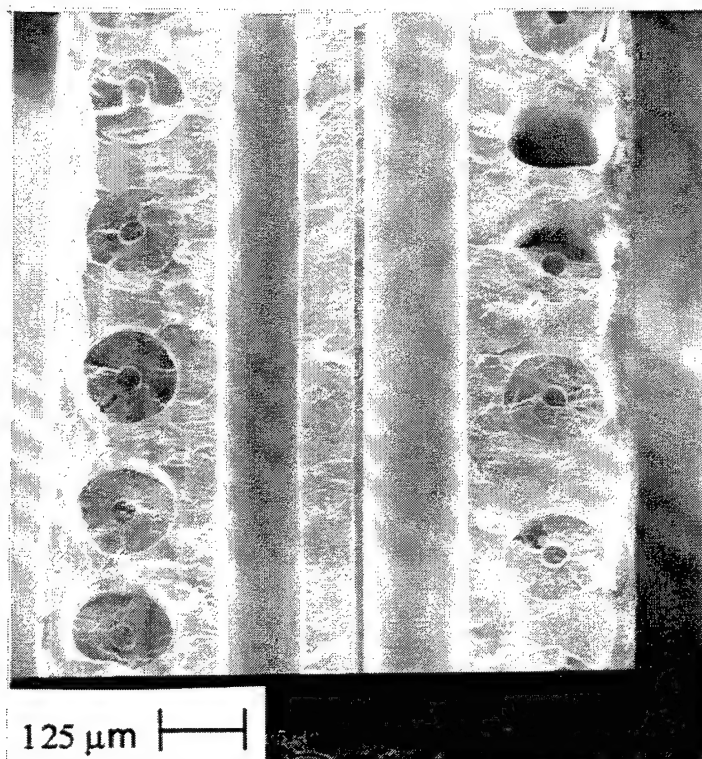


Fig. 44 Matrix fatigue cracks extending from the [90] plies

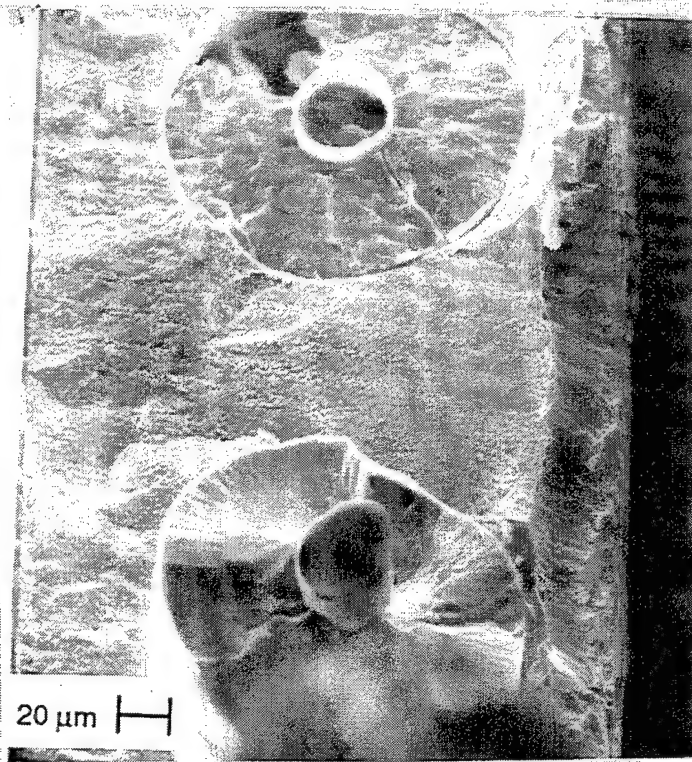


Fig. 45 Thumbnail crack on 815°C fracture surface

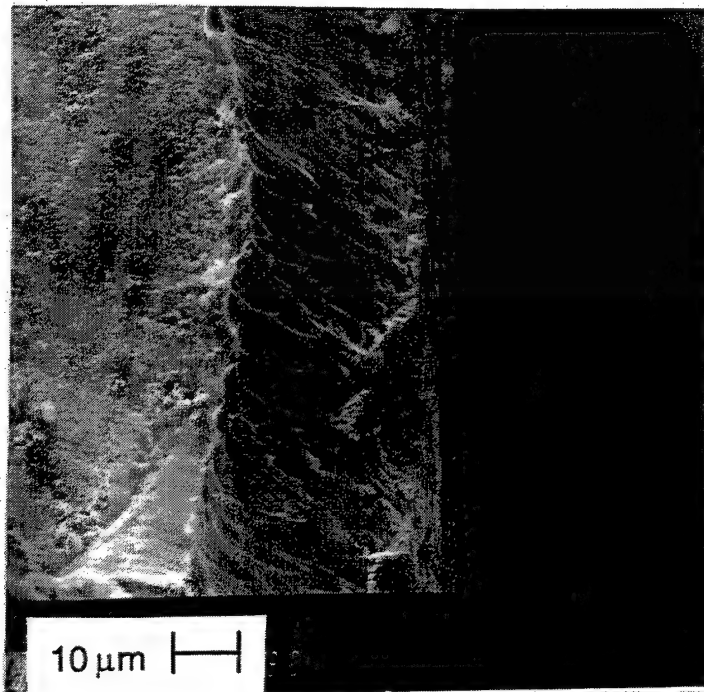


Fig. 46 Brittle failure region induced by precipitated alpha phase

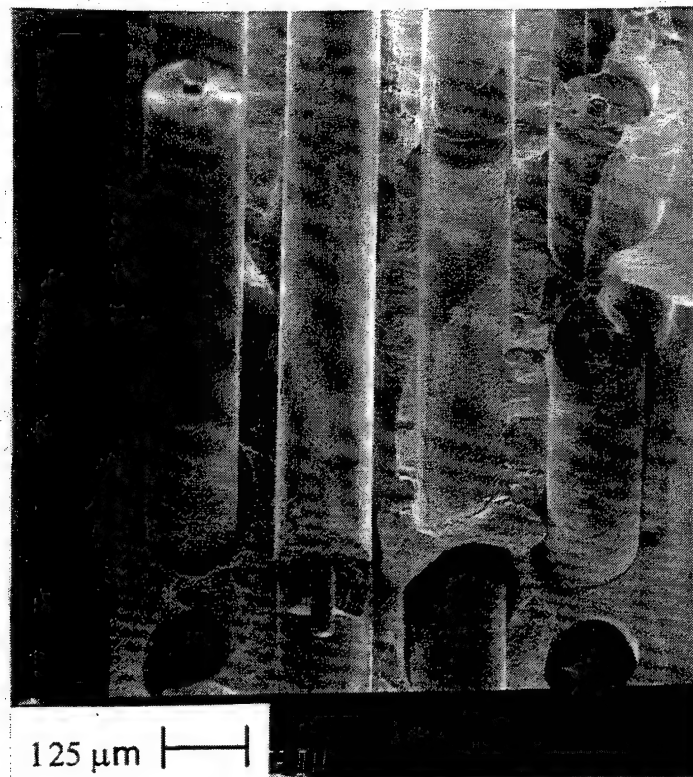


Fig. 47 Stepped fracture in overload failure region of an 815°C test specimen

SECTION 5

DAMAGE MONITORING

5.1 ELECTRIC POTENTIAL RESULTS

Direct current electric potential (DCEP) voltage difference was monitored for selected high-frequency fatigue tests. The current density is assumed to be uniformly distributed throughout the matrix cross-sectional area of the specimen. The superalloy gripping surfaces, to which the DCEP current leads were spotwelded, encourage the uniform distribution of electric current across the specimen width. DCEP pickup leads, however, were spotwelded directly to the specimen with a 50.8 mm spacing. The measured voltage drop, V , along the specimen, between the DCEP pickup leads, is a function of the applied current and conducting material resistance, from the relation:

$$V = I \cdot R \quad (5.1)$$

where I is the current which was set at 10 A and R is the resistance of the specimen between the pick up leads. Therefore, it can be concluded that a change in the conducting material resistance creates a corresponding change in measured voltage.

The resistance of the specimen is related to material resistivity and geometry by the relation

$$R = \rho L / A \quad (5.2)$$

where ρ is the resistivity, L is the pickup lead spacing which was experimentally set at 50.8 mm, and A is the specimen cross-sectional area. The composite constituent resistivities, Table 8, indicated that the fiber resistivity was six orders of magnitude greater than the matrix resistivity [11, 21]. Fiber resistivity was assumed to have negligible change with increasing temperature. Therefore, the matrix was the primary current path, due to its lower resistance.

Table 8

CONSTITUENT RESISTIVITIES AS A FUNCTION OF TEMPERATURE

Material	Temperature (°C)	Resistivity ($\Omega \cdot cm$)
SCS-6	23.9 - 815	200
Timetal®21S	23.9	135.00E-6
Timetal®21S	650	148.04E-6
Timetal®21S	815	148.40E-6

If the cross-sectional area is reduced by fatigue damage such as matrix cracking, the material resistance will increase from equation (5.2). Furthermore, a subsequent increase in measured voltage will result as shown by equation (5.1).

For reference purposes, DCEP voltage drop was monitored at elevated temperature conditions of 650°C and no mechanical loading for 20 hours. A transformation from time of exposure to equivalent cycles enabled the thermal exposure specimens to be compared to the results of the 650°C fatigue results.

Measured DCEP voltage results for 650°C tests are plotted with respect to fatigue cycles in Figs. 48-50, and 815°C tests are shown in Figures 51-53. Each plot summarizes the fatigue tests at one stress ratio, and thermal exposure tests

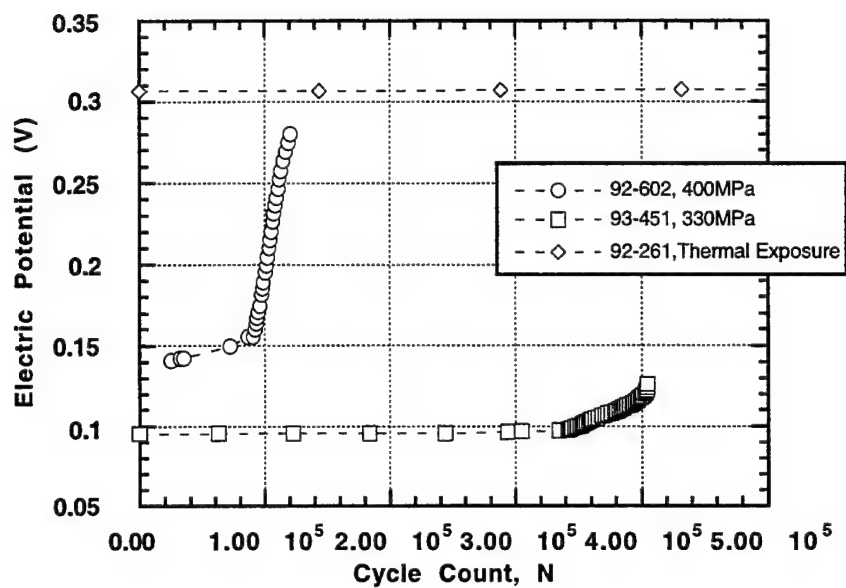


Fig. 48 DCEP for 650°C, R=0.1 tests

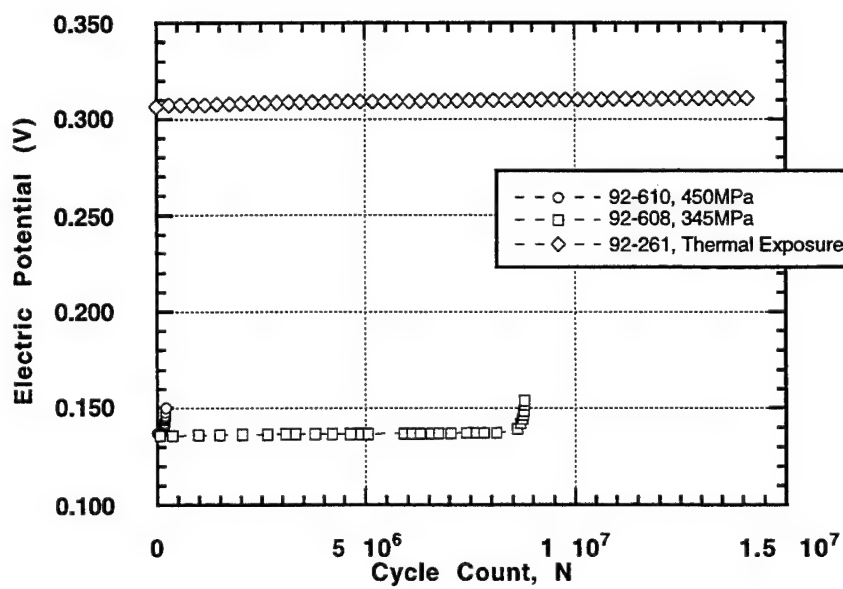


Fig. 49 DCEP for 650°C, R=0.5 tests

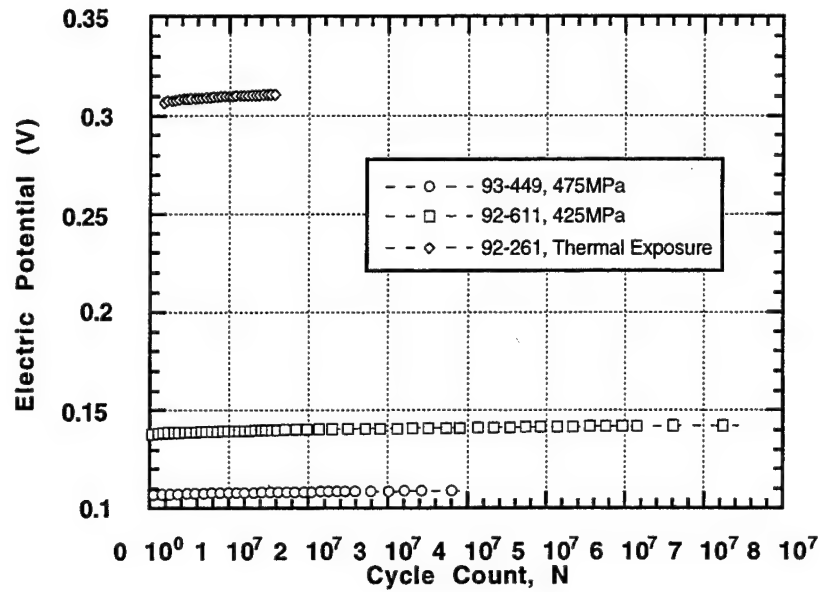


Fig. 50 DCEP for 650°C, R=0.8 tests

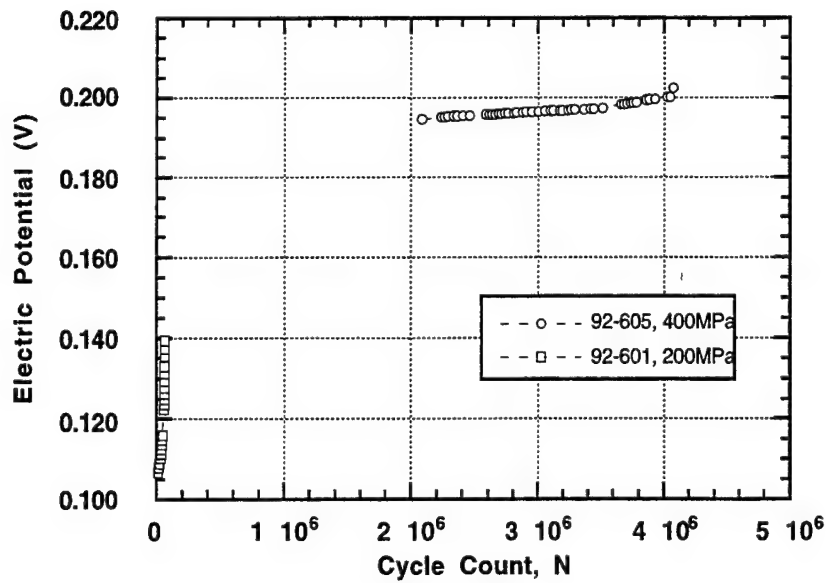


Fig. 51 DCEP for 815°C, R=0.1 tests

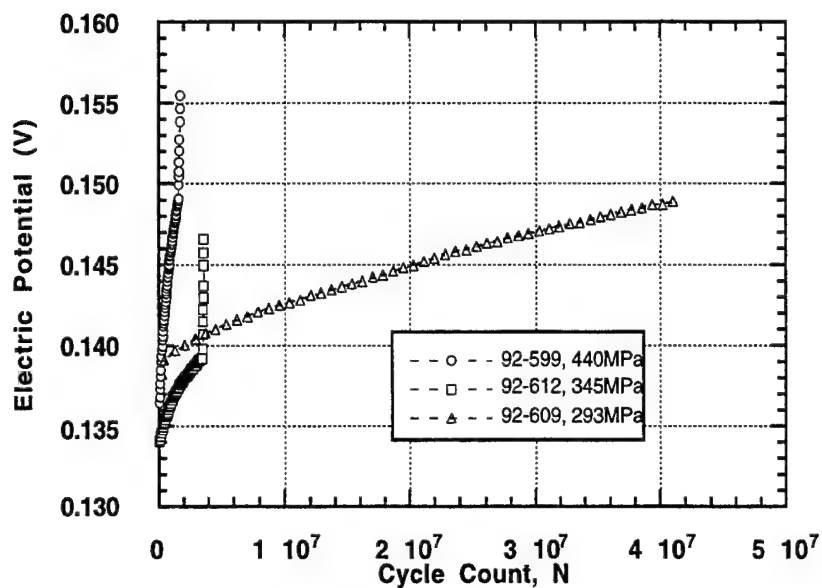


Fig. 52 DCEP for 815°C, R=0.5 tests

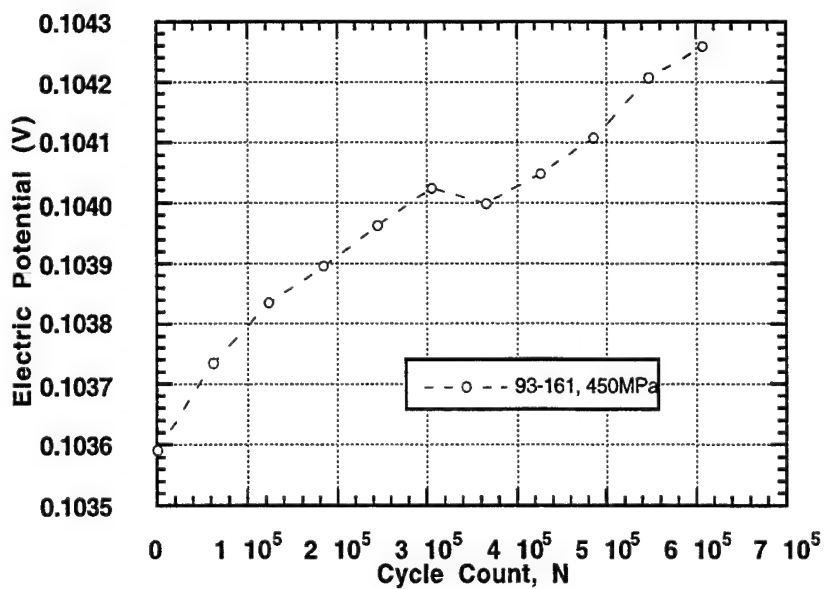


Fig. 53 DCEP for 815°C, R=0.8

tests were included at 650°C. Figures 48-53 incorporate data from three specimen geometries and two different volume fractions, contributing to the overall initial DCEP voltage variation. The variations can be attributed to discrepancies in DCEP pickup lead spacing, specimen geometry, and material volume fraction.

The initial electric potential voltage drop was calculated with a knowledge of the DCEP conditions. The voltage drop relation, a function of DCEP parameters, material properties, and specimen geometry, has the form

$$V = \frac{I\rho L}{A_m} \quad (5.3)$$

where A_m is the specimen cross-sectional area. The very high resistivity of the SCS-6 fiber relative to the matrix material suggested that it carried little electrical current, and therefore, the fibers were assumed to behave as insulators. The electrical current carrying cross-sectional area of the specimen was approximated after examining the matrix and fiber relationship. The presence of longitudinal and cross-ply fibers complicated the analysis. The [0] fibers and matrix in the outer laminate plies act as resistors in parallel. Since the fibers were assumed to act as insulators, the conducting area of the [0] plies was exclusively the matrix material. The electric current conducting matrix area of the two plies containing [0] fibers was determined with the relation

$$A_m[0] = 2Wt'(1 - V_f) \quad (5.4)$$

where W = specimen width (mm), t' = laminae thickness (mm) and V_f = fiber volume fraction. The laminae containing [90] fibers resulted in the fibers and

matrix behaving as resistors in series. However, the fibers act as insulators and disrupt the current path in the laminae containing off-axis fibers. By assuming that no current is carried in the wake of the fiber, as shown in Fig. 54, the portion of matrix which acts as a current path in the two [90] plies was reduced to the relation,

$$A_m[90] = 2W \left(t' - 2\sqrt{\frac{V_f t'}{n_f \pi}} \right) \quad (5.5)$$

where n_f = number of fibers/mm = 5.079.

A relation to calculate the voltage drop across the DCEP pick-up leads was formed by summing the current carrying cross-sectional area, (5.4), (5.5), and substituting into (5.3). The initial electric potential voltage difference has the form

$$V = \frac{\rho IL}{2W \left[t'(2 - V_f) - 2\sqrt{\frac{V_f t'}{n_f \pi}} \right]} \quad (5.6)$$

and resistivity was assumed to be uniform in the region spanned by the electric potential pickup leads.

Predicted initial voltages are shown with their corresponding experimentally measured values in Table 9 for tests conducted with differing specimen geometries and test conditions.

Matrix material between [90] fibers assumed to carry no electrical current.

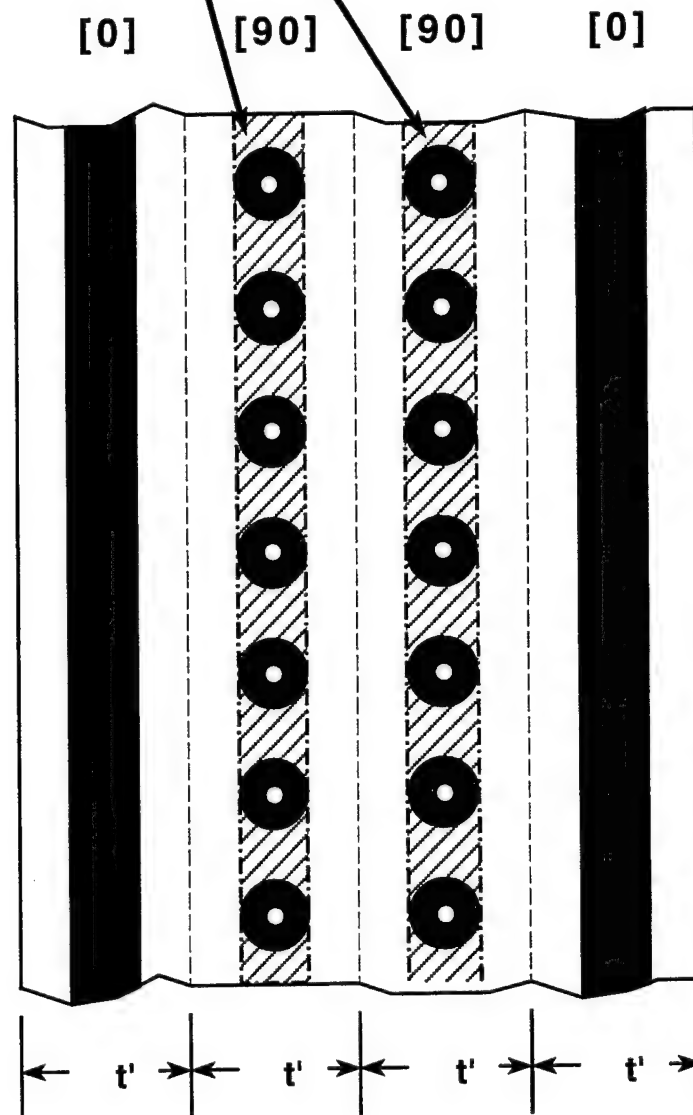


Fig. 54 Reduction in current carrying cross-sectional area due to [90] fibers

Table 9

PREDICTED AND MEASURED INITIAL DCEP VOLTAGE DROP

Spec. ID	Temp. °C	Width	Thickness	V (Predicted)	V (Measured)
92-261	650	6.10 mm	0.83 mm	0.3207	0.3063
92-602	650	12.78 mm	0.80 mm	0.1660	0.1554
92-612	815	12.70 mm	0.81 mm	0.1625	0.1341

The predicted initial readings at 650°C are within 6 % of the experimentally recorded values, however, at the higher temperature of 815°C, the prediction differs from the experimental value by greater than 20 %. These discrepancies were the result of experimental variations such as pickup lead spacing. Voltage drop values were also subject to varying material resistivities outside of the heated zone. As noted in Table 8, resistivity is temperature dependent, therefore, the resistivity decreases in the regions outside of the heated zone where temperature is reduced, and spanned by the DCEP pickup leads. The assumption of uniform test temperature and subsequently uniform resistivity, over-estimated the initial electric potential voltage drop.

The overall trends in the DCEP results become apparent when data sets are normalized relative to their initial values, and plotted as percent DCEP change from the initial voltage measurement. The 650°C results are shown in Figs. 55-57. In Figure 55, a maximum increase of 98% is shown for HF test specimen 92-602, while Kortyna [6] noted maximum increases on the order of

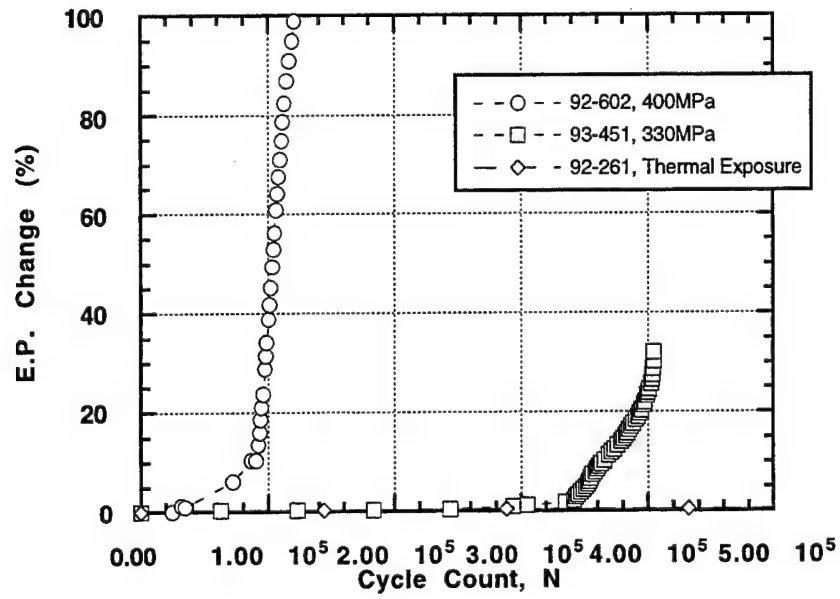


Fig. 55 Normalized DCEP change for 650°C, R=0.1

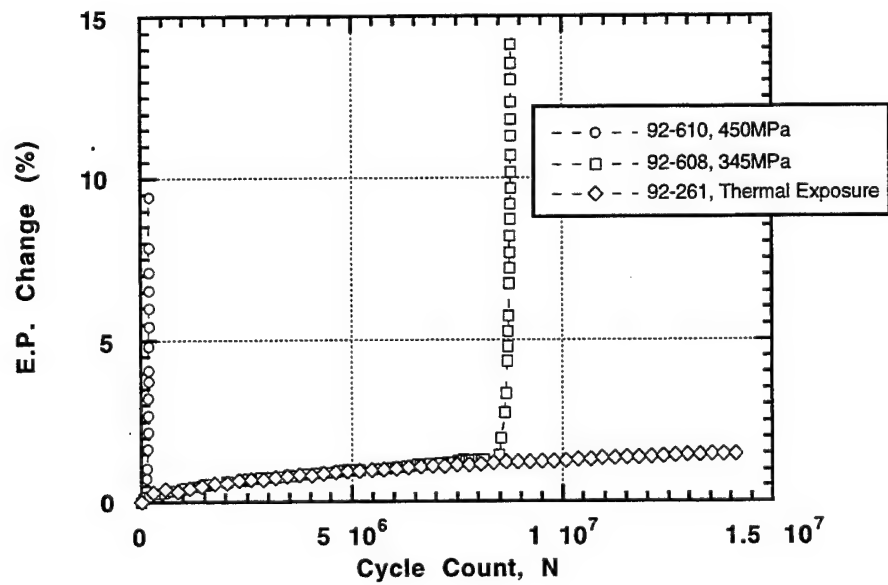


Fig. 56 Normalized DCEP change for 650°C, R=0.5

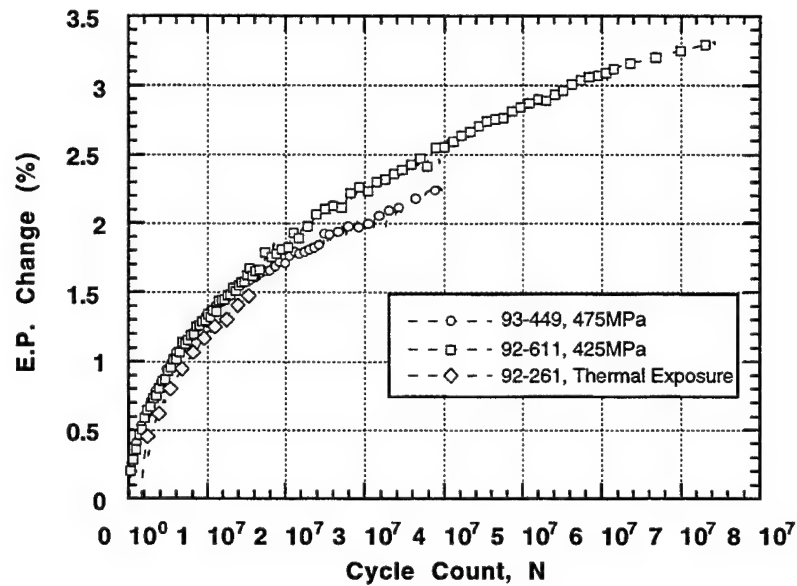


Fig. 57 Normalized DCEP change for 650°C, $R=0.8$

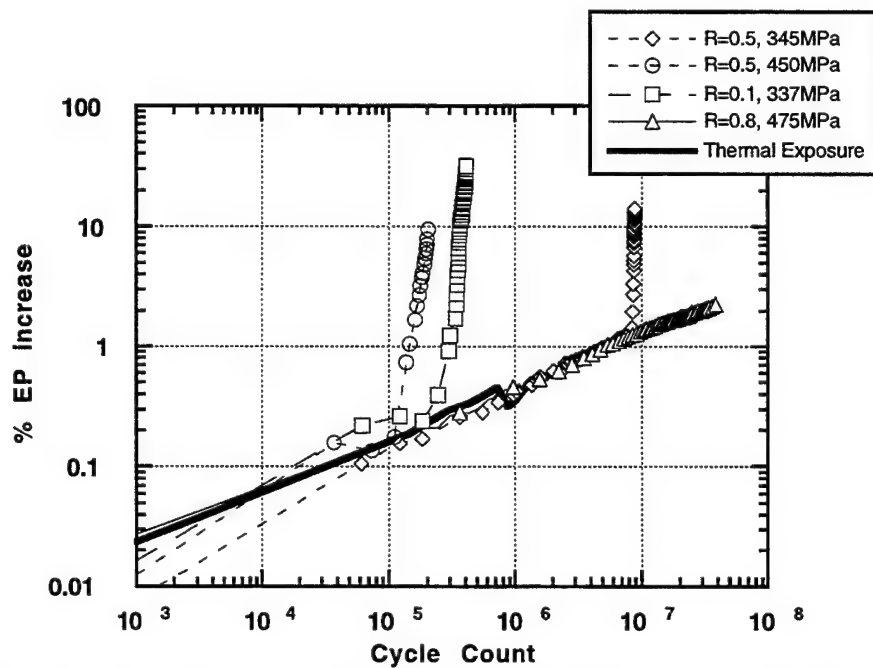


Fig. 58 Consolidation of normalized DCEP change for 650°C, $R=0.1, 0.5$ and 0.8

only 10% for unidirectional SCS-6/Ti-24Al-11Nb tested at 815°C. The greater increase in DCEP for the cross-ply composite tested in this study was attributed to greater damage to the cross-sectional area and interruption of the current path due to substantial matrix cracking caused by the 90° fibers.

The inclusion of the thermal exposure test 92-261 with the 650°C results, Figs. 55-57, indicates that DCEP data coalesces through the intermediate stages of life for various test conditions. The thermal exposure tests indicate that even in the absence of mechanical loading, DCEP voltage increases 1.5 % in 20 hours. All 650°C percent DCEP change results are shown in Figure 58 to collapse into a single line regardless of stress ratio, maximum stress, and mechanical loading. This suggests that DCEP voltage did not change with the formation of matrix cracks from the [90] fibers, but rather only from extensive through-thickness matrix cracking present near the end of the fatigue life of the specimen.

DCEP results at 815°C are shown in Figs. 59-61 and although the voltage increases throughout fatigue life, the results at different conditions do not coalesce as noted at 650°C.

To better study the change in DCEP throughout the fatigue lives, results were plotted as percent DCEP change vs. life fraction (%) as shown in Figs. 62-67. Tests conducted at both 650°C and 815°C display similar DCEP trends. At a stress-ratio of $R=0.1$, the electric potential increases rapidly between 70 and 90% of life. As shown in Fig. 62 and 65, tests conducted at 400 MPa and 320 MPa began increasing sharply at 70 and 80 % of life, respectively, suggesting that the onset of rapid damage accumulation relative to the life fraction consumed was directly influenced by the magnitude of the maximum stress. The substantial

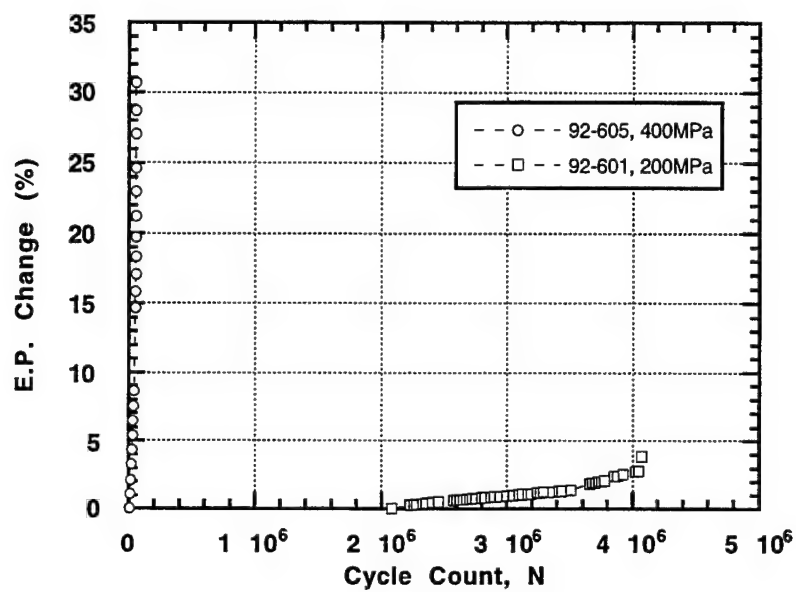


Fig. 59 Normalized DCEP change for 815°C, R=0.1

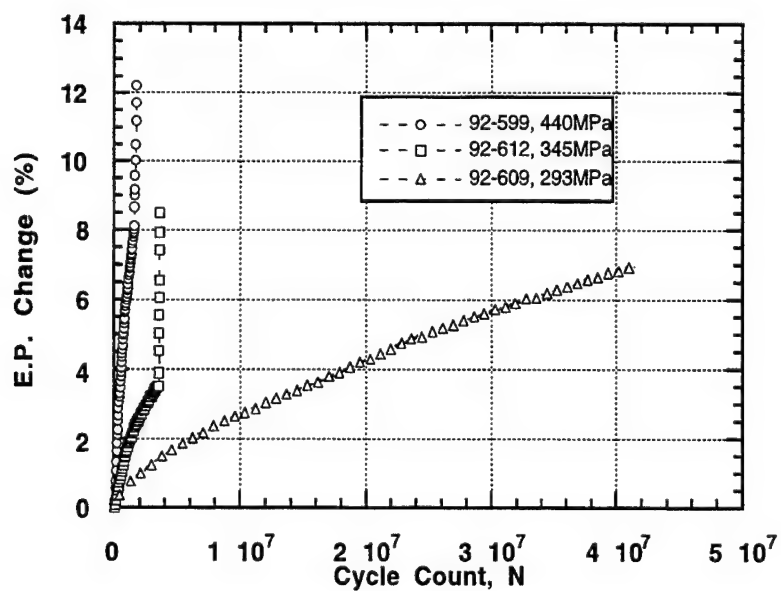


Fig. 60 Normalized DCEP change for 815°C, R=0.5

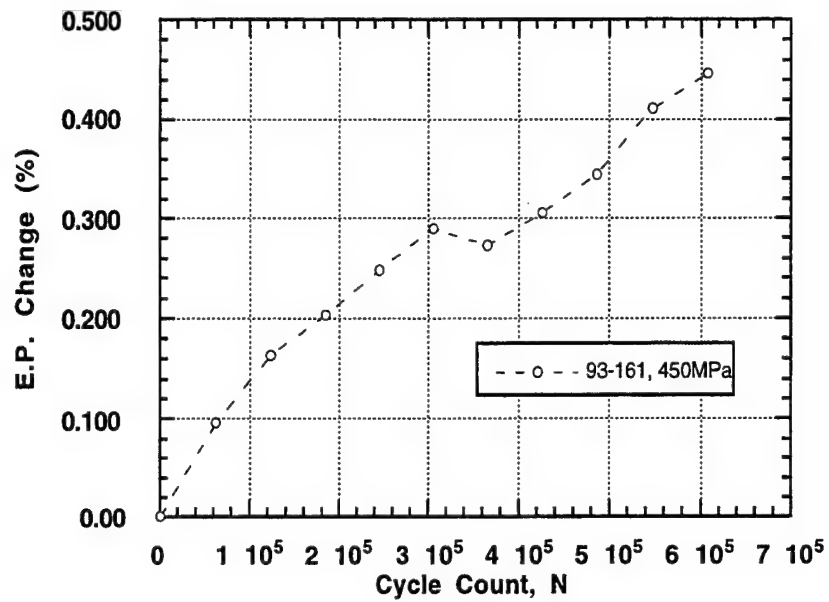


Fig. 61 Normalized DCEP change for 815°C, R=0.8

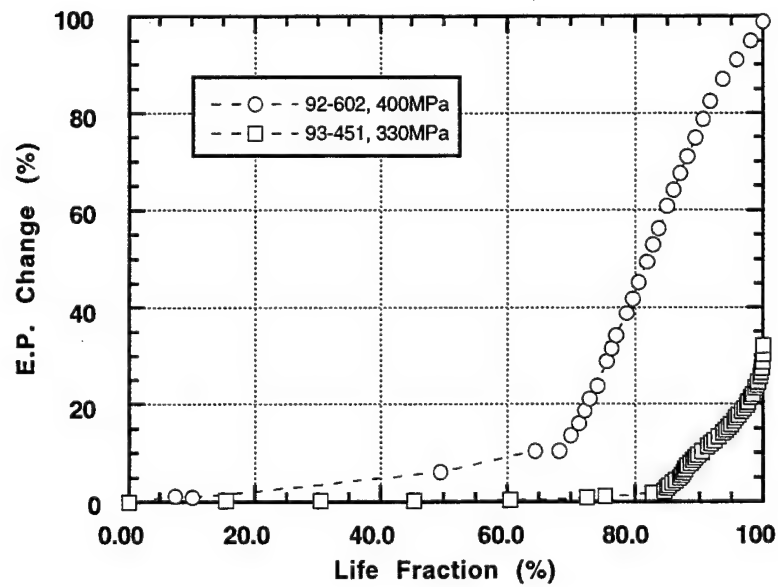


Fig. 62 DCEP change with respect to life for 650°C, R=0.1

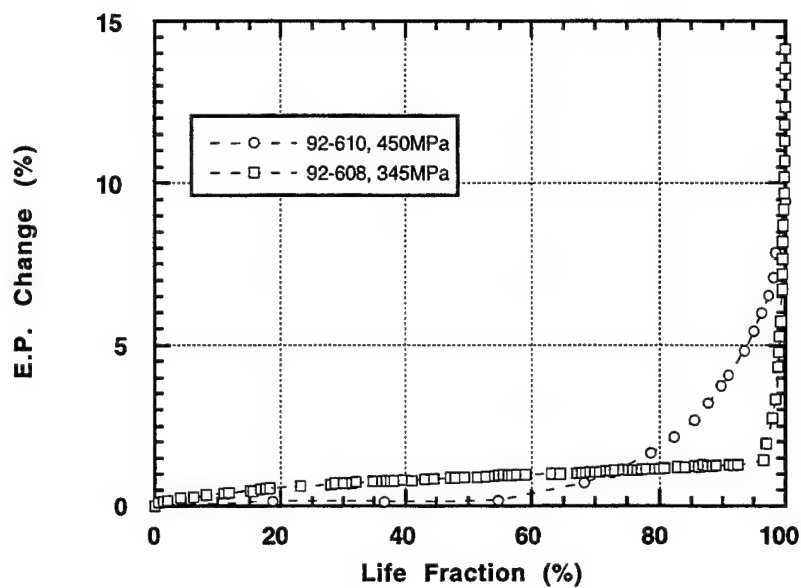


Fig. 63 DCEP change with respect to life for 650°C, R=0.5

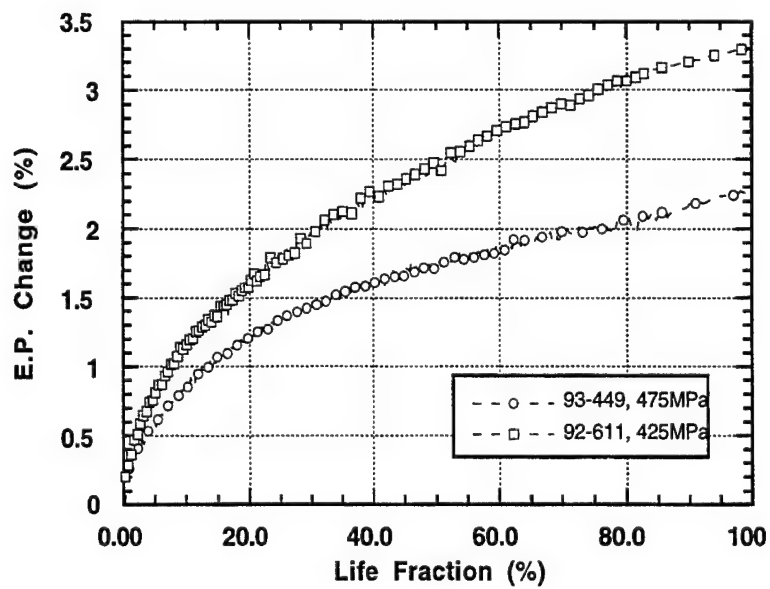


Fig. 64 DCEP change with respect to life for 650 °C, R=0.8

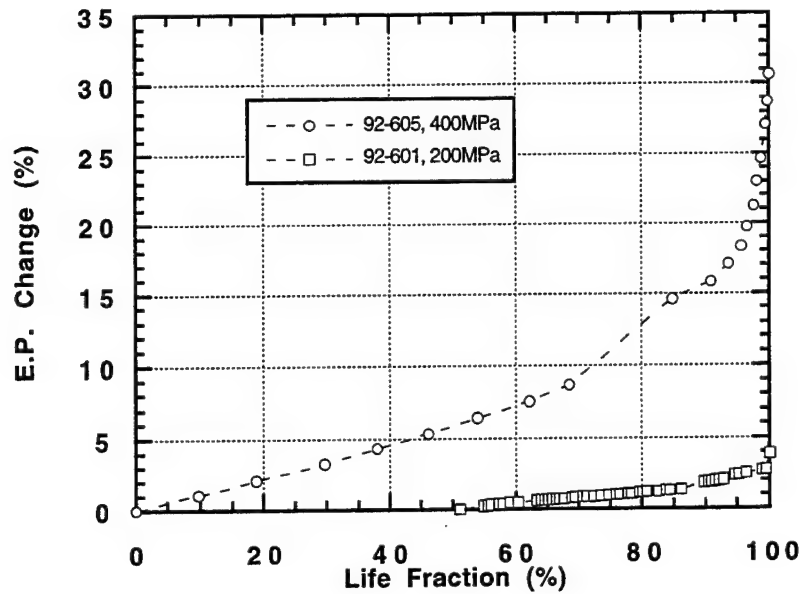


Fig. 65 DCEP change with respect to life for 815°C, R=0.1

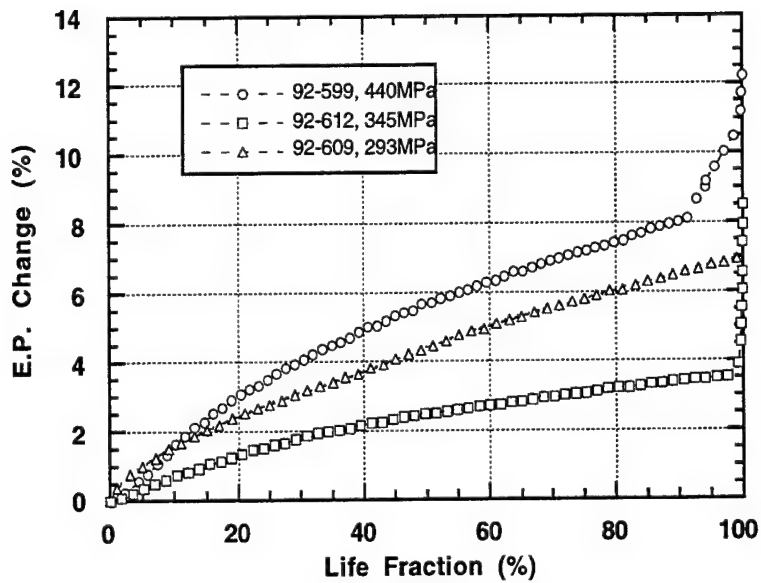


Fig. 66 DCEP change with respect to life for 815°C, R=0.5

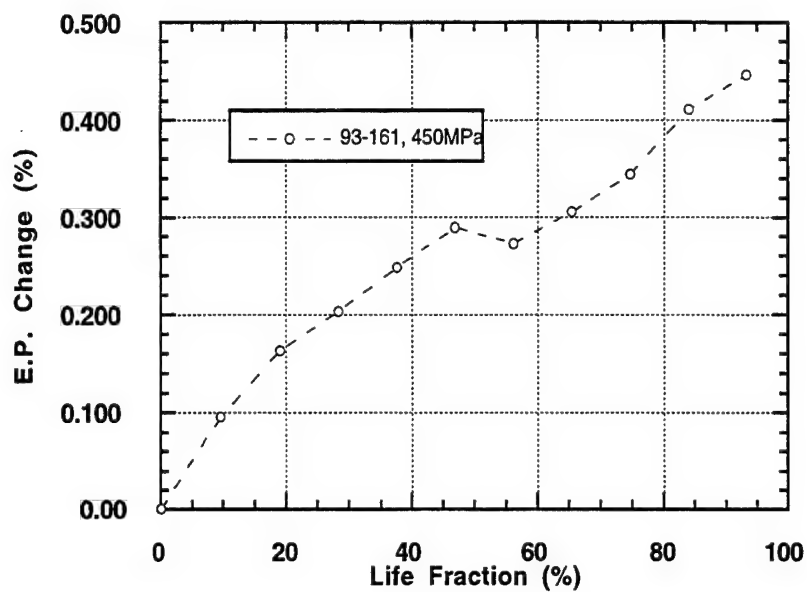


Fig. 67 DCEP change with respect to life for 815°C, R=0.8

increase in DCEP was attributed to matrix cracking in the radiused transition region of the specimen. Although no correlation between matrix crack lengths and measured electric potential voltage was determined.

At a stress ratio of 0.5, Figs. 63 and 66, the failure was more abrupt with the onset of DCEP increase occurring after 90 % of the life. Furthermore, while the prior two stress ratios, 0.1 and 0.5, record a rapid increase in DCEP voltage when failure is imminent or occurring, the $R=0.8$ data, Figs. 64 and 67, show no sign of increase.

5.2 CORRELATION OF DCEP INCREASE WITH PHYSICAL OBSERVATIONS

Direct correlations of DCEP results with damage mechanisms and damage accumulation were not determined; however, general observations related to the effectiveness of DCEP for detecting fatigue damage were made. DCEP voltage was not effected by the failure of SCS-6 fibers since they behave as insulators and carry no current. However, matrix cracking will reduce the cross-sectional area and should result in an increase in voltage. To quantify the effect of matrix damage on DCEP results, the effect of area reduction on measured voltage can be studied. As noted in the physical observations section, through-thickness cracking occurs in a limited region of the specimen length. From equation (5.6), it was determined that a reduction in cross-sectional area of 50 % over a length of 5.08 mm with a pick-up lead spacing of 50.8 mm results in a predicted voltage increase of only 10%. The lack of increase indicates that DCEP is insensitive to damage because of the influence of the undamaged portion of matrix material. The substantial undamaged matrix material due to the long pickup lead spacing, acting in series with the damaged material, dominates the DCEP response. The requirement of the presence of large scale matrix cracking to be recognizable in the experimental potential drop measurements better explains the similarities in

the thermal exposure and fatigue test DCEP. Substantial cracking resulting in a large reduction in cross-sectional area was necessary to change the measured voltage drop. The magnitude of the voltage drop increase was effected by the applied mean stress. Tests having high mean stresses, particularly at $R=0.8$, resulted in the rapid overload failure of the specimen before sufficient fatigue crack growth reduced the matrix area, and subsequent voltage drop increases could occur.

Matrix cracking which was shown to initiate at the $[90]$ fibers does not reduce the current carrying cross-section sufficiently to create a detectable voltage change and may be obscured by the presence of transverse fibers. Therefore, matrix cracking which occurs in the $[90]$ laminae early in life does not result in a noticeable change in DCEP.

SECTION 6

LIFE PREDICTION

6.1 LINEAR SUMMATION MODEL

As noted in the results section, fatigue life displays a cyclic dependence at 650°C, and a mixed mode of both cycle and time dependence at 815°C. Fatigue lives vary with frequency, stress range, and stress ratio. A model developed by T. Nicholas of the Air Force Materials Directorate for the unidirectionally reinforced SCS-6/Ti-24Al-11Nb composite [22, 23] was adapted to the cross-ply laminate of interest in this study. The life prediction model, a phenomenological linear-summation model, was developed to predict the fatigue life as a function of frequency, stress range, and stress ratio, based on life fractions under fatigue and creep.

The total fatigue life, N , was divided into three components: a cyclic stress term N_c ; time-dependent environmental degradation term, N_t ; and a mixed-mode term, N_i . The linear life fraction model used in this study has the form:

$$\frac{1}{N_c} + \frac{1}{N_t} + \frac{1}{N_i} = \frac{1}{N} \quad (6.1)$$

The life associated with the cyclic stress term has the form:

$$N_c = A(\Delta\sigma)^{-m} \quad (6.2)$$

where the coefficient A and exponent m were determined by a method of least squares fit on a log-log plot. To determine A and m , cycles to failure obtained at the highest frequency were used since the data were least influenced by time-dependent effects. The variables A and m for 650°C and 815°C were determined from the data in Figures 68 and 69, respectively. For the 650°C data, A equaled 1.755E+27 and m equaled -8.7132, and for the 815°C data A equaled 1.0941E+20 and m equaled -5.9041.

The life expended per cycle by time-dependent degradation, $1/N_t$, is evaluated through the summation of damage over an entire cycle with respect to time at stress. The time to failure as a function of stress is represented by the creep rupture time to failure and has the form:

$$t_c = B\sigma^{-n} \quad (6.3)$$

The summation of the incremental time at stress was performed by simplifying the waveform to be triangular and integrating over one cycle or period. The stress increment is related to the time increment by:

$$dt = \frac{d\sigma}{2f(1-R)\sigma_{\max}} \quad (6.4)$$

where f is the frequency and R is the stress ratio. Integrating this equation with respect to the cyclic stress range to determine the time at stress and summing the creep damage, results in the time dependent life fraction per cycle which has the form:

$$\frac{1}{N_t} = \frac{1}{f\sigma_{\max}(1-R)} \int_{R\sigma_{\max}}^{\sigma_{\max}} \frac{d\sigma}{t_c(\sigma)} \quad (6.5)$$

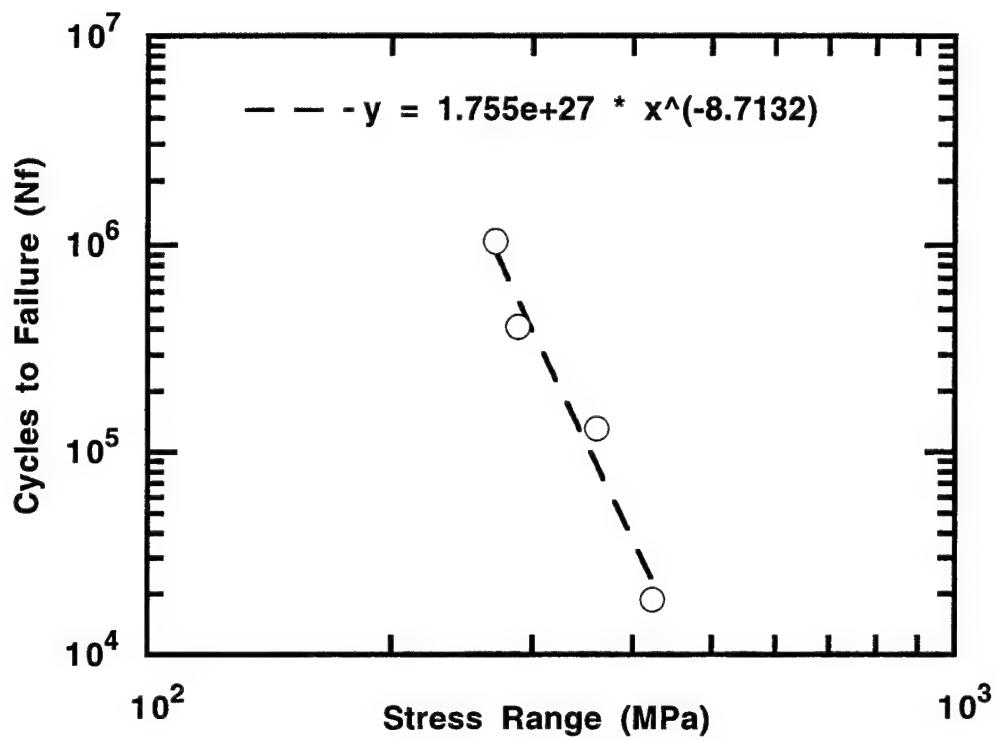


Fig. 68 Cyclic damage term, 200 Hz power law fit, R=0.1, 650°C

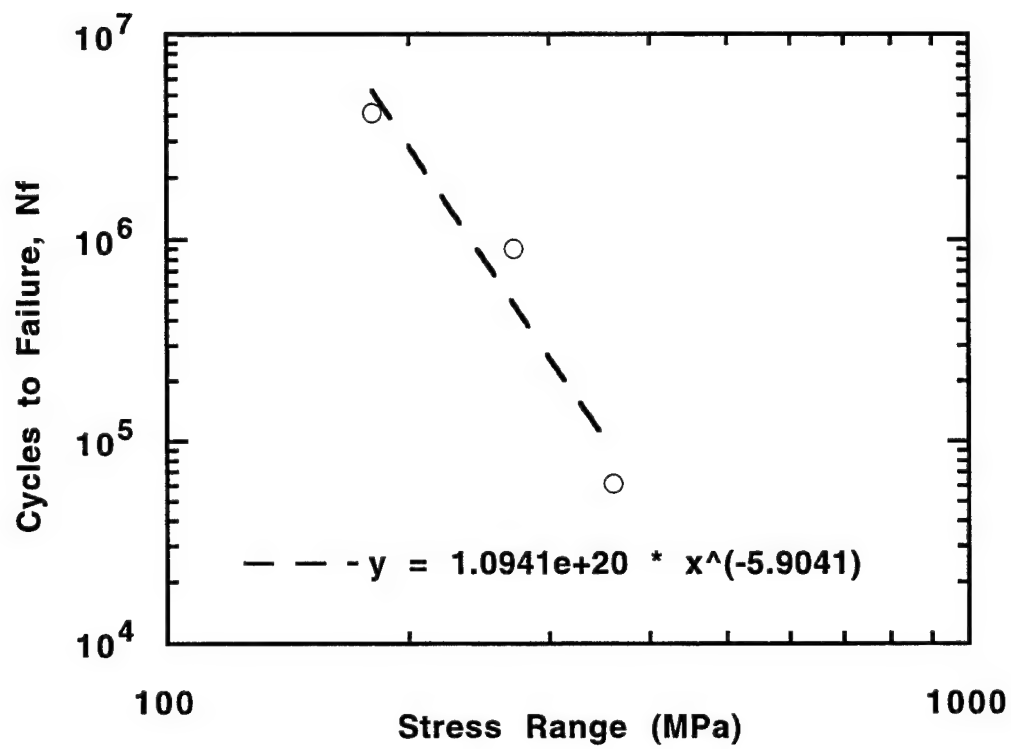


Fig. 69 Cyclic damage term 200 Hz power law fit, R=0.1, 815°C

Performing the integration of this equation and inverting the results provides the number of cycles to failure due solely to time dependent effects and has the form:

$$N_t = \frac{Bf(n+1)(1-R)}{\sigma_{\max}^n (1-R^{n+1})} \quad (6.6)$$

Investigations by Russ and Nicholas [22] indicated that life predictions using only cyclic and time dependent life fractions grossly overestimated fatigue lives necessitating an interaction term. The interaction term, N_i , the fatigue life associated with interaction effects, is represented by:

$$N_i = C\sqrt{N_{ii}N_{ci}} \quad (6.7)$$

The interaction term accounts for enhanced damage due to the combined effects of creep and fatigue. The time dependent portion of the interaction, N_{ii} , is assumed to have the form;

$$N_{ii} = fB\sigma_{mean}^{-n} \quad (6.8)$$

where mean stress contributes to the time dependent damage. The cyclic contribution to the interaction term represented by:

$$N_{ci} = A(\Delta\sigma)^{-m} \quad (6.9)$$

The coefficient C was determined empirically.

The coefficient B and exponent n of the time dependent creep rupture time-to-failure term could be determined by a method of linear least squares fit to experimental creep rupture data. However, insufficient creep rupture life

data, two tests at 650°C and three tests at 815°C, were available. The use of experimental creep rupture data to determine B and n resulted in reduced fatigue lives. Therefore, the coefficient B and exponent n , as well as the interaction term coefficient C were empirically determined by fitting the linear summation model predictions to the experimental fatigue life data. The model predictions and experimental fatigue life data are shown in Fig. 68, where $B = 5.0\text{E}+24$ and $n = 6$ at 650°C, and $B = 5.0\text{E}+21$ and $n = 6$ at 815°C. The interaction term coefficient C equaled 0.01 at both 650 °C and 815 °C.

The creep rupture time to failure predictions, equation (6.3), were then plotted using the empirically determined variables with the 650°C and 815°C experimental creep rupture life data in Figs. 71 and 72, respectively. Experimental creep rupture data were provided by M. Khobaib of UDRI [15].

6.2 FATIGUE LIFE PREDICTIONS

Experimental fatigue life data encompassing two temperatures, four frequencies, and three stress ratios are presented in Figures 70, 73, 74 and 75 with the curves representing the model's life predictions. Reasonably good correlation exists between the experimental data and model predictions.

Linear life frequency model predictions and experimental results of 650°C isothermal fatigue tests conducted with a stress ratio of 0.1 are presented in Fig. 70. The model reflects the general trends in the data over the entire range of cycles to failure. The fatigue life model predictions accurately represent the cyclic dependence, described in the fatigue life results section, of the composite at 650°C . Life predictions over the entire stress range agree with experimental results. However, the model does not capture the region below a stress range of 225 MPa or the region approaching the ultimate strength. The model's life predictions increase as stress range decreases and therefore does not represent

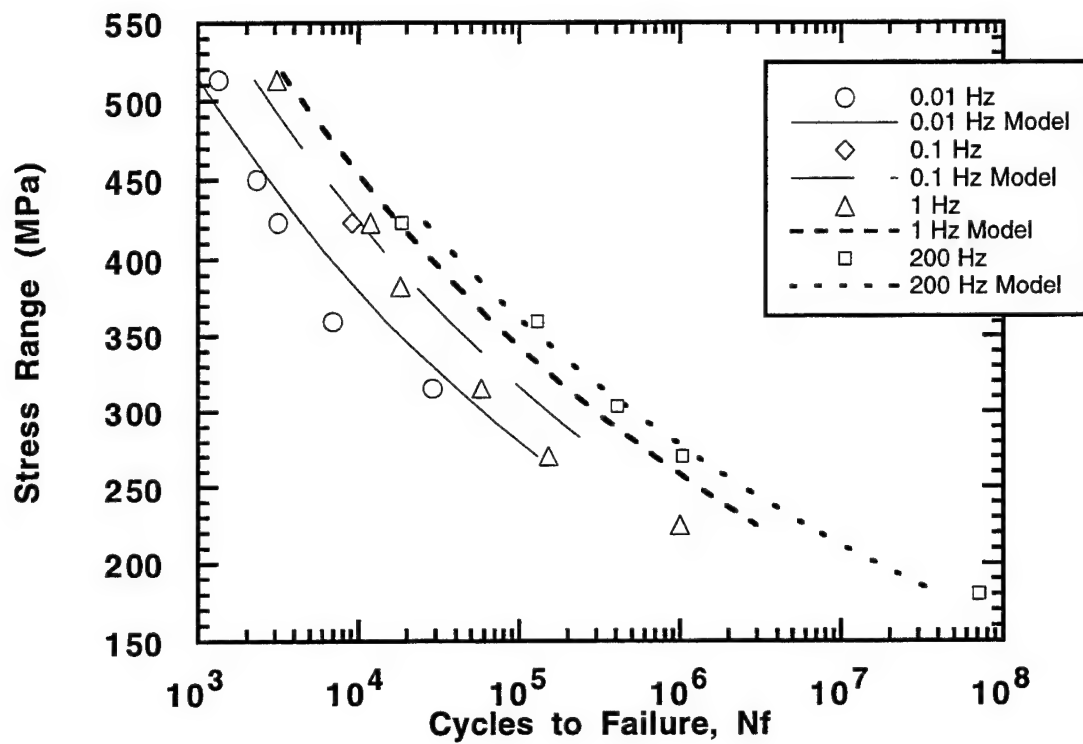


Fig. 70 Experimental data and model predictions for $R=0.1$, 650°C

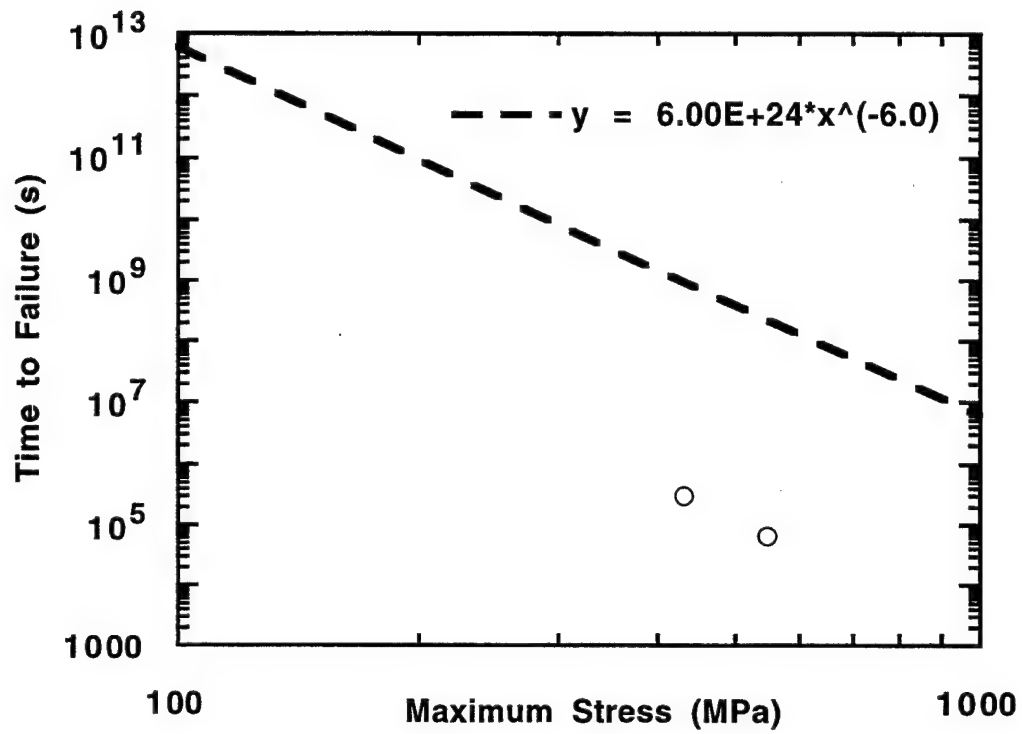


Fig. 71 Time dependent damage term creep rupture life, power law fit, 650°C

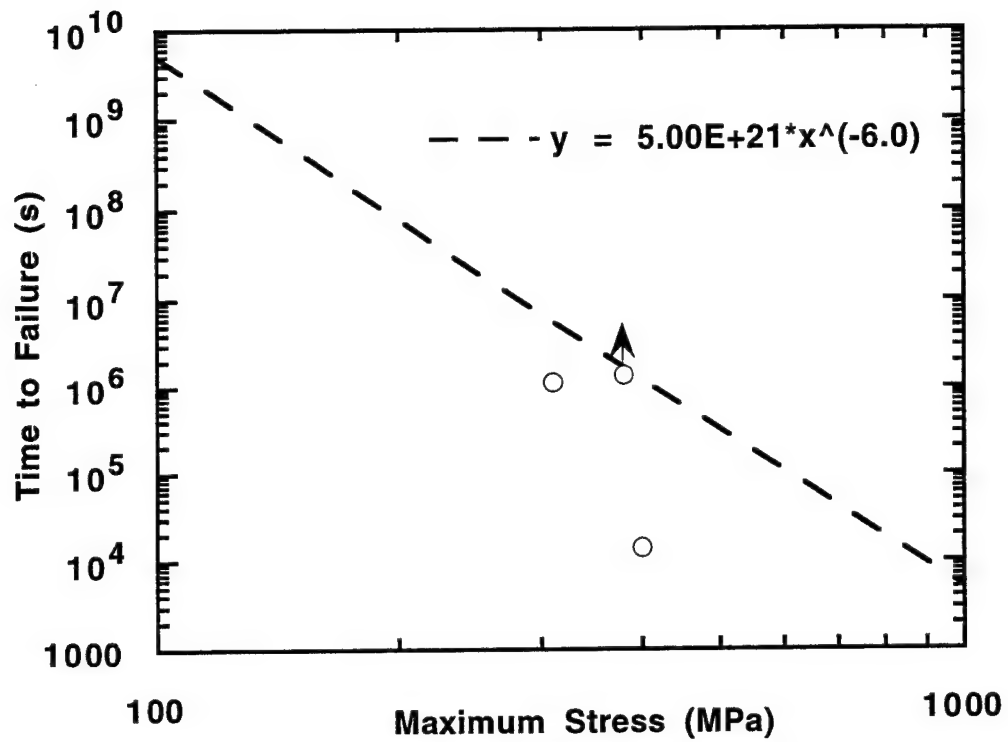


Fig. 72 Time dependent damage term creep rupture life, power law fit, 815°C

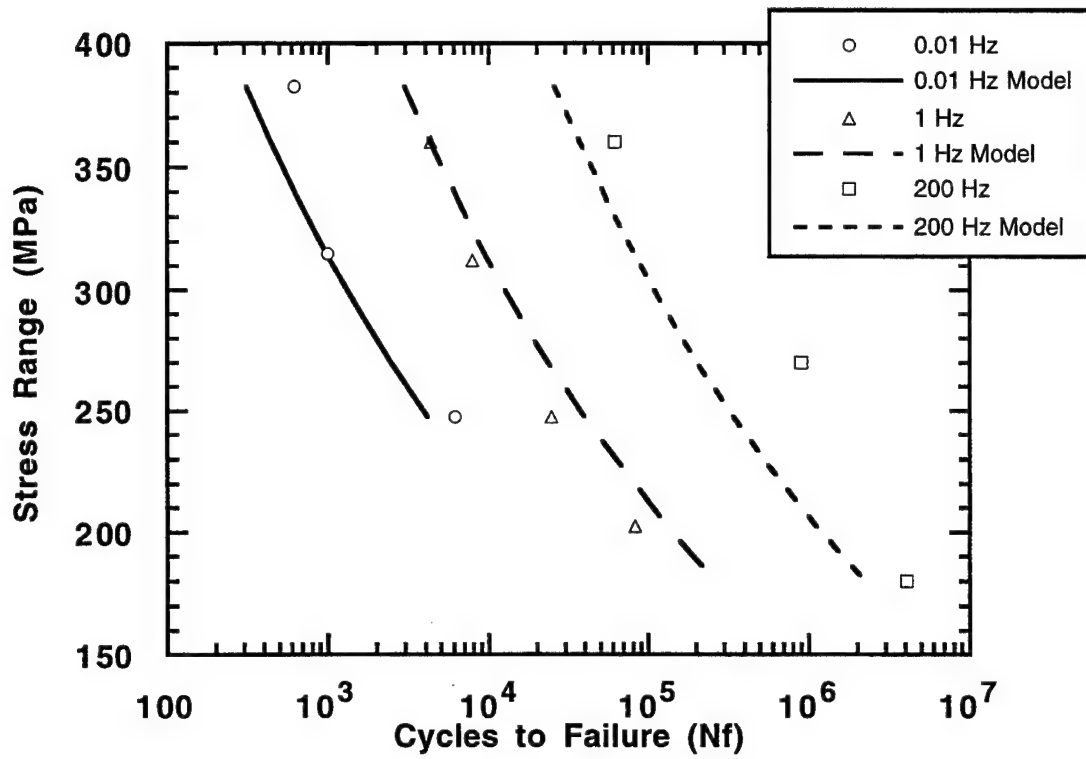


Fig. 73 Experimental data and model predictions at 815°C, R=0.1

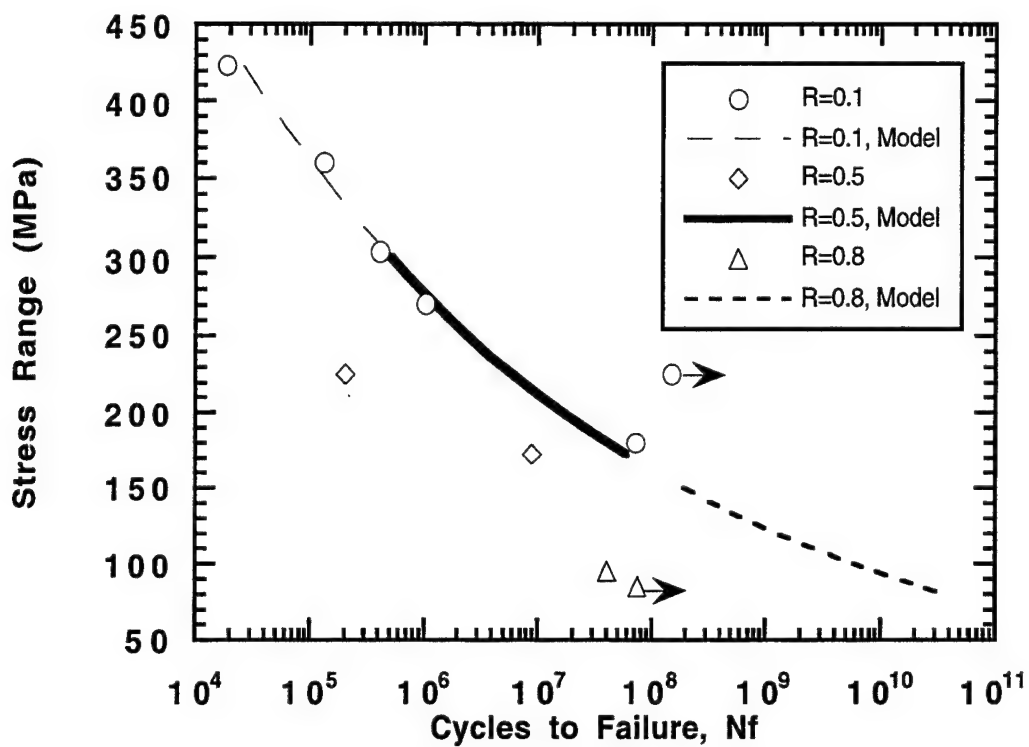


Fig 74 Experimental data and model predictions for 200 Hz, $R=0.1, 0.5$, and 0.8 , 650°C

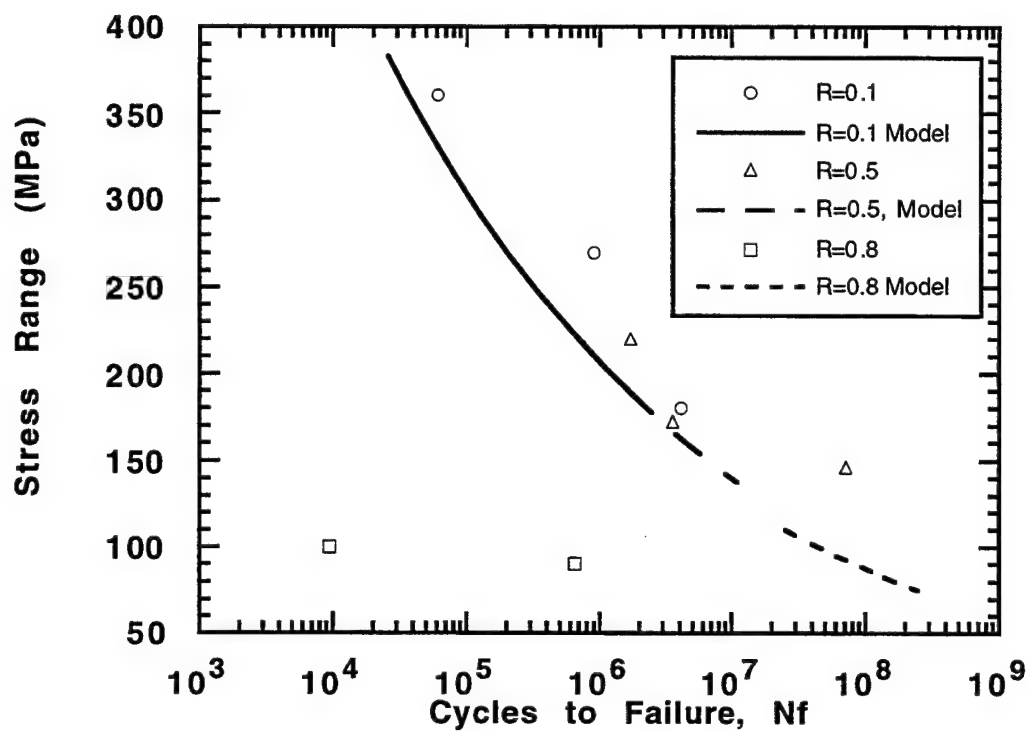


Fig. 75 Experimental data and model predictions for 200 Hz, $R=0.1, 0.5$, and 0.8 , 815°C

the region below the fatigue limit of the composite where failure does not occur [23]. Talreja proposed to represent the region below the fatigue limit with horizontal bands [4].

Shown in Fig. 73 are the experimental data and model predictions at 815°C. The fatigue life results at 815°C differed from the 650°C results with an increase in time dependence. Fatigue lives from three different test frequencies, 0.01, 1 and 200 Hz, and their respective predictions are shown. Again the model accurately represents the trends in the experimental data.

For presentation purposes, higher stress ratio data and model predictions are shown separate from the frequency data. Stress ratio was only varied in high frequency testing, and therefore, no low frequency $R=0.5$, and 0.8 data were available. Figures 74 and 75 present all 200 Hz, 650°C and 815°C data at $R=0.1$, 0.5 , and 0.8 , respectively. The model predictions overestimate fatigue lives at both elevated temperatures by one order of magnitude at a stress ratio of 0.5 , and approximately two orders of magnitude at a stress ratio of 0.8 .

6.3 BLOCK LOADING STUDY

A block loading study was conducted with an interest in predicting, based on constant amplitude loading test data, the fatigue life of a specimen subjected to a variable load history. The Palmgren-Miner cumulative damage law suggests that damage accumulates linearly throughout the fatigue life of a component. Therefore, a specimen subjected to a given fraction of the number of cycles required to cause failure at a given stress level, will sustain a proportional amount of damage. Another way of stating this is that fatigue failure is expected when the life fractions of the variable amplitude loading sum to equal one. In equation form [24, 25]

$$\frac{n_1}{N_{f1}} + \frac{n_2}{N_{f2}} + \dots + \frac{n_i}{N_{fi}} = 1 \quad (6.10)$$

where n_i is the number of cycles applied at a given stress level and N_{fi} is the fatigue life at σ_i .

The block loading study consisted of tests on two specimens, 93-452 and 93-450, with the loading histories shown in Table 10. Also shown in Table 10 are the experimental fatigue lives of constant amplitude fatigue tests, 92-600 and 92-602, whose applied stresses correspond to the stresses in loading block one and two.

The block loading procedure comprised of two consecutive cyclic loads, the first block of cycles equaling 50 % of the experimentally determined cyclic fatigue life for a given stress level followed by a second block cycled to failure. For example, test 93-452 was fatigued at a maximum stress level of 300 MPa for 528,714 cycles, one-half the fatigue life of the constant amplitude test 92-600. The

Table 10

BLOCK LOADING STUDY, R=0.1, 200 Hz

Specimen ID	Block 1		Block 2		Cycles to Failure, N
	Stress σ_1 (MPa)	Cycles n_1	Stress σ_2 (MPa)	Cycles n_2	
93-452	300	528,714	400	125,603	654,317
93-450	400	71,531	300	257,648	329,179
92-600	300	1.04E+6	NA	NA	1.04E+6
92-602	400	1.30E+5	NA	NA	1.30E+5

first loading block was followed by cycling the specimen to failure at a maximum stress of 400 MPa. The procedure was reversed for 93-450, by cycling at 400 MPa for 71,531 cycles followed by cycling the specimen to failure at a maximum stress of 400 MPa. The number of fatigue cycles applied during each loading block and the corresponding stress levels are shown in Table 10.

Due to the nonlinearity of fatigue damage accumulation, and the effect of block sequence, the Palmgren-Miner Law does not result in a summation equaling unity [26]. Typically, a decreasing loading sequence results in a summation less than one:

$$\frac{\sum n}{\sum N} < 1 \quad (7.2)$$

For example, by applying the Palmgren-Miner cumulative damage law to the cyclic results of 93-450, will result in a sum less than unity as shown.

$$\frac{71,531}{130,000} + \frac{257,648}{1,040,000} = 0.798$$

Conversely, an increasing loading sequence will result in a summation greater than one;

$$\frac{\sum n}{\sum N} > 1 \quad (7.3)$$

and the summation of the cyclic results of 93-452 results in a value greater than one as shown below.

$$\frac{528,714}{1,040,000} + \frac{125,603}{130,000} = 1.475$$

A comparison of the percent DCEP increase between the block loading study tests, Fig. 76, suggests that the nonlinear nature of damage accumulation may be observed. The decreasing loading sequence of test 93-450, resulted in an approximate increase of 1 % in measured potential during the first 400 MPa loading block, suggesting the initiation of fatigue damage. The second block loading at 300 MPa followed with an accelerated increase to 13 % in electric potential at failure. The increasing loading sequence of test 93-452, however,

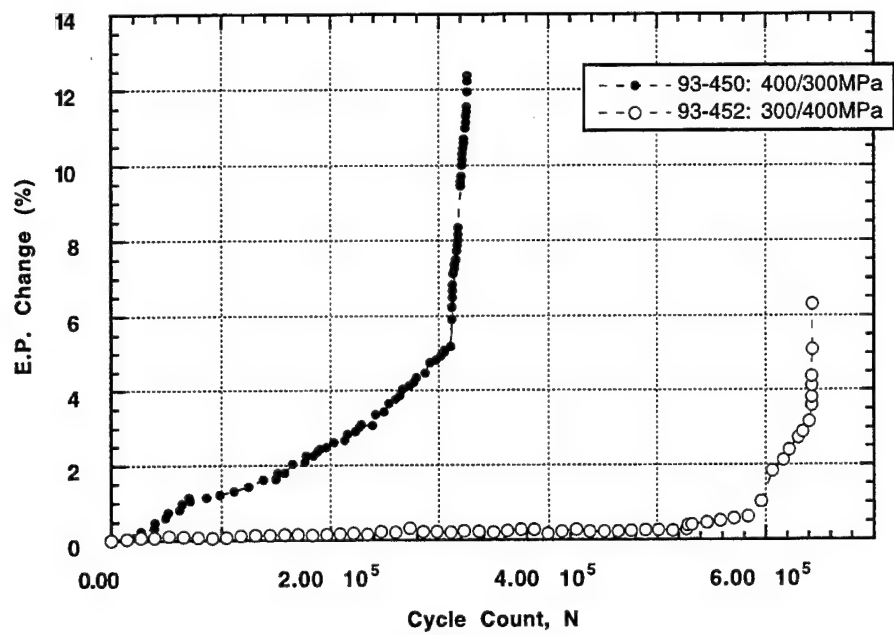


Fig. 76 Block Loading normalized DCEP change

resulted in negligible potential increase during the lower stress of the first loading block indicating the absence of damage. The subsequent second loading block began with virtually no damage identifiable by electric potential techniques to be present in the specimen. The specimen was fatigued for 125,603 cycles at 400 MPa, where the constant amplitude test 92-602 required 130,000 cycles for failure, suggesting that little damage was induced by the first loading block.

The fatigue life and DCEP results of the block loading study strongly suggest that damage accumulates nonlinearly in this MMC. High initial stresses in spectrum loading studies will result in abbreviated fatigue lives and the nonlinear accumulation of damage should be considered when applying the linear-summation model to MMC's.

SECTION 7

CONCLUSIONS

The fatigue behavior of the SCS-6/Timetal®21S [0/90]_S titanium matrix composite was evaluated in an elevated temperature high frequency fatigue environment. Test conditions were chosen to encompass a range of maximum stresses at stress ratios of 0.1, 0.5, and 0.8, and at test temperatures of 650°C and 815°C. All high frequency fatigue tests were conducted on a unique test system at 200 Hz.

The effect of frequency on fatigue behavior was studied by comparing the 200 Hz cyclic lives to that of 0.01 Hz and 1 Hz low frequency fatigue test data. Variations in fiber volume fraction were noted between specimens, and a rule of mixtures technique was implemented to account for the effective stress in the composite constituents. A comparison of the low and high frequency test results indicate that 650°C fatigue lives were primarily cycle dependent. Furthermore, fatigue lives at 815°C display predominately cycle dependence at high stresses. However, a mixed mode of cycle and time dependence was observed at lower stresses where extended time of exposure encourages environmental effects.

Several high frequency tests did not result in fracture of the specimen and an endurance limit could be shown to be influenced by the combined effect of mean stress and stress range.

Fatigue damage was noted to initiate along the 90° fibers as a result of the fiber/matrix interfacial bond failure. Internal crack initiation was evidenced by

matrix cracks which propagated first from the transverse fibers and then around the longitudinal fibers. Fully fiber bridged matrix through-thickness cracking was observed until sufficient cross-sectional area reduction of the matrix and environmental degradation of exposed longitudinal fibers resulted in specimen failure.

Thermal exposure tests indicated that in the absence of mechanical loading induced fatigue cracking, the composite specimens exposed for 100 hours resulted in no reduction in tensile strength.

Electric potential voltage drop was monitored across the specimen gage length and provided a relative indication of damage accumulation throughout the fatigue lives. Although correlation between electric potential increases and quantitative results of crack density or size were not made, this technique should be investigated further.

To promote a better understanding of the fatigue life dependence on cyclic and time dependent factors, a phenomenological linear-life-frequency effect model was adapted to the cross-ply composite. Model predictions were made based on experimental cyclic fatigue life and creep rupture data, and comparisons were made to the experimental results.

SECTION 8

REFERENCES

- [1] Larsen, J.M., Revelos, W.C., and Gambone, M.L., "An Overview of Potential Titanium Aluminide Composites in Aerospace Applications," Intermetallic Composites II, (eds. D.B. Miracle, D.L. Anton, and J.A. Graves), MRS Proceedings, Vol. 273, 1992 Pittsburgh, PA.
- [2] Gambone, M. L., "Fatigue and Fracture of Titanium Aluminides, Vol. II," U.S. Air Force report WRDC-TR-89-4145 Vol. II, Wright-Patterson Air Force Base, OH, 1989.
- [3] Larsen, J. M., Williams, K. A., Balsone, S. J., and Stucke, M. A., "Titanium Aluminides for Aerospace Applications," High Temperature Aluminides and Intermetallics Symposium Proceedings, (eds. S. H. Whang, C. T. Liu, D. P. Pope, J. O. Stiegler), Indianapolis, IN, October 1989.
- [4] Talreja, R., "Fatigue of Composite Materials: Damage Mechanisms and Fatigue Life Diagrams," Fatigue of Composite Materials, Technomic Publishing Co., 1987, pp. 25-38.
- [5] Johnson, W.S., "Fatigue Testing and Damage Development in Continuous Fiber Reinforced Metal Matrix Composites," Metal Matrix Composites: Testing, Analysis, and Failure Modes, ASTM STP 1032, W.S. Johnson, Ed., American Society for Testing and Materials, Philadelphia, 1989, pp. 194-221.
- [6] Johnson, W. S., "Damage Development in Titanium Metal Matrix Composites Subjected to Cyclic Loading," Presented as a Keynote Lecture at Fatigue and Fracture of Inorganic Composites, March 31-April 2, 1992, Cambridge, UK.

- [7] Kortyna, B.R., Ashbaugh, N.E., "Fatigue Characteristics of a Titanium Aluminide Composite at Elevated Temperature," Titanium Aluminide Composites, Workshop proceedings, eds. P.R. Smith, S.J. Balsone, and T. Nicholas, Materials Directorate, WPAFB, WL-TR-91-4020, February 1991.
- [8] McAfee, J.L., Spear, S.R., Niemann, J.T., and Lewis, W.J., "The Thermal Stability of Beta21S Titanium Alloy and its Suitability as a Matrix Alloy for the X-30 TMC Fuselage," Titanium Matrix Composites, Workshop Proceedings, eds. P.R. Smith, W.C. Revelos, Materials Directorate, WPAFB, WL-TR-92-4035, April 1992.
- [9] Das, G., "Microstructural Characterization of Ceramic Reinforcements for Composites," Titanium Aluminide Composites, Workshop proceedings, eds. P.R. Smith, S.J. Balsone, and T. Nicholas, Materials Directorate, WPAFB, WL-TR-91-4020, February 1991.
- [10] Stubbs, D. A., Russ, S. M., and MacLellan, P. T., "Examination of the Correlation Between NDE-detected Manufacturing Abnormalities in MMCs and Ultimate Tensile Strength or Thermomechanical Fatigue Life," accepted for publication in an STP on Cyclic Deformation, Fracture & Nondestructive Evaluation, American Society for Testing and Materials, 1994.
- [11] Kortyna, B. R., "High Cycle Fatigue Behavior of an SCS-6/Ti-24Al-11Nb Composite," M. S. Thesis, University of Dayton, TR-90-77, Dayton, OH, August, 1990.
- [12] Hartman, G. A., and Johnson, D. A., "D-C Electric Potential Method Applied to Thermal/Mechanical Fatigue Crack Growth," Experimental Mechanics, Vol. 27, No.1, pp. 106-112, March 1987.
- [13] Nicholas, T., Russ, S. M., "Fatigue Life Modeling in Titanium Matrix Composites," Proceedings of the American Society for composites-Ninth Technical conference, September 20-22, 1994, Newark, Delaware.
- [14] Castelli, M., and Ellis, R., Private Communication, Fall 1992.

- [15] Ashbaugh, N. E., Khobaib, M., "Characterization of Titanium Matrix Composites," NASP Technical report 1199, Vol. IV, National Institute for the Mechanics and Life Prediction of High Temperature Composites (NIC), Wright Laboratory, Materials Directorate, Wright-Patterson Air Force Base, OH, 1994.
- [16] Revollos, W. C., Jones, J. W., and Dolley, E. J., "Thermal Fatigue of a SiC/Ti-15Mo-2.7Nb-3Al-0.2Si (wt. %) Composite," in press for Acta Metallurgica, 1993.
- [17] Larsen, J. M., Russ, S. M., and Jones, J. W., "Possibilities and Pitfalls in Aerospace Applications of Titanium Matrix Composites," NATO AGARD conference on Characterization of Fibre Reinforced Titanium Metal Matrix Composites, Bordeaux, France, September, 1993.
- [18] Mahoney, M. W., Martin, P. L., and Hardwich, D. A., "Microstructural Stability of Beta 21S," 7th World Conference on Titanium, Proceedings, TMS, San Diego CA, 1992, pp.
- [19] Gayda, J., and Gabb, T. P., "Isothermal Fatigue Behavior of a [90°]8 at 426°C," International Journal of Fatigue, No. 1, pp. 14-20, 1992.
- [20] Russ, S. M., and Hanson, D. G., "Fatigue and Thermomechanical fatigue of a SiC/Titanium [0/90]8 Composite," FATIGUE 93, Volume II, J.P. Bailon and J.I. Dickson, Eds., Chameleon Press, London, U. K., 1993, pp. 969-974.
- [21] Timetal®21S Data Sheet, TIMET, 1999 Broadway, Denver, CO 80202.
- [22] Nicholas, T., and Russ, S. M., "Elevated Temperature Fatigue Behavior of SCS-6/Ti-24Al-11Nb," Journal of Materials Science and Engineering, A153, 1992, pp. 514-519.
- [23] Nicholas, T., Russ, S., Schehl, N., and Cheney, A., "Frequency and Stress Ratio Effects on Fatigue of Unidirectional SCS-6/Ti-24Al-11Nb Composite at 650°C," FATIGUE 93, Volume II, J.P. Bailon and J.I. Dickson, Eds, EMAS, 1993, pp. 995-1000.
- [24] Dowling, N. E. Mechanical Behavior of Materials, New Jersey, Prentice-Hall, 1993.

- [25] Shigley, J. E., Mischke, C. R. Mechanical Engineering Design, New York, McGraw-Hill, 1989.
- [26] Hertzberg, R. W., Deformation and Fracture Mechanics of Engineering Materials, John Wiley & Sons, Inc., New York, 1989.